ACCELERATION OF SOLAR ENERGETIC PARTICLES IN CORONAL SHOCKS THROUGH SELF-GENERATED TURBULENCE

by

Markus Battarbee

From
  Department of Physics and Astronomy
  University of Turku
  FI-20014 Turku
  Finland

Supervised by
  Prof. Eino Valtonen
  Department of Physics and Astronomy
  University of Turku
  Finland

Advisors
  Docent Timo Laitinen, Ph.D.   Docent Rami Vainio, Ph.D.
  Jeremiah Horrocks Institute   Department of Physics
  University of Central Lancashire   University of Helsinki
  United Kingdom   Finland

Reviewed by
  Prof. Ilya Usoskin   Dr. Chee Ng
  Dept. of Physical Sciences   Astrophysics Science Division
  University of Oulu   NASA Goddard Space Flight Center
  Finland   USA

Opponent
  Dr. Silvia Dalla
  Jeremiah Horrocks Institute
  University of Central Lancashire
  United Kingdom

Abstract

The acceleration of solar energetic particles (SEPs) by flares and coronal mass ejections (CMEs) has been a major topic of research for the solar-terrestrial physics and geophysics communities for decades. This thesis discusses theories describing first-order Fermi acceleration of SEPs through repeated crossings at a CME-driven shock. We propose that particle trapping occurs through self-generated Alfvén waves, leading to a turbulent trapping region in front of the shock.

Decelerating coronal shocks are shown to be capable of efficient SEP acceleration, provided seed particle injection is sufficient. Quasi-parallel shocks are found to inject thermal particles with good efficiency. The roles of minimum injection velocities, cross-field diffusion, downstream scattering efficiency and cross-shock potential are investigated in detail, with downstream isotropisation timescales having a major effect on injection efficiency.

Accelerated spectra of heavier elements up to iron are found to exhibit significantly harder spectra than protons. Accelerated spectra cut-off energies are found to scale proportional to $(Q/A)^{1.5}$, which is explained through analysis of the spectral shape of amplified Alfvénic turbulence. Acceleration times to different threshold energies are found to be non-linear, indicating that self-consistent time-dependent simulations are required in order to expose the full extent of acceleration dynamics. The well-established quasilinear theory (QLT) of particle scattering is investigated by comparing QLT scattering coefficients with those found via full-orbit simulations. QLT is found to overemphasise resonance conditions. This finding supports the simplifications implemented in the presented coronal shock acceleration (CSA) simulation software.

The CSA software package is used to simulate a range of acceleration scenarios. The results are found to be in agreement with well-established particle acceleration theory. At the same time, new spatial and temporal dynamics of particle population trapping and wave evolution are revealed.

Contents

Preface

Dear reader,

thank you for showing interest in this fascinating field of research. Immeasurable thanks to both my advisors, Timo Laitinen and Rami Vainio, who have ensured continued guidance, inspiration and vigour in approaching new mental challenges. Thank you to my professor, Eino Valtonen, for enlisting me as a research member of our group, and for continued assistance in funding my adventures in the fields of solar science. A big thank you goes to all my colleagues, including, but not limited to: Esa Riihonen, Timo Eronen, Oskari Saloniemi, Jussi Lehti, Jouni Saari, Osku Raukunen, Amjad Al-Sawad, Jouni Peltonen, Juho-Ville Saarela, Tero Sahla, Silja Pohjolainen and professor Jarmo Torsti.

I wish to express my gratitude to my esteemed opponent, Dr. Silvia Dalla, for agreeing to travel to Finland in order to critique my work. I greatly appreciate the assistance given by prof. Ilya Usoskin and Dr. Chee K. Ng in reviewing my thesis and providing valuable feedback. I wish to thank my co-authors and collaborators both nationally and internationally, including Heli Hietala, Neus Agueda, Jens Pomoell, Arto Sandroos, Alexandr Afanasiev, Felix Spanier, Sebastian Lange, and numerous other acquaintances over the years.

Although science is fascinating, life is not much without friends. I consider myself lucky to have so many amazing friends, both within and outside the world of physics. To all you, too numerous to list, thank you!

A huge thank you to my mother and father for trusting me to become the person I am today, and to my brother and sister for inspiring me throughout the years. Finally, I want to thank my wife, Elina, for the love, support and encouragement she has always offered me.

Turku, October 2013

Markus Battarbee

List of papers

The aim of this dissertation is to describe the physics, underlying theories and Monte Carlo simulation methods used by the author in researching solar energetic particle acceleration at coronal shocks. This thesis consists of a review of the subject and the following original research articles:

I   **Acceleration of Energetic Particles Through Self-Generated Waves in a Decelerating Coronal Shock**
M. Battarbee, T. Laitinen, R. Vainio and N. Agueda, Twelfth International Solar Wind Conference, AIP Conference Proceedings **Vol. 1216**, pp. 84-87 (2010). [`arXiv:1303.4334`].
URL `http://dx.doi.org/10.1063/1.3395969`.

II   **Heavy-ion Acceleration and Self-generated Waves in Coronal Shocks**
M. Battarbee, T. Laitinen and R. Vainio, Astronomy & Astrophysics **Vol. 535**, A34 (2011) [`arXiv:1303.4340`].
URL `http://dx.doi.org/10.1051/0004-6361/201117507`.

III   **Injection of thermal and suprathermal seed particles into coronal shocks of varying obliquity**
M. Battarbee, R. Vainio, T. Laitinen and H. Hietala, Astronomy & Astrophysics **Vol. 558**, A110 (2013) [`arXiv:1309.2062`].
URL `http://dx.doi.org/10.1051/0004-6361/201321348`.

IV   **Particle scattering in turbulent plasmas with amplified wave modes**
S. Lange, R. Vainio, M. Battarbee, F. Spanier and T. Laitinen, Astronomy & Astrophysics **Vol. 553**, A129 (2013) [`arXiv:1303.7463`].
URL `http://dx.doi.org/10.1051/0004-6361/201220804`.

The author's contributions to the included papers is as follows.

Paper I The manuscript was written by the author, with assistance from the advisors. The focus of the research was chosen in collaboration with the advisors. The simulation software programming and research involved in choosing advection methods was completed by the author. Data analysis was conducted by the author, with significant input to conclusions and the quality of the text given by both advisors.

Paper II The manuscript was written by the author, with assistance from the advisors, where R. Vainio was responsible for the bulk of acceleration timescale analysis. The extension of the software to support multiple ion populations was undertaken by the author, as was the extension of applicable theoretical formulae, with input from both advisors. Data analysis, visualisation and data fitting was conducted by the author.

Paper III The manuscript was written by the author, with assistance from the advisors. All additions and extensions to the simulation software required for this research were completed by the author. The author completed all simulational tasks, semianalytical research and visualisation tasks. H. Hietala advised the author on statistical injection probability calculations.

Paper IV The author supplied the numerical SQLT calculations used in the manuscript. Additionally, the author took part in formulating the numerical SQLT application used. The MHD turbulence simulations and particle orbit calculations were conducted by S. Lange and F. Spanier. The author had no input on the GISMO code.

Abbreviations used

All equations in this thesis use the *cgs* system of units.

AU	Astronomical Unit
CIR	Co-rotating Interaction Region
CME	Coronal Mass Ejection
CR	Cosmic Ray
HT	de Hoffmann-Teller
DSA	Diffusive Shock Acceleration
EM	ElectroMagnetic
EQLT	Extended Quasi-Linear Theory
EUV	Extreme UltraViolet
GLE	Ground Level Event / Enhancement
HDU	Header + Data Unit
IMF	Interplanetary Magnetic Field
IP	InterPlanetary
LHS	Left-Hand Side of equation
MHD	MagnetoHydroDynamics
QLT	Quasi-Linear Theory
RHS	Right-Hand Side of equation
SDA	Shock Drift Acceleration
SEP	Solar Energetic Particle
SNIF	Shock Normal Incidence Frame
SQLT	Standard Quasi-Linear Theory

Part I

Introduction

Chapter 1

Solar Energetic Particles

1.1 The Sun

The Sun, designated with the symbol $\odot$, is our life force. It feeds energy to the solar system through electromagnetic (EM) radiation, gravitational forces, plasma waves and ejected particles. The constant outflowing stream of electrons and ions, known as the solar wind (Gringauz et al. 1960), is a dilute hot plasma, streaming outwards through the planetary zone until it forms the termination shock at the edge between the solar system and interstellar space. Processes on the solar surface and in the solar corona can release massive amounts of energy, leading to clouds of ejected plasma, shock waves, and accelerated particles.

Solar wind ion charge states and abundances (see, e.g., Lodders 2003) can vary both between different phases of the 11-year solar activity cycle (Lee 2000), different solar wind outflow regions (Srivastava & Schwenn 2000), and different individual energy release events (Tylka et al. 1999). As the solar wind (slow wind at ca. 400 km s^{-1}, fast wind at ca. 700 km s^{-1}) is mostly collisionless, high energy particles do not thermalise efficiently. Some particles can be accelerated as Solar Energetic Particles (SEP) to tens or hundreds of MeV per nucleon, or, in the case of Ground-Level Enhancement (GLE) events (Cliver et al. 1983; Reames 2009; Gopalswamy et al. 2012), into the GeV range. These SEPs constitute a real hazard to telecommunications, global positioning systems, space flight, and astronaut safety.

The Earth has a strong internal dipole magnetic field, which extends into near-Earth space as the magnetosphere (Fairfield 1968). A boundary called the magnetopause exists where the solar wind and the extended magnetic field of the Sun impact on the magnetosphere of the Earth. The

impacting solar wind forms a bow shock in front of the magnetosphere. The shocked and deflected region of plasma between the magnetopause and the bow shock is known as the magnetosheath.

The magnetosphere shields the Earth, suppressing the influx of energetic charged particles, which could potentially cause significant damage to near-Earth satellites and astronauts conducting spacewalks (see, e.g., Dorman & Pustil'nik 2008). Operation outside the protection of the magnetosphere is only possible if the variations and effects of the solar environment are well understood.

The term *Space weather* can be used both as a description of solar processes and conditions harmful to technology and life (Wright et al. 1995) and as a more encompassing description for the physical and phenomenological states of natural space environments (Watermann et al. 2009). In studying and simulating SEP acceleration processes, we can attain a better understanding of space weather and how to take it into account in space mission design.

1.2   Observations of energetic particles

The rise of the space age has allowed mankind to breach the limitations of ground-based observations, greatly increasing our capabilities in detecting and understanding solar activity. Missions observing the solar wind and the Sun from the Lagrange point L1, approximately stationary between the Sun and the Earth, include, for example, ACE (Advanced Composition Explorer), Wind, and SOHO (Solar and Heliospheric Observatory). The Solar Dynamics Observatory or SDO is in geosynchronous orbit around the Earth. The Cluster mission observes interactions between the solar wind and Earth's magnetosphere in orbit around the Earth, whereas the STEREO (Solar Terrestrial Relations Observatory) mission consists of twin spacecraft orbiting around the Sun at approximately 1 astronomical unit (AU), with one unit orbiting ahead of the Earth, one following behind it. Aboard the International Space Station, the AMS-02 (Alpha Magnetic Spectrometer) further extends the observation of very high energy cosmic rays (CRs). Other projects observing cosmic rays include, for example, PAMELA and BESS. One example of a future mission for solar observations is SolO (Solar Orbiter), which will achieve an elliptical orbit around the Sun, with a perihelion of 0.284 AU. Another is SPP (Solar Probe Plus), with
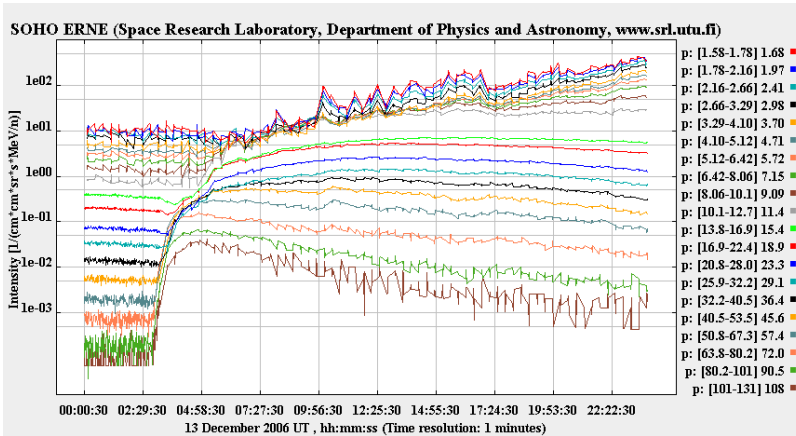
Figure 1.1: An example of particle flux detected by ERNE/LED and ERNE/HED aboard SOHO from the December 13th, 2006 event. Energy ranges are in units MeV. Image credit: SEPServer (www.sepserver.eu)

a perihelion distance of only 0.04 AU. When spacecraft positions allow, multi-spacecraft observations can be used to infer the spatial and temporal evolution of an event and associated SEP populations (see, e.g., Malandraki et al. 2012 and Ng et al. 2012).

SEP observations can be done on a per-particle basis, or by generating series of particle fluxes with segmented energy ranges (see, e.g., Torsti et al. 1988). Particles are classified according to element and isotope, and sometimes, charge state. Some instruments, such as ERNE aboard SOHO, are capable of transmitting information on the directions of incident particles, which can be used to infer the angular distribution of the flux (Torsti et al. 1997). Instruments are capable of observing only a limited range of particle energies although, for example, AMS-02 and PAMELA can observe particles in the GeV or even TeV range. Example data gathered by ERNE from the December 13th, 2006 event is shown in figure 1.1.

Before impacting the detector, accelerated particles travel through the interplanetary medium, altering their angular and temporal profiles (see, e.g., Kocharov et al. 2009). Deconvolution of the effects of IP transport on properties of a SEP population can be used to find out additional information on the release site. Solar event properties can also be probed by EM

observations. Particle and EM observations, along with particle accelera-
tion theory and combined with numerical simulations, are an excellent tool
for furthering our understanding of solar phenomena.

1.3   Particle acceleration sources

Historically, SEP events were believed to originate at solar flares, observable
from the surface of the Earth through white light and hydrogen alpha-
line (Hα) emission. New and improved observational methods, facilitated
by spacecraft, encouraged attempts to categorise them. Since the 1980s,
SEP events have been split into two categories as impulsive and gradual
events (see, e.g., Reames et al. 1992). During these events, the particle
flux can increase by orders of magnitude. Impulsive events last from hours
to a few days, while gradual events can last up to a week. Research into
acceleration mechanisms at flares or shocks (see, e.g., Reames 2002) has
presented several mechanisms capable of explaining acceleration to high
energies, which can be used to describe features related to particle spectra,
temporal profiles, and ion ratios.

Observations of radiative emissions such as radio waves as well as soft
and hard X-rays can be used to connect the source of particle acceleration
to events visible on the solar disk. Emission profiles and their resemblance
to impulsive or gradual events (see, e.g., Reames 1990b and Reames et al.
1992) are an important classification tool.

Although some events seem to fit neatly into one or the other category,
there is a large indefinite group of *mixed* events exhibiting properties of
both types (see, e.g., Cane et al. 2003 and Tylka et al. 2005). Observed
particle fluxes can appear to exhibit both prompt and gradual components,
especially at high energies or for minor ions. Multi-peaked events may
suggest flare and shock acceleration occurring concurrently (Li & Zank
2005).

At the same time, there appears to be only a weak connection between
shock parameters and SEP acceleration efficiency (Lario et al. 2005). In
recent years, a growing trend has been to view shocks as the primary source
of energetic particle acceleration for both gradual and mixed events, with
flares providing important seed particle population enhancements (see, e.g.,
Mason et al. 1999, Tylka et al. 2001, Tylka et al. 2005 and Sandroos &
Vainio 2009b), which can lead to increased acceleration efficiency and ion

composition resembling impulsive events. In this thesis, we focus on coronal shocks as sources of SEP acceleration.

1.4 Shock acceleration mechanisms

As solar wind particles encounter a propagating coronal shock, they may experience significant acceleration and reach high energies through various interactions (see, e.g., Fisk 1971; van Nes et al. 1984). *Diffusive Shock Acceleration* (DSA) is the process of particles gaining energy from repeated shock crossings due to scatterings in both the upstream and the downstream of the shock. *Shock Drift Acceleration* (SDA) describes energy gains of particles due to the motional electric field. *Shock Surfing* describes small-scale acceleration of particles, trapped at the shock front due to the cross-shock potential, experiencing acceleration by the motional electric field.

1.5 Particle populations

SEP fluxes and the solar wind consist of the primary elements found in the Sun (hydrogen, helium) and heavier elements. The exact composition of the solar wind is modified by solar cycle activity, the source region, and the solar wind type (Ross & Aller 1976; Reames et al. 2012). In table 1.1, we present a selection of energetic particle types and their related elemental abundances.

Due to the high temperature of the solar corona, gas exists in a plasma state where hydrogen is found almost exclusively as detached protons and electrons, and many heavier elements have also lost a significant fraction of their electrons. The existence of both ions and electrons results in a macro-scopically neutral plasma which can exhibit freeze-in of magnetic field-lines (Alfv́en 1950). Alfvén (1977) delves further into this particle-field interaction of plasmas.

A thermalised proton population has a Maxwellian velocity distribution, given as

$$f(\mathbf{v}) = \left(\frac{m_{\mathrm{p}}}{2\pi k_{\mathrm{B}} T} \right)^{3/2} \exp \left[-\frac{m_{\mathrm{p}} |\mathbf{v}|^2}{2 k_{\mathrm{B}} T} \right], \tag{1.1}$$

where $\mathbf{v}$ is the velocity of the particle, m_{p} is the proton mass, k_{B} is the

Boltzmann constant, and T is the plasma temperature. As the plasma of the solar wind is dilute, it is considered collisionless, and the distribution function of the plasma can differ from the Maxwellian. Thus, the solar corona can consist of both thermal and non-thermal particle populations, exhibiting suprathermal tails extending to high energies.

In order to model a particle population exhibiting a suprathermal tail, we use the κ-distribution (Vasyliunas 1968; Prested et al. 2008), described by the equation

$$f(\mathbf{v}) = \frac{n(r)\Gamma(\kappa+1)}{w_0^3 \pi^{3/2} \kappa^{3/2} \Gamma(\kappa-1/2)} \left[1 + \frac{|\mathbf{v}|^2}{\kappa w_0^2}\right]^{-\kappa-1}, \tag{1.2}$$

where $n(r)$ is the plasma density, r is the heliocentric distance, Γ is the Gamma function, and w_0 is a representative velocity parameter related to the kinetic temperature T as

$$w_0 = \sqrt{2Tk_{\mathrm{B}}\frac{\kappa-3/2}{\kappa m_{\mathrm{p}}}}. \tag{1.3}$$

The parameter κ signifies the strength of the suprathermal tail, with lower values resulting in stronger tails, and the distribution approaches a Maxwellian as $\kappa \to \infty$. In this work, a κ-distribution of $\kappa = 2$ is used to represent a strongly non-thermal particle population, and a parameter of $\kappa = 15$ is used to represent a nearly Maxwellian distribution. A sample of distribution functions following the κ-distribution is shown in figure 1.2.

1.6   Energetic particle transport

In order to understand transport and acceleration of SEPs, it is essential to review the basic equations governing their motion within the solar wind plasma environment. We assume an infinitely conducting plasma with background magnetic field $\mathbf{B}_0$, and assume that a transformation to a frame with macroscopic electric field $\mathbf{E}_0 = 0$ is possible. The motion of a charged particle with velocity $\mathbf{v}$, momentum $\mathbf{p}$, and charge q can be described with the guiding centre approximation, split into motion parallel to the magnetic field line ($v_\parallel = v\cos\theta$) and perpendicular to it ($v_\perp = v\sin\theta$). θ is the particle pitch-angle, and $\mu = \cos\theta$ is the pitch-angle cosine. Perpendicular motion occurs along a helical path, with angular gyrofrequency
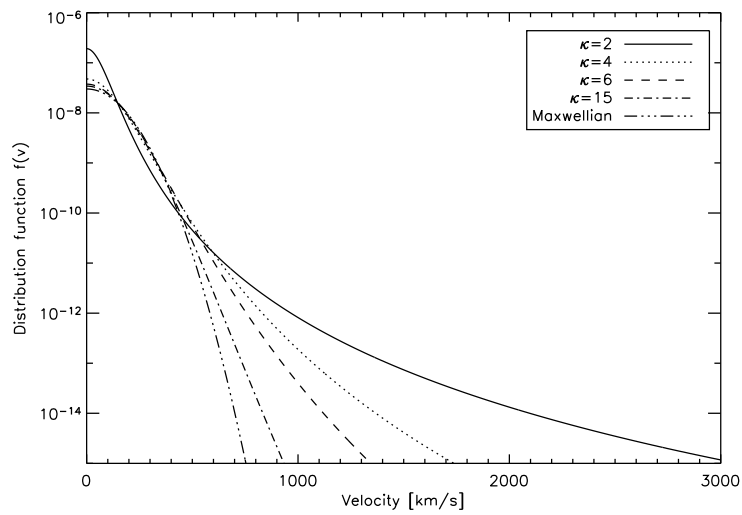
Figure 1.2: Sample particle distribution functions $f(v)$ with κ=2, 4, 6, and 15, along with a Maxwellian distribution function.

$\mathbf{\Omega} = -q\mathbf{B}/(\gamma mc)$, where c is the speed of light, and γ is the particle Lorentz factor. The *Larmor radius* of the gyropath is $r_{\mathrm{L}} = v_\perp/\Omega = \gamma mcv_\perp/(qB)$. The guiding centre is found by projecting the position of the particle to the field line at the centre of the gyropath. The guiding centre propagates at speed $v_\parallel$. This approximation is valid as long as the characteristic spatial scale of the magnetic field is much larger than the Larmor radius.

In the absence of non-magnetic forces, changing magnetic flux density can cause a particle to be deflected, with $v_\parallel$ and $v_\perp$ changing whilst v remains constant. As magnetic flux density B increases, parallel velocity decreases, and a particle can experience magnetic mirroring. As B decreases, the particle is focused towards smaller pitch-angles.

1.7 Kinetic theory

The evolution of a particle population can be described through kinetic theory as an equation of change for the distribution function of particles. To begin, we may assume all changes of state are adiabatic, and consider Liouville's theorem, i.e., the conservation of the distribution function $f_\alpha(\mathbf{r}, \mathbf{p}, t)$ for particle population α in phase space along particle orbits (Gibbs 1902). Extending this to the whole distribution function and defining $\dot{\mathbf{r}} = \mathbf{v}$ and $\dot{\mathbf{p}} = q(\mathbf{E} + \mathbf{v} \times \mathbf{B}/c)$ yields

$$\frac{\mathrm{d}f_\alpha}{\mathrm{d}t} = \frac{\partial f_\alpha}{\partial t} + \dot{\mathbf{r}} \cdot \nabla_r f_\alpha + \dot{\mathbf{p}} \cdot \nabla_p f_\alpha = 0. \tag{1.4}$$

This is the kinetic form of the *collisionless Boltzmann equation*, also known as the *Vlasov equation*.

The Vlasov equation can be altered to use ensemble averages, where $\langle f_\alpha(\mathbf{r}, \mathbf{p}, t) \rangle = F_\alpha(\mathbf{r}, \mathbf{p}, t)$, describing average evolution of a population experiencing random magnetic fluctuations. We consider an ensemble of small-scale fluctuations and quasilinear approximations (see, e.g., Schlickeiser 2002), and define the coordinate system as $\xi_i = (p, \mu, \phi, x, y, z)$. This is also presented in **Paper IV**, section 2.2, using coordinates X_σ. Here p and μ describe particle momentum in the plasma rest frame, ϕ is the gyrophase, and x, y, and z are spatial coordinates of the guiding centre. This allows rearranging the Vlasov equation as a diffusion equation, known as the *Fokker-Planck equation* (Chandrasekhar 1943). This, assuming a

homogeneous background magnetic field, takes the form

$$\frac{\partial F_\alpha}{\partial t} + v\mu \frac{\partial F_\alpha}{\partial z} - \Omega \frac{\partial F_\alpha}{\partial \phi} - \frac{1}{p^2} \frac{\partial}{\partial \xi_i} \left(p^2 D_{\xi_i \xi_j} \frac{\partial F_\alpha}{\partial \xi_j} \right) = S_\alpha, \qquad (1.5)$$

where $S_\alpha = S_\alpha(p, \mu, \phi, x, y, z)$ is a source function and $D_{\xi_i \xi_j}$ is a Fokker-Planck coefficient, and where Einstein summation is applied over i and j. These diffusion coefficients are a way of describing the phase-space evolution of a particle population due to, for example, collisions and scattering off magnetic fluctuations such as Alfvénic turbulence. Choosing to limit motion to the guiding centre approximation along a single radial field line, averaging over all gyrophases, and representing the coordinate system as $\hat{\xi}_i = (p, \mu, z)$ allows describing the plasma rest frame evolution of the ensemble average of particles $\hat{F}_\alpha(p, \mu, z)$ with the equation

$$\frac{\partial \hat{F}_\alpha}{\partial t} + v\mu \frac{\partial \hat{F}_\alpha}{\partial z} - \frac{1}{p^2} \frac{\partial}{\partial \hat{\xi}_i} \left(p^2 D_{\hat{\xi}_i \hat{\xi}_j} \frac{\partial \hat{F}_\alpha}{\partial \hat{\xi}_j} \right) = \hat{S}_\alpha(p, \mu, z). \qquad (1.6)$$

A major topic of research related to CRs is that of solving the various Fokker-Planck coefficients, allowing formulation of CR transport equations (see, e.g., Kulsrud & Pearce 1969, Jokipii 1971, Luhmann 1976, and Ruffolo 1995). The transport of energetic particles including adiabatic effects, magnetic focusing (Earl 1976), and interactions with turbulence are detailed in chapter 3.

	Z	Photosphere[1]	Gradual events[2] (SEP Corona)	CIR events[2] (Coronal Hole)	Impulsive flares [2]	Anomalous CR[3]	Galactic CR source[4]
H	1	1.35×10^6	$(1.57 \pm 0.22) \times 10^6$	$(1.81 \pm 0.24) \times 10^6$	$\sim 1 \times 10^6$	$\sim 1000 \pm 500$	$(1.74 \pm 0.43) \times 10^5$
He	2	$(132 \pm 11) \times 10^3$	$(57 \pm 3) \times 10^3$	$(159 \pm 10) \times 10^3$	$(46 \pm 4) \times 10^3$	$(5 \pm 1) \times 10^3$	$(23.5 \pm 1.6) \times 10^3$
C	6	479 ± 55	465 ± 9	890 ± 36	434 ± 30	< 10	843 ± 67
N	7	126 ± 20	124 ± 3	140 ± 14	157 ± 18	120 ± 10	61 ± 24
O	8	1000 ± 161	1000 ± 10	1000 ± 37	1000 ± 45	1000 ± 10	1000 ± 40
Fe	26	42.7 ± 3.9	134 ± 4	97 ± 11	1078 ± 46	< 0.9	182 ± 11

Table 1.1: Selection of elemental abundances in energetic particle sources. Collected by (Reames 1999a), with data from (Grevesse et al. 1996)[1], (Reames 1995, 1998)[2], (Reames 1999b)[3] and (Lund 1989)[4].

Chapter 2

Coronal Shocks

2.1 Geometry

Coronal mass ejections occur with a variety of shapes and temporal profiles and, thus, there is no single correct way to model their morphology. However, as a CME-driven shock will originate at a source of rapid energy release, a feasible way to study the phenomenon is to view the shock driven as a rapidly expanding nearly spherical front or dome. Recent EUV observations (see, e.g., Ma et al. 2011 and Grechnev et al. 2011) support this interpretation. An example of such a framework is given in figure 2.1. The released energy and expanding plasma cloud deform the structure of the solar corona, which can have pre-existing complex formations.

The propagating coronal shock will intersect a number of magnetic field lines with different geometries (Pomoell et al. 2011), possibly with extensive ripples and perturbations (Giacalone & Neugebauer 2008). As direct observations of ambient field lines are beyond our present capabilities, the exact extent of deformation of the interplanetary magnetic field (IMF) is unknown. A simplified, often used model is the Parker spiral, where magnetic field lines are frozen in the radially propagating solar wind, and the rotation of the Sun twists them into a spiral shape. Well below 1 AU, the spiral is not very tight, and the Parker field can be approximated by radial field lines.

A simple model representing the heliospheric magnetic field consists of a magnetic flux tube attached to the surface of the Sun and extending outwards along the Parker spiral. The flux tube cross-section scales as the inverse of the magnetic flux density. As plasma consists of charged particles, they are considered trapped to the confines of this flux tube, and travel according to the guiding centre approximation. As a simplification,
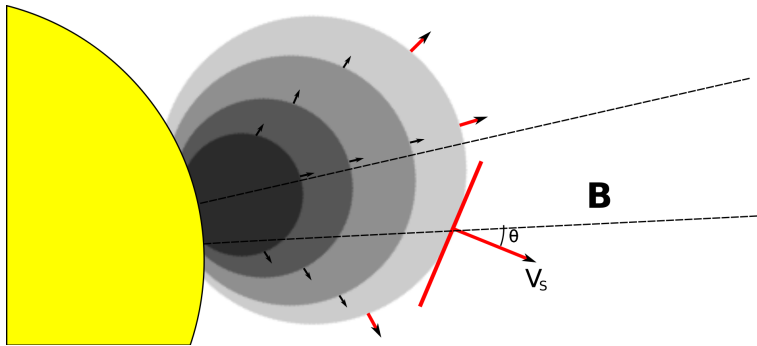
Figure 2.1: Sample schematic of a spherically expanding CME driving a shock front.

flux tubes can be considered infinitesimally thin. As an extensive coronal shock front propagates and intersects the flux tube in question, the shock parameters (shock-normal velocity V_s and shock-normal angle θ_{Bn}) can be tracked at the point of intersection. In **Paper I**, we investigated acceleration effectiveness of a decelerating coronal shock, and in **Paper III**, we investigated the effect of shock-normal angle θ_{Bn} on particle injection.

In shock physics, a commonly used initial frame of reference is the shock normal incidence frame (SNIF). In this frame, attached to the shock, the flow of plasma **u** in the upstream is directed perpendicular to the shock front. However, magnetic field lines are not necessarily aligned with the plasma flow. Here we choose the z-axis to be normal to the shock, the magnetic field to be in the zx-plane, and the y-axis to complement the right-hand system. In the SNIF, a motional electric field may be present, given by the equation

$$\mathbf{E} = -\frac{1}{c}\mathbf{u} \times \mathbf{B}, \tag{2.1}$$

directed along the y-axis. Next, we transform to a frame which moves along the shock front with a speed of $u_x = u_z B_x / B_z$. In this frame, known as the de Hoffmann – Teller (HT) frame, the magnetic field and plasma flow become aligned, and thus, the electric field disappears (de Hoffmann & Teller 1950). Transformation to this frame is valid as long as the transformation velocity is subluminal, which is usually not a very limiting factor
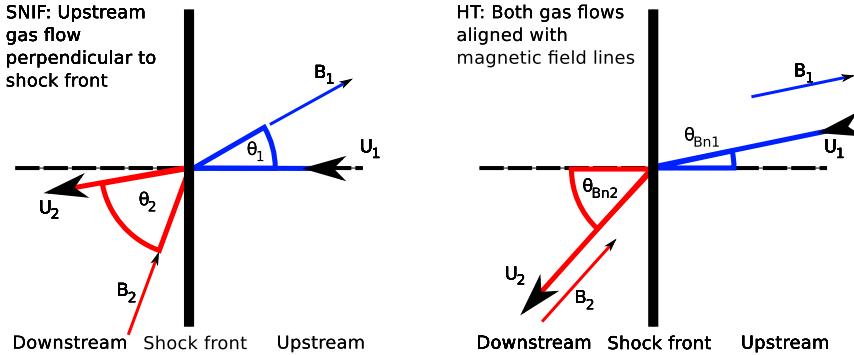
Figure 2.2: The shock normal incidence frame (SNIF, left) and the de Hoffmann – Teller frame (HT, right)

in heliophysical cases. It is easily shown that the alignment of plasma flow and magnetic field applies both in the upstream and the downstream of the shock. According to the co-planarity theorem, both upstream and downstream flows exist in a single plane within the SNIF and HT frames, and thus, the direction of the y-axis can be ignored. Examples of HT and SNIF frames are shown in figure 2.2.

2.2 Velocities and Mach numbers

A shock may be modelled as a disturbance propagating within a medium at a speed greater than the signal speed of the medium. As information of the disturbance cannot travel ahead of it, the upstream properties of the medium experience an abrupt change when encountering the disturbance, and thus, a shock forms. The sound speed in a space plasma is given as

$$v_{\mathrm{s}} = \sqrt{\frac{\gamma P}{\rho}} = \sqrt{\frac{\gamma k_{\mathrm{B}} T_{\mathrm{sum}}}{m_{\mathrm{p}}}}, \tag{2.2}$$

where $\gamma = 5/3$ is the polytropic index (or ratio of specific heats) describing a mono-atomic gas, P is the gas pressure, and ρ is the gas mass density. The temperature T_{sum} is the sum of electron and ion temperatures, as both particle populations contribute to total gas pressure. As with any shock waves, shocks in plasmas can be described by their Mach number. The

sonic Mach number, describing speed relative to signal speeds of sound waves, is defined as

$$M_{\mathrm{s}} = \frac{u_1}{v_{\mathrm{s}}}, \tag{2.3}$$

where u_1 is the HT-frame upstream gas flow speed towards the shock. In general, we refer to upstream quantities with subscript 1 and to downstream quantities with subscript 2.

In 1942, Hannes Alfvén postulated the existence of electromagnetic-hydrodynamic waves propagating through plasma (Alfvén 1942). The Alfvén wave is a non-compressional wave, caused by the freeze-in of magnetic field lines to the plasma. It consists of magnetic disturbances and results from the plasma attempting to return to a configuration with as little magnetic field line curvature as possible. The Alfvén speed

$$v_{\mathrm{A}} = \frac{B}{\sqrt{4\pi\rho}} \tag{2.4}$$

describes the speed at which Alfvénic waves travel parallel to the mean magnetic field. The Alfvénic Mach number M_{A} is given as

$$M_{\mathrm{A}} = \frac{u_1}{v_{\mathrm{A}}}. \tag{2.5}$$

We define the (upstream) plasma beta, or the ratio of gas pressure to magnetic pressure, as

$$\beta_1 = \frac{8\pi P_1}{B_1^2} = \frac{2}{\gamma}\frac{v_{\mathrm{s}}^2}{v_{\mathrm{A}}^2} = \frac{2}{\gamma}\frac{M_{\mathrm{A}}^2}{M_{\mathrm{s}}^2}. \tag{2.6}$$

In order for a coronal disturbance to develop into a fast mode shock, it must be super-Alfvénic in both the upstream and the downstream of the shock. This can be defined as the condition $r_{\mathrm{g}} < M_{\mathrm{A}}^2$, where r_{g} is the gas compression ratio.

2.3 Jump conditions

The transition from upstream plasma quantities to downstream plasma quantities at a shock results in a number of jump conditions, due to conser-

vation laws and Maxwell's equations, which can be expressed as continuous fluxes across the shock. In describing these jump conditions, we use square brackets [ ] to indicate the difference of the enclosed quantity on the different sides of the discontinuity. The shock-normal component is designated with the subscript n, with the tangential component designated with the subscript t. In deriving the conditions, we have ignored terms of viscosity and heat conduction, and use the gas adiabatic index γ. We also utilise the co-planarity theorem.

Instead of presenting jump conditions for a classical hydrodynamic shock, we choose to focus directly on the magneto-hydrodynamic (MHD) case. Shock jump conditions, known as the *Rankine-Hugoniot relations*, are reviewed in Salas (2007), and the equations can, in the HT frame, be written as follows:

1. Continuity of shock-normal mass flux

$$[\rho u_\mathrm{n}] = 0 \tag{2.7}$$

2. Continuity of shock-normal magnetic field component

$$[B_\mathrm{n}] = 0 \tag{2.8}$$

3. Continuity of shock-normal momentum flux

$$\left[P + \rho u_\mathrm{n}^2 + \frac{1}{8\pi} B_\mathrm{t}^2 \right] = 0 \tag{2.9}$$

4. Continuity of shock-transversal momentum flux

$$\left[\rho u_\mathrm{n} u_\mathrm{t} - \frac{1}{4\pi} B_\mathrm{n} B_\mathrm{t} \right] = 0 \tag{2.10}$$

5. Continuity of shock-normal energy flux

$$\left[\frac{1}{2} \rho u^2 u_\mathrm{n} + \frac{\gamma P}{(\gamma - 1)} u_\mathrm{n} \right] = 0 \tag{2.11}$$

6. Continuity of shock-transversal electric field

$$[u_\mathrm{t} B_\mathrm{n} - B_\mathrm{t} u_\mathrm{n}] = 0 \tag{2.12}$$

In this formulation, the momentum flux conservation equations include terms from the Maxwell stress tensor in addition to hydrodynamic terms. The shock-normal energy flux conservation should include a term for electromagnetic energy, which is defined by the shock-normal component of the Poynting vector $\mathbf{S} = \frac{c}{4\pi} \mathbf{E} \times \mathbf{B}$. In a well-conducting plasma and after

transformation to the HT frame, however, the Poynting vector reduces to zero, and thus, the energy transfer term is zero. The continuity equation for the shock-transversal electric field results from the induction equation for ideal MHD.

Solving the jump conditions for an MHD discontinuity can result in many different solutions, some of only limited interest. For shock waves, we require $u_\mathrm{n} \neq 0$, which excludes many trivial solutions from consideration. Solving jump conditions for a parallel shock ($u_\mathrm{t} = B_\mathrm{t} = 0$) is a great deal simpler, but in this chapter we consider the general case for an oblique shock in the HT frame. As suggested by Vainio & Schlickeiser (1999), we consider the parallel shock as a special case with a small but finite upstream tangential magnetic field (e.g., $B_\mathrm{t} = \delta B_1 = 0.003 B_0 = 0.003 B_\mathrm{n}$). This may represent the effect the magnetic pressure of Alfvénic turbulence has at the shock, and ensures a fast-mode shock.

2.4   Compression ratios

Important parameters in describing an MHD shock are the compression ratios for gas density and magnetic flux density. The gas compression ratio r_g can, using the continuity of mass flux, be used to relate the normal components of plasma flow velocity u, as

$$r_\mathrm{g} = \frac{\rho_2}{\rho_1} = \frac{u_{\mathrm{n},1}}{u_{\mathrm{n},2}}. \tag{2.13}$$

For reference, the gas compression ratio of a parallel shock in an adiabatic medium is given as

$$r_\mathrm{g} = \frac{\gamma + 1}{\gamma - 1 + 4\beta_1 \gamma^{-1} M_\mathrm{A}^{-2}}, \tag{2.14}$$

which limits the gas compression ratio to values $r_\mathrm{g} < 4$ (for $\gamma = 5/3$). This is the form used in **Paper II**.

Due to **B** being divergence-free, the shock-normal component of **B** is conserved. The ratio of magnetic flux densities, or the magnetic compression ratio, is

$$r_B = \frac{B_2}{B_1}. \tag{2.15}$$

In the de Hoffmann – Teller frame, plasma flow is parallel with the magnetic field, and flow speeds of plasma are related to shock compression ratios via

$$\frac{u_2}{u_1} = \frac{r_B}{r_g}. \tag{2.16}$$

2.5 Solving the gas compression ratio

The Rankine-Hugoniot equations can be used to solve the gas compression ratio at a shock of arbitrary shock-normal angle θ_{Bn}. The process is omitted here, as it has been introduced previously by Priest (1982). After a lengthy calculation, the shock conditions result in a cubic equation for the gas compression ratio r_g, given as

$$0 = (M_A^2 - r_g)^2 \left\{ \gamma \beta_1 r_g + M_A^2 \cos^2 \theta_{Bn}((\gamma - 1)r_g - (\gamma + 1)) \right\}$$
$$+ r_g M_A^2 \sin^2 \theta_{Bn} \left\{ (\gamma + (2 - \gamma)r_g)M_A^2 + r_g((\gamma - 1)r_g - (\gamma + 1)) \right\}, \tag{2.17}$$

where only parameters defined in the upstream of the shock are used. Instead of attempting to solve this cubic equation, we choose to reformulate it in the parametric form suggested by Vainio & Schlickeiser (1999). Defining $M_A^2 = r_g\{1 + \zeta\}$ allows reformulating (2.17) as

$$0 = \zeta^2 \left\{ \gamma \beta_1 + (1 + \zeta) \cos^2 \theta_{Bn}((\gamma - 1)r_g - (\gamma + 1)) \right\}$$
$$+ (1 + \zeta) \sin^2 \theta_{Bn} \left\{ (\gamma + (2 - \gamma)r_g)(1 + \zeta) + (\gamma - 1)r_g - (\gamma + 1) \right\}. \tag{2.18}$$

This is a linear equation in $r_g(\zeta)$, and can be rewritten as

$$r_g(\zeta) = \frac{(1 + \zeta) \left\{ \zeta^2(\gamma + 1) \cos^2 \theta_{Bn} + (1 - \gamma \zeta) \sin^2 \theta_{Bn} \right\} - \zeta^2 \gamma \beta_1}{(1 + \zeta) \left\{ \zeta^2(\gamma - 1) \cos^2 \theta_{Bn} + (1 + (2 - \gamma)\zeta) \sin^2 \theta_{Bn} \right\}} \tag{2.19}$$

$$M_A^2 = r_g(\zeta) \left\{ 1 + \zeta \right\}. \tag{2.20}$$

This allows running through the parameter space of $\zeta > -1$, using known values of β_1, θ_{Bn}, and $\gamma = 5/3$, until (2.20) results in the (also known) value of of M_A^2. This can be achieved easily by applying, for example, Newton's method.

As the original equation was cubic in nature, we examine the parameter space of available solutions. One solution can be found by setting

$M_A = r_g = 1$, which describes the motion of a shear Alfvén wave. In order to find the other solutions at $r_g = 1$, we simplify equation (2.17) into

$$0 = \zeta^2 \left\{ \gamma\beta_1 - 2(1+\zeta)\cos^2\theta_{Bn} \right\} + 2\zeta(1+\zeta)\sin^2\theta_{Bn}. \qquad (2.21)$$

Disregarding the solution at $\zeta = 0$ (the shear Alfvén wave), we can find the remaining root values at

$$M_A^2 = 1 + \zeta = \frac{1 + \frac{1}{2}\gamma\beta_1 \pm \sqrt{(1 + \frac{1}{2}\gamma\beta_1)^2 - 2\gamma\beta_1\cos^2\theta_{Bn}}}{2\cos^2\theta_{Bn}}. \qquad (2.22)$$

These solutions are for the fast (+) and slow (-) MHD waves.

In figure 2.3, we present a sample of the parameter space of solutions. Solutions resulting in $r_g < 1$ are rarefactions, not shocks. Solutions with $M_A^2 < 1$ represent slow shocks, and solutions for which $r_g > 1$ and $1 < M_A^2 < r_g$ hold true are intermediate shocks. The remaining solutions of $M_A^2 > r_g > 1$ represent fast shocks, where flows are super-Alfvénic. By finding the three solutions for $r_g(\zeta) = 1$ and initialising our ζ-running method at the largest of these values (and progressing in the positive direction), we can limit the found solutions to the parameter space of fast shocks.

2.6 Solving the magnetic compression ratio

The magnetic compression ratio r_B was given as the ratio of upstream and downstream magnetic flux densities. The change of the tangential magnetic field component can be derived from the jump conditions, and is given as

$$\frac{B_{t,2}}{B_{t,1}} = r_g \frac{M_A^2 - 1}{M_A^2 - r_g}. \qquad (2.23)$$

Combining this with equations (2.5), (2.8), and the decomposed form of (2.15), we find the square of r_B as

$$r_B^2 = \cos^2\theta_{Bn} + \sin^2\theta_{Bn} \left(\frac{M_A^2 - 1}{M_A^2 - r_g} r_g \right)^2. \qquad (2.24)$$
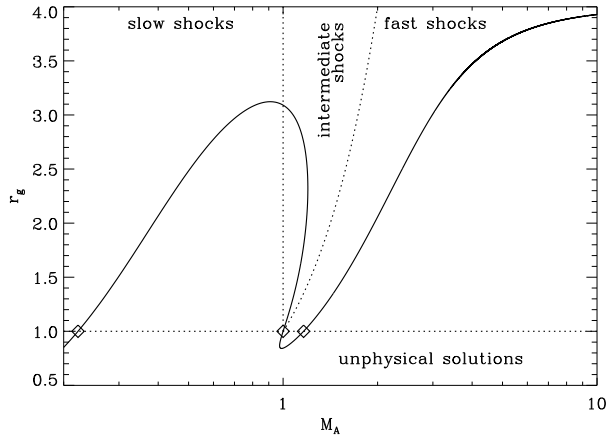
Figure 2.3: The parameter space for solutions to the equation linking gas compression ratio r_{g} and Alfvénic Mach number M_{A}. In this figure, solutions for increasing ζ are plotted as a curve with the values $\theta_{B\mathrm{n}} = 30°$, $\gamma = 5/3$, and $\frac{1}{2}\gamma\beta_1 = 0.05$. The three diamonds represent solutions at $r_{\mathrm{g}} = 1$. In the solution space of fast-mode shocks, r_{g} grows with increasing ζ.

2.7   The cross-shock potential

The solar wind contains ions and electrons in amounts which result in a macroscopically neutral plasma. A propagating shock disturbs the motion of particles it encounters, which can lead to charge imbalance over small spatial scales. Ions and electrons impacting the shock penetrate the downstream magnetic field according to their rigidity. The initial motion of protons, being heavier particles, extends further into the shock profile than that of electrons. This imbalance leads to an electrostatic potential jump associated with the shock front.

The cross-shock potential has been observed and modelled most extensively at the bow shock of the Earth (see, e.g., Hull et al. 2000 and Kuncic et al. 2002). One method of approximating the effect is a potential jump of

$$\Delta\Phi = \phi\frac{1}{2}m_{\mathrm{p}}\left(u_{\mathrm{n},1}^2 - u_{\mathrm{n},2}^2\right), \qquad (2.25)$$

which is proportional to the change of the normal component of proton ram energy with a fitting parameter $\phi \approx 0.12$ (Hull et al. 2000). The effect of a cross-shock potential on particle acceleration has, prior to this work, been investigated by, for example, Gedalin (1996) and Zank et al. (2001).

Chapter 3

Wave-particle interactions

Like any fluid medium, plasma can exhibit many kinds of fluctuations (see, e.g., Boyd & Sanderson 2003). Electromagnetic waves (x-rays, visible light, radio waves) can travel through plasma, as can pressure waves, sound waves and magnetic fluctuations. Plasma waves store, transport, and redistribute energy. As energetic particles travel along a helical trajectory through a magnetised and turbulent plasma, they interact with plasma waves at resonant wavenumbers. Waves cause particles to scatter, and scattering particles amplify Alfvén waves (Lee 1971).

3.1 MHD waves

A full description of plasma waves, being outside the scope of this thesis, is omitted in favour of MHD simplifications which describe wave properties adequately for our modelling efforts. Additional descriptions can be found in, for example, Kallenrode (2004) and Kulsrud (2005).

MHD waves arise from ion motion in the plasma, and are found at relatively low frequencies. Equations describing MHD result in *dispersion relations*, which describe wave-like solutions for plasma motion. Dispersion relations for a MHD wave propagating in an arbitrary direction result in three solutions: a fast mode, an intermediate mode, and a slow mode (see also: section 2.5). Wave propagation can be described with angular wave frequency ω, phase velocity $v_p = \omega/k$, group velocity $v_g = \partial\omega/\partial k$, wave number k, and direction of the wave vector $\mathbf{k}$.

The dispersion relation for fast $(+)$ and slow $(-)$ MHD waves is

$$\frac{\omega^2}{k^2} = \frac{v_A^2 + v_s^2}{2} \pm \frac{1}{2}\sqrt{(v_A^2 - v_s^2)^2 + 4v_A^2 v_s^2 \sin^2\theta}, \tag{3.1}$$

where θ is the angle between $\mathbf{k}$ and $\mathbf{B}_0$. The dispersion relation for the intermediate wave is

$$\frac{\omega}{k} = v_{\mathrm{A}} \cos\theta. \tag{3.2}$$

The solutions show that slow and intermediate MHD waves do not propagate perpendicular to $\mathbf{B}_0$. At the perpendicular limit, the fast MHD wave reduces to the *magnetosonic wave*, propagating with the phase speed $v_{\mathrm{p}} = \sqrt{v_{\mathrm{A}}^2 + v_{\mathrm{s}}^2}$ with $\mathbf{k} \perp \mathbf{B}_0$. At the parallel limit, with $\mathbf{k} \parallel \mathbf{B}_0$, the fast MHD wave propagates at a phase speed equal to the greater of v_{s} and v_{A}, whereas the slow MHD wave propagates at a phase speed equal to the lesser of v_{s} and v_{A}. At the parallel limit, the intermediate MHD wave propagates at the phase speed v_{A}.

We now consider the incompressible limit of MHD, which can be physically described as v_{s} (or β from eq. 2.6) being very large. At this limit, pressure disturbances propagate at very fast speeds, which results in fast MHD waves propagating near-instantaneously. At the lowest order, incompressible intermediate and slow MHD waves propagate at the same phase speed $v_{\mathrm{p}} = v_{\mathrm{A}} \cos\theta$. At this limit, they differ mainly through polarisation.

The intermediate MHD wave is equivalent to an *Alfvén wave* (Alfvén 1942), alternatively called a shear Alfvén wave. Shear Alfvén waves are polarised, i.e., have first-order magnetic disturbances $\delta\mathbf{B}$, in the direction perpendicular to both $\mathbf{k}$ and $\mathbf{B}_0$. The incompressible limit of the slow MHD wave is called the pseudo Alfvén wave, and it is polarised in the $\mathbf{k} - \mathbf{B}_0$ plane, perpendicular to $\mathbf{k}$. Waves which have both $\mathbf{k} \parallel \mathbf{B}_0$ and $\delta\mathbf{B} \perp \mathbf{B}_0$ are referred to as the *slab mode*.

3.1.1 Helicity, polarisation, and oscillation frequency

Alfvén waves propagating at angles oblique to the background magnetic field are always linearly polarised. However, parallel Alfvén waves can be formulated as a combination of left-handed (LH) and right-handed (RH) modes. Handedness is defined according to rotation around the direction of the mean magnetic field. In the frame of the propagating wave, the spatial helical form of the wave translates to a definition of left-handed or right-handed magnetic helicity. The sign of the wavenumber k indicates helicity, with $k > 0$ for RH waves and $k < 0$ for LH waves. In addition, the vector $\delta\mathbf{B}$ rotates in the frame of the plasma in either the right-handed or left-handed

direction around the mean magnetic field. The magnetic polarisation of the wave is defined by the sign of the frequency ω, which is positive for LH rotating waves and negative for RH rotating waves. As a result of these two definitions, a wave can propagate either parallel ($\mathbf{k} \uparrow\uparrow \mathbf{B}_0$) or anti-parallel ($\mathbf{k} \uparrow\downarrow \mathbf{B}_0$) to the mean magnetic field. Parallel waves propagate at velocity $\omega/k = v_\mathrm{A}$ and anti-parallel waves at velocity $\omega/k = -v_\mathrm{A}$.

When observing an Alfvén wave from a frame moving at speed $v_\parallel$ along the magnetic field, the relativistic Doppler-shifted oscillation frequency ω' of a given wave is observed as

$$\omega' = \gamma_\parallel(\omega - k_\parallel v_\parallel), \tag{3.3}$$

where $\gamma_\parallel = 1/\sqrt{1 - v_\parallel^2/c^2}$ and the sign of ω' represents the observed magnetic polarity in the moving frame. Note that in different applications, the naming conventions of forward or backward propagating waves can differ. In the heliocentric frame, waves propagating outwards from the Sun are often referred to as forward propagating waves, but when considering wave transfer at a shock crossing, it is customary to define a forward propagating wave as one propagating in the same direction as the plasma does in the shock frame. In a general case, the cross-helicity H_c, used to describe the ratio of wave intensities of forward-moving (I_+) and backward-moving (I_-) waves, is given as

$$H_\mathrm{c} = \frac{I_+ - I_-}{I_+ + I_-}. \tag{3.4}$$

3.2   Particle transport and scattering

3.2.1   Quasi-linear theory

The most commonly adopted method of quantifying the scattering of energetic particles off Alfvén waves is known as quasi-linear theory (QLT), as introduced by Jokipii (1966). The initial assumption of QLT is to deduce the motion of particles in circumstances where the effects of scattering cause minimal disturbances to the gyropath of the particle. Magnetic fluctuations are described as a linear first-order approximation of the form $\mathbf{B} = \mathbf{B}_0 + \delta\mathbf{B}$, where the amplitude of magnetic fluctuations is $\delta B \ll B_0$. In the basic formulation, with $\mathbf{k} \parallel \mathbf{B}_0$, only the perpendicular magnetic

fluctuation component $\delta\mathbf{B}_\perp$ is considered, describing, for example, parallel Alfvén waves.

Examining the scattering angle of a particle with mass m and charge q through change of the pitch-angle cosine $\mu = \cos\theta = v_\parallel/v$ allows us to formulate the change of μ through the Lorentz force as

$$v\dot\mu = \dot{v}_\parallel = \frac{q}{mc}\delta B_\perp(\mathbf{r}, t)v_\perp \sin\phi, \tag{3.5}$$

where ϕ is the angle between the perpendicular velocity component $\mathbf{v}_\perp$ and the perpendicular magnetic fluctuation component $\delta\mathbf{B}_\perp$. Additionally, we have used the assumption of conservation of energy in the wave frame. This holds, for example, for MHD waves, where there is no electric field related to the wave.

Choosing the coordinates so that $\mathbf{B}_0 \uparrow\uparrow \hat{\mathbf{e}}_z$, the equation describing a background magnetic field $\mathbf{B}_0$ and a circularly polarised parallel Alfvén wave of frequency ω in the frame of plasma with $\mathbf{k} \parallel \mathbf{B}_0$ becomes

$$\mathbf{B} = B_0\hat{\mathbf{e}}_z + \delta B \left(\hat{\mathbf{e}}_x - \imath\hat{\mathbf{e}}_y\right) e^{\imath(kz-\omega t-\phi')}, \tag{3.6}$$

where ϕ' is a phase constant. The velocity of a particle following a gyropath along the background magnetic field $\mathbf{B}_0$ can be separated into components in a similar way, resulting in

$$\mathbf{v} = v_\parallel\hat{\mathbf{e}}_z + v_\perp \left(\hat{\mathbf{e}}_x - \imath\hat{\mathbf{e}}_y\right) e^{\imath(-\Omega t-\Phi')}, \tag{3.7}$$

where Φ' is a phase constant, and $\Omega > 0$ for a positively charged particle. For a particle propagating with parallel speed $v_\parallel$ and gyrofrequency Ω, we find $z = v_\parallel t$. The phase difference $\phi' - \Phi'$ can be solved from the exponential oscillation terms of equations (3.6) and (3.7). If the phase difference is constant, the wave and the particle are in resonance, according to the condition $\Omega = \omega - kv_\parallel$. For all non-resonant frequencies, over an extended period of time, the quasilinear approximation results in the Lorentz force contributions cancelling each other out.

For resonant interactions, the phase difference $\phi'-\Phi'$ defines the strength and direction of the Lorentz force along the z-axis. If $(\phi' - \Phi') = 0$ or π, $\mathbf{v}_\perp \parallel \delta\mathbf{B}_\perp$ and $\dot{v}_\parallel = 0$. $(\phi' - \Phi') = \pm\pi/2$ leads to maximal acceleration in the direction $\pm\hat{\mathbf{e}}_z$. Thus, particles can scatter off resonant waves in both directions in μ-space.

Derivations of QLT for waves with $\mathbf{k}$ not parallel with $\mathbf{B}_0$ are possible (see, e.g., Schlickeiser 2002), but outside the scope of this thesis.

3.2.2 The Fokker-Planck equation and focused transport

The evolution of particle populations can be described through kinetic theory, as introduced in section 1.7. The Fokker-Planck equation contains a selection of diffusion coefficients, describing the evolution of the particle population in phase space due to, for example, collisions and scattering off magnetic fluctuations such as Alfvén waves. Additionally, the particle distribution experiences adiabatic cooling due to gas expansion (Skilling 1971, 1975) and pitch-angle focusing (Earl 1976; Ng & Wong 1979). Pitch-angle focusing occurs due to conservation of magnetic moment as the flux tube expands and magnetic flux density decreases.

In this section, we modify the Fokker-Planck equation (1.6) in order to describe particle population evolution as a *focused transport equation*. We include terms describing magnetic focusing and pitch-angle scattering off Alfvén waves. We designate values given in the fixed inertial frame, attached to the Sun, as plain $(\mathbf{p}, \mathbf{r}, t)$ and values given in the frame of scattering centres as primed $(\mathbf{p}', \mathbf{r}', t')$. In the inertial frame, scattering centres propagate at speed $V = u_{\mathrm{sw}} + v_{\mathrm{A}}$, where u_{sw} is the solar wind speed.

We have excluded effects due to solar rotation and IMF curvature, assuming radial solar wind flow and a radial magnetic field. The assumption of a radial field is reasonable within the solar corona and the innermost parts of the heliosphere, but not at, for example, 1 AU. A more detailed discussion, including effects due to solar rotation and magnetic field curvature, can be found in Ruffolo (1995).

Particles experience adiabatic changes to their direction of momentum both in the inertial frame (due to magnetic focusing) and in the frame of scattering centres (due to pitch-angle scattering off Alfvén waves). The resultant effect of adiabatic deceleration can also include minor terms due to, for example, changes in solar wind speed u_{sw} or non-radial geometry.

Using the flux tube cross-sectional area $\mathcal{A} \propto B^{-1}$, the heliocentric distance r, and the spatial scale length of the mean magnetic field L for which

$$\frac{1}{L} = -\frac{1}{B}\frac{\partial B}{\partial r} = \frac{1}{\mathcal{A}}\frac{\partial \mathcal{A}}{\partial r}, \tag{3.8}$$

the rate of change for particle pitch-angle μ in the fixed frame due to magnetic focusing can be written as (Ruffolo 1995)

$$\dot{\mu} = \frac{v}{2L}(1 - \mu^2). \tag{3.9}$$

In the frame of scattering centres, equation (3.9) becomes

$$\dot{\mu}' = \frac{(1 - \mu^2)}{2L}\left(v' + \mu'V\left(1 - \frac{v'^2}{c^2}\right)\right). \tag{3.10}$$

Adiabatic deceleration (often described as average change of momentum due to gas expansion) is derived as

$$\dot{p}' = -\frac{Vp'}{2L}\left(1 - \mu'^2\right). \tag{3.11}$$

Due to the small magnitude of the effect, adiabatic deceleration can often be ignored for simplicity. The pitch-angle altering effect due to magnetic focusing should not, however, be ignored.

We now rewrite equation (1.6) in *mixed coordinates*. The number of particles found at a point in phase-space is defined as

$$F(\mathbf{p}, \mathbf{r}, t)\, \mathrm{d}^3\mathbf{r}\, \mathrm{d}^3\mathbf{p} = F'(\mathbf{p}', \mathbf{r}', t')\, \mathrm{d}^3\mathbf{r}'\, \mathrm{d}^3\mathbf{p}' = F^*(\mathbf{p}', \mathbf{r}, t)\, \mathrm{d}^3\mathbf{r}\, \mathrm{d}^3\mathbf{p}',$$

where the final form $F^*(\mathbf{p}', \mathbf{r}, t)$ is given in mixed coordinates. We choose to use the one-dimensional guiding centre approximation and ignore terms $\mathcal{O}(vV/c^2)$, noting that $F^*(p', \mu', r, t) \approx F(p, \mu, r, t)$ (see, e.g., Gleeson & Webb 1980). Using this notation, we derive an equation describing focused transport (see also Roelof 1969, Kunstmann 1979, and Ng et al. 2003), resulting in the form

$$\frac{\partial F^*_\alpha}{\partial t} + \left(v'\mu' + V\right)\frac{\partial F^*_\alpha}{\partial r} + \frac{(1 - \mu'^2)}{2L}\left(v' + \mu'V\right)\frac{\partial F^*_\alpha}{\partial \mu'}$$
$$-\frac{(1 - \mu'^2)}{2L}Vp'\frac{\partial F^*_\alpha}{\partial p'} - \frac{\partial}{\partial \mu'}D_{\mu'\mu'}\frac{\partial F^*_\alpha}{\partial \mu'} = 0. \tag{3.12}$$

In this equation, the second term describes particle streaming and solar wind convection, the third term describes pitch-angle focusing due to the diverging magnetic field, the fourth term describes adiabatic deceleration and the fifth term describes pitch-angle scattering off resonant Alfvén waves.

The benefit of using mixed coordinates is that by choosing to examine particle scattering in the frame of scattering centres, it can be described in an adiabatic manner through the single Fokker-Planck coefficient $D_{\mu'\mu'}$.

An alternative method of describing the large-scale spatial and temporal evolution of a quasi-isotropic ($f \approx f_0(\mathbf{r}, p, t)$) particle population is Parker's equation (see, e.g., Parker 1965b and Jokipii & Parker 1970). Instead of describing scattering off Alfvénic turbulence through $D_{\mu\mu}$, it is possible to reformulate scattering according to the particle mean free path $\lambda = 3D_\parallel/v$ (see also Hasselmann & Wibberenz 1968). This yields the spatial diffusion coefficient (Earl 1974)

$$D_\parallel = \frac{v^2}{8} \int_{-1}^{+1} \frac{(1-\mu^2)^2}{D_{\mu\mu}} d\mu. \tag{3.13}$$

For an isotropic particle population, adiabatic deceleration is described as

$$\langle \dot{p} \rangle = -\frac{p}{3} \nabla \cdot \mathbf{V}. \tag{3.14}$$

With this formulation, Parker's equation describing a quasi-isotropic population within an expanding radial flux tube becomes

$$\frac{\partial f_0}{\partial t} + V \frac{\partial f_0}{\partial r} - \frac{p}{3} \frac{1}{\mathcal{A}} \frac{\partial}{\partial r} (\mathcal{A}V) \frac{\partial f_0}{\partial p} = \frac{1}{\mathcal{A}} \frac{\partial}{\partial r} \left(\mathcal{A} D_\parallel \frac{\partial f_0}{\partial r} \right). \tag{3.15}$$

Following Kocharov et al. (1996) and Kocharov et al. (1998), and using the linear density $n = \mathrm{d}^2 N/\mathrm{d}r\,\mathrm{d}p = 4\pi p^2 \mathcal{A} f_0$, we can reformulate Parker's equation as

$$\frac{\partial n}{\partial t} + \frac{\partial}{\partial r} \left[\left(V + \frac{D_\parallel}{L} \right) n \right] - \frac{\partial}{\partial p} \left[\frac{p}{3} \left(\frac{\partial V}{\partial r} + \frac{V}{L} \right) n \right] = \frac{\partial}{\partial r} \left(D_\parallel \frac{\partial n}{\partial r} \right), \tag{3.16}$$

which allows us to examine how, according to the second term, amplified turbulence (with $D_\parallel \approx 0$) can cause even high-energy particle populations to be convected at the speed of scattering centres.

Focused diffusion equations or reformulations of Parker's equation allow theoretical assessment of particle population evolution, but cannot be extended to account for self-consistent wave generation and particle trapping. As such, they are presented for comparison and reference. The Monte

Carlo method of calculating particle transport, as presented in chapter 5, is a better tool for self-consistent acceleration simulations.

3.2.3 Fokker-Planck coefficients

Full derivation of Fokker-Planck coefficients is beyond the scope of this thesis, and we direct the interested reader to Schlickeiser (1989) and Schlickeiser (2002). For particle scattering off Alfvén waves, the Fokker-Planck coefficient is given as (Schlickeiser 2002)

$$D_{\mu\mu} = \frac{2\Omega^2}{B_0^2}\left(1-\mu^2\right)\sum_{j=\pm 1}\sum_{n=-\infty}^{\infty}\int \mathrm{d}^3k\,\mathcal{R}_j$$

$$\left[1-\frac{\mu\omega_j}{k_\parallel v}\right]^2\left(\frac{nJ_n(v_\perp k_\perp/\Omega)}{v_\perp k_\perp/\Omega}\right)^2 P_{RR}^j(\mathbf{k}), \qquad (3.17)$$

where J_n is the Bessel function. The resonance function, with the assumption of negligible damping, is presented here as

$$\mathcal{R}_j = \pi\delta(v_\parallel k_\parallel - jk_\parallel v_\mathrm{A} + n\Omega), \qquad (3.18)$$

where δ is the Kronecker delta.

For the term $n = 0$, the Fokker-Planck scattering coefficient is zero. For $n \neq 0$ we can use the magnetostatic approach, assuming particles propagate at velocities $v \gg v_\mathrm{A}$. This results in the resonance condition being reduced to $\mathcal{R} = \pi\delta(v_\parallel k_\parallel + n\Omega)$, as well as the simplification

$$\left[1-\frac{\mu\omega_j}{k_\parallel v}\right]^2 \approx 1.$$

In this way the scattering coefficient for Alfvénic turbulence becomes

$$D_{\mu\mu} = \frac{2\pi\Omega^2}{B_0^2}\left(1-\mu^2\right)\sum_{n=-\infty}^{\infty}\int \mathrm{d}^3k\,\delta(k_\parallel v_\parallel + n\Omega)\left(\frac{nJ_n(v_\perp k_\perp/\Omega)}{v_\perp k_\perp/\Omega}\right)^2 P_{xx}(\mathbf{k}).$$

$$(3.19)$$

We define the denominator, and the argument of the Bessel function, as $x = v_\perp k_\perp/\Omega$. As for parallel Alfvén waves $x = 0$, we investigate the Bessel

function as a series

$$J_\alpha(x) = \sum_{m=0}^{\infty} \frac{(-1)^m}{m!\,\Gamma(m+\alpha+1)} (\tfrac{1}{2}x)^{2m+\alpha}, \qquad (3.20)$$

where the first term is seen to be $\frac{1}{4}x$ and all other terms include higher powers of the argument x. Thus, for purely parallel Alfvén waves, only the term $n = 1$ survives, the terms $x = v_\perp k_\perp/\Omega$ cancel out, and the relevant part of equation (3.19) becomes $\left(\frac{1}{4}\right)^2$.

The Fokker-Planck coefficient for particles scattering off pseudo Alfvén waves (after a similar derivation) is given as (see **Paper IV** and Schlickeiser 2002)

$$D_{\mu\mu} = \frac{2\pi\Omega^2}{B_0^2}\left(1-\mu^2\right)\sum_{n=-\infty}^{\infty}\int \mathrm{d}^3k\,\delta(k_\parallel v_\parallel + n\Omega)\left(J_n'(v_\perp k_\perp/\Omega)\right)^2 P_{xx}(\mathbf{k},$$

$$(3.21)$$

where J_n' is the derivative of J_n.

3.3 Scattering rate and pitch-angle dependence

The energetic particle scattering rate, $\nu = 2D_{\mu\mu}/(1-\mu^2)$, can be used to link particle scatterings with the magnetic fluctuations they experience. In the simplest case of slab-mode turbulence (i.e., fluctuations with wave vectors aligned with the background magnetic field), the resonant wavenumber of the scattering particle is $k_\mathrm{r} = \Omega/v_\parallel$. According to Schlickeiser (1989), we define the particle mean free path as

$$\lambda = \frac{3v}{8}\int_{-1}^{+1}\frac{(1-\mu^2)^2}{D_{\mu\mu}}d\mu. \qquad (3.22)$$

Here the standard quasi-linear theory (SQLT) pitch-angle diffusion coefficient is (Vainio & Laitinen 2001)

$$D_{\mu\mu} = \frac{\pi}{2}\frac{\Omega^2}{B^2}(1-\mu^2)\frac{I(\Omega/(v\mu))}{|v\mu|}, \qquad (3.23)$$

which is described in terms of wave intensity $I(k)$, which is related to the magnitude of magnetic fluctuations as $\int I(\mathbf{k})\,\mathrm{d}^3k = \langle \delta B^2 \rangle$. For vanishing magnetic helicity, $I(k) = I(-k)$, the wave intensity $I(k)$ can be related with the wave power spectrum as

$$|k|I(k) = \frac{1}{2}fP(f). \tag{3.24}$$

Combining equations (3.23) and (3.24) results in the pitch-angle diffusion coefficient

$$D_{\mu\mu} = \frac{\pi}{4}\Omega(1 - \mu^2)\frac{f_{\mathrm{r}}P(f_{\mathrm{r}})}{B^2}. \tag{3.25}$$

Inserting this into the definition of scattering frequency results in

$$\nu = \frac{\pi}{2}\Omega\frac{f_{\mathrm{r}}P(f_{\mathrm{r}})}{B^2}. \tag{3.26}$$

This depends on the particle pitch-angle only through the resonant wave frequency

$$f_{\mathrm{r}} = \frac{\Omega}{2\pi}\frac{V}{v|\mu|}, \tag{3.27}$$

where V is the propagation speed of resonant waves.

This pitch-angle-dependent scattering poses a challenge. Particles with values of μ close to zero are resonant with fluctuations associated with very large wavenumbers, so require the presence of high frequency waves in order to experience significant scattering. Alfvénic waves in the inner heliosphere contain very little power at high frequencies, due to dissipation effects, and thus form the so-called resonance gap. If particles are unable to scatter across hemispheres past $\mu = 0$, they cannot become isotropic, which is a prerequisite for diffusive type particle transport characterised by a mean free path. Work on extending QLT in order to bridge the resonance gap has been published in, for example, Ng & Reames (1995).

In order to bridge the resonance gap, and simplify wave amplification calculations (see section 3.4), we alter the SQLT resonance condition ac-

cording to Lee (1983), resulting in

$$f_{\mathrm{r}} = f_{\mathrm{cp}} \frac{V}{v}, \tag{3.28}$$

where $f_{\mathrm{cp}} = \Omega/(2\pi)$. This is equivalent to applying the restriction of $|\mu| = 1$ to equation (3.27).

In **Paper IV**, we discuss the reliability of QLT by comparing it with full-orbit simulations using MHD-generated turbulence, and find that QLT overestimates the pitch-angle dependence of particle scattering, lending credibility to this approximation. We also refer the reader to Ng & Reames (1995), where Extended QLT (EQLT) was formulated with the same target of crossing the resonance gap.

3.4   Wave amplification via particle scattering

Energetic particles scattering off Alfvén waves conserve their energy in the wave frame, experiencing only deflection. As waves propagate at speed v_{A} in relation to the solar wind plasma, particle energy in the solar wind plasma frame is not conserved (see figure 3.1). Each small-angle particle scattering changes the plasma-frame particle energy by $\Delta E_{\mathrm{p}} = v_{\mathrm{A}} p \Delta\mu$, where p and $\Delta\mu$ are measured in the wave frame. Thus, conservation of total plasma-frame energy results in energy deposition to turbulence, with a change of the resonant wave energy of $\Delta E_{\mathrm{w}} = -v_{\mathrm{A}} p \Delta\mu$. In this section, we detail the connection between wave amplification and energetic particle scatterings, as formulated in Vainio (2003), and extend it to account for minor ions.

Summing up all energy deposition contributions in a certain spatial position, the rate of change for wave energy density is found as

$$\frac{\mathrm{d}U_{\mathrm{w}}}{\mathrm{d}t} = -\int v_{\mathrm{A}} p \frac{\langle \Delta\mu \rangle}{\Delta t} f_\alpha(\mathbf{r}, \mathbf{p}, t) \, \mathrm{d}^3 p, \tag{3.29}$$

where f_α is the ion distribution function. Here the change in pitch-angle is given by the Fokker-Planck coefficient $\langle \Delta\mu \rangle / \Delta t = \partial D_{\mu\mu}/\partial\mu$, where $D_{\mu\mu} = \frac{1}{2} \langle (\Delta\mu)^2 \rangle / \Delta t$ is the particle pitch-angle diffusion coefficient. In

QLT (Jokipii 1966), it is defined (following the notation of Vainio 2003) as

$$D_{\mu\mu} = \frac{\pi}{4}\Omega(1 - \mu^2)\frac{|k_{\rm r}|W(k_{\rm r})}{U_B}, \tag{3.30}$$

where $k_{\rm r}$ is the resonant wavenumber. The energy associated with the magnetic field, $U_B = B^2/8\pi = \frac{1}{2}v_{\rm A}^2 n_{\rm p} m_{\rm p}$, is calculated assuming that all solar wind ions are protons.

Rewriting equation (3.29) in a cylindrically symmetrical form, and making the substitution $d^3p = p^2 \sin\theta \, dp \, d\theta \, d\phi = -2\pi p^2 \, dp \, d\mu$, results in

$$\frac{dU_{\rm w}}{dt} = \iint 2\pi v_{\rm A} p^3 \frac{\partial D_{\mu\mu}(k_{\rm r})}{\partial \mu} f_\alpha(\mathbf{r}, \mathbf{p}, t) \, d\mu \, dp. \tag{3.31}$$

Examining $\int \frac{\partial D_{\mu\mu}}{\partial \mu} f_\alpha(\mathbf{r}, \mathbf{p}, t) \, d\mu$ through partial integration yields

$$\int_{-1}^{+1} \frac{\partial D_{\mu\mu}}{\partial \mu} f_\alpha(\mathbf{r}, \mathbf{p}, t) \, d\mu = \left.\int^{+1}\right|_{\mu=-1} D_{\mu\mu} f_\alpha(\mathbf{r}, \mathbf{p}, t) - \int_{-1}^{+1} D_{\mu\mu}\frac{\partial f_\alpha(\mathbf{r}, \mathbf{p}, t)}{\partial \mu} \, d\mu. \tag{3.32}$$

According to equation (3.30), we find $D_{\mu\mu}(\mu = \pm 1) \equiv 0$, and the first term on the RHS equals zero.

Assuming the existence of only slab-mode outward-propagating Alfvén waves, we can write the wave energy density as $U_{\rm w} = \int W(k) \, dk$, where $W(\mathbf{r}, k, t) \, dk$ is the energy density of waves with a wavenumber in the range from k to $k+dk$. Since the pitch-angle diffusion coefficient $D_{\mu\mu}$ is calculated for only a single wavenumber $k_{\rm r}$, we can use equation (3.32) and rewrite equation (3.31) to include integration over all wavenumbers using the delta function. This results in the form

$$\int \frac{dW(k)}{dt} dk = -\iiint \delta(k - k_{\rm r}) \, 2\pi v_{\rm A} p^3 D_{\mu\mu}(k)\frac{\partial f_\alpha(\mathbf{r}, \mathbf{p}, t)}{\partial \mu} \, d\mu \, dp \, dk. \tag{3.33}$$

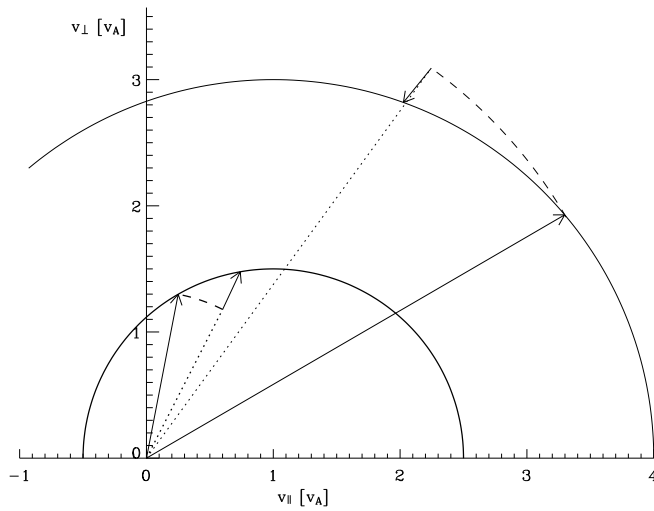Since both sides are integrated over k, we can limit our examination to the integrands, which must be equal.

Figure 3.1: Plasma frame velocity vectors for particles scattering off Alfvén waves. Energy is conserved in the frame of waves, propagating at speed v_A, resulting in addition or subtraction of energy in the plasma frame. Long arrows represent pre-scattering velocities, shorter arrows represent the speed difference in the plasma frame.

Combining equations (3.30) and (3.33), we find

$$\frac{\mathrm{d}W(k)}{\mathrm{d}t} = -\iint \delta(k - k_\mathrm{r}) \frac{\pi^2 v_\mathrm{A} p^3 \Omega}{2 U_B}(1 - \mu^2)|k|W(k)\frac{\partial f_\alpha}{\partial \mu}\,\mathrm{d}\mu\,\mathrm{d}p, \quad (3.34)$$

which can be transformed into

$$\frac{1}{W}\frac{\mathrm{d}W}{\mathrm{d}t} = -\iint \delta(k - k_\mathrm{r})|k|\frac{\pi^2 p^3 \Omega}{v_\mathrm{A} n_\mathrm{p} m_\mathrm{p}}(1 - \mu^2)\frac{\partial f_\alpha}{\partial \mu}\,\mathrm{d}\mu\,\mathrm{d}p, \quad (3.35)$$

where the resonant wavenumber $k_\mathrm{r} = \Omega/v\mu$.

Next, we replace $\delta(k + \Omega/v\mu)$ with $\frac{1}{2}\delta(|k| - \Omega/v)$. This simplification of the quasi-linear resonance condition ignores the μ-dependence, as suggested by, for example, Skilling (1975), Bell (1978), and Lee (1983). Next we use partial integration to find

$$\int_{-1}^{+1}(1 - \mu^2)\frac{\partial f_\alpha}{\partial \mu}\,\mathrm{d}\mu = \left/\!\!\!\!\!\!\!\!\!{\vphantom{\int_{-1}^{+1}}}\right._{\mu=-1}^{\,+1}(1 - \mu^2)f_\alpha - \int_{-1}^{+1}(-2)\mu f_\alpha\,\mathrm{d}\mu, \quad (3.36)$$

which allows us to obtain the growth rate

$$\Gamma_\mathrm{w}(k) = \frac{1}{W}\frac{\mathrm{d}W}{\mathrm{d}t} = -\frac{\pi^2 \Omega}{v_\mathrm{A} n_\mathrm{p} m_\mathrm{p}}\iint p^3 \mu|k|\delta(|k| - \Omega/v)f_\alpha\,\mathrm{d}\mu\,\mathrm{d}p. \quad (3.37)$$

We now choose the resonant relativistic momentum $p = \gamma m v$ as the independent parameter, with $v = \Omega/|k|$. We define a constant $K_0 = \gamma m\Omega$ and transform the integral over p into an integral over k, as the Dirac delta function is defined in k-space. Now $\mathrm{d}p = \mathrm{d}(K_0/|k|) = -\frac{K_0}{|k|^2}\mathrm{d}|k|$, $|k| = K_0/p$ and we find

$$- \frac{\pi^2}{v_{\rm A} n_{\rm p} m_{\rm p}} \iint p^3 \mu \Omega |k| \delta(|k| - \Omega/v) f_\alpha \, {\rm d}\mu \, {\rm d}p$$

$$= \frac{\pi^2}{v_{\rm A} n_{\rm p} m_{\rm p}} \iint \frac{K_0^5}{|k|^4} \frac{\mu}{\gamma m} \delta(|k| - \Omega/v) f_\alpha \, {\rm d}\mu \, {\rm d}|k|$$

$$= \frac{\pi^2}{v_{\rm A} n_{\rm p} m_{\rm p}} \int \frac{v^4}{\Omega^4} K_0^5 \frac{\mu}{\gamma m} f_\alpha \, {\rm d}\mu$$

$$= \frac{\pi^2 K_0}{v_{\rm A} n_{\rm p} m_{\rm p}} \int p^4 \frac{\mu}{\gamma m} f_\alpha \, {\rm d}\mu$$

$$= \frac{\pi}{2} \frac{\gamma m \Omega}{v_{\rm A} n_{\rm p} m_{\rm p}} 2\pi \int p^3 \mu v f_\alpha \, {\rm d}\mu.$$

Now we can note that $S_\alpha(\mathbf{r}, p, t) = 2\pi \int_{-1}^{+1} p^2 \mu v f_\alpha(\mathbf{r}, p, t)) \, {\rm d}\mu$ is the streaming of ions, i.e. the net number of particles crossing a point in space per unit area (perpendicular to the magnetic field), unit momentum, and unit time, at (wave-frame) momentum p. Thus, with the additional definition of the (non-relativistic) ion cyclotron frequency $\Omega_{\rm c} = \gamma \Omega = qB/(mc)$, we can formulate the turbulence growth rate $\Gamma_{\rm w}(k_{\rm r})$ as

$$\Gamma_{\rm w}(k_{\rm r}) = \frac{\pi}{2} \Omega_{\rm c} \frac{m}{m_{\rm p}} \frac{p S_\alpha(\mathbf{r}, p, t)}{n_{\rm p} v_{\rm A}}, \tag{3.38}$$

where $k_{\rm r} = \Omega/v$ is the wavenumber resonant with particles of momentum p. This allows for a numerically efficient way of coupling particle scatterings (measured as streaming) with turbulence generation, which is especially useful in self-consistent Monte Carlo simulations.

3.5   Wave cascading

Alfvén waves interact and transfer energy across wavenumber space through a process known as cascading. Non-linear interactions between three Alfvén waves (Shebalin et al. 1983; Goldreich & Sridhar 1995) or two Alfvén waves and a sound wave (Chin & Wentzel 1972; Vainio & Spanier 2005) alter the inertial range spectrum of turbulence. SEP scattering can amplify turbulence in the inertial range, as described in section 3.4. At the ion and electron cyclotron frequencies, energy from turbulence begins to increasingly

dissipate into solar wind thermal energy (Hollweg 1986). Thus, cascading from small to large wavenumbers is a strong candidate for explaining coronal heating (Cranmer et al. 2007 and references therein). Inverse cascading from large to small wavenumbers is also possible, as presented in Spanier & Vainio (2008).

Spatial gradients leading to interactions at large scales cause "stirring", acting as a energy source at low wavenumbers. The triple correlation timescale τ_3 represents how fluctuations of similar size interact with each other. The Alfvén timescale is the crossing time $\tau_A = \lambda/v_A$, and the nonlinear timescale is the eddy-turnover time $\tau_{NL} = \lambda/\delta u$, where δu is the velocity amplitude of plasma fluctuations.

The two best known analytical solutions for the inertial range spectrum of Alfvénic turbulence in the solar wind are the Kolmogorov (Kolmogorov 1941, 1991) and the Iroshnikov-Kraichnan (IK, Iroshnikov 1963, 1964; Kraichnan 1965) models. At the limit of weak magnetic fields or strong turbulence ($\tau_3 \approx \tau_{NL}$) spectral evolution follows the Kolmogorov phenomenology ($P \propto f^{-5/3}$). For weak turbulence or strong magnetic fields ($\tau_3 \approx \tau_A$) the power spectrum is found to follow the IK phenomenology ($P \propto f^{-3/2}$). Bridging between Kolmogorov and IK phenomenologies has been suggested by, for example, Zhou & Matthaeus (1990) (with $\tau_3^{-1} = \tau_{NL}^{-1} + \tau_A^{-1}$) and Miller & Roberts (1995).

A flux function is used to describe the flux of wave power across frequencies. As a phenomenological treatment, the flux function is often assessed through dimensional analysis (see, e.g., Leith 1967, Dobrowolny et al. 1980, Tu et al. 1984, and Zhou & Matthaeus 1990). For numerical work, cascading can be described through the simplification of linear diffusion, defined as

$$F(r, f) = -D_{ff}\frac{\partial P}{\partial f}, \tag{3.39}$$

where D_{ff} is the spectral diffusion coefficient. This coefficient is phenomenological, with the form chosen to result in the preferred spectral shape (Kolmogorov or IK), possibly depending on plasma parameters. Laitinen (2003) formulated this as

$$D_{ff} = 2\pi C(r)\frac{v_A}{u_{sw} + v_A}\frac{1}{1 + \sqrt{fP/B^2}}\frac{f^4 P}{B^2}, \tag{3.40}$$

where $C(r)$ is a constant determining the wavenumber of the high-frequency turbulence break point. A simpler approximation, used in this work, is

$$D_{ff} = \frac{u_{\text{sw}} + v_{\text{A}}}{1 \text{ AU}} f_{\text{b}}^{-2/3} f^{8/3}, \qquad (3.41)$$

which leads to a Kolmogorov spectrum above the turbulence break point $f_b = 1$ mHz at 1 AU (see, e.g., Horbury et al. 1996).

3.6   Wave transport

In addition to cascading (section 3.5), wave power changes due to plasma expansion and changes of speeds, as the solar wind plasma flows outwards from the Sun (Matthaeus et al. 1994). The WKB approach (Parker 1965a; Barnes & Hollweg 1974), addresses transport of non-interacting waves, which can be seen as a starting point for modern wave transport theories. WKB alone has succeeded in correlating some interplanetary observations with coronal sources (see, e.g., Denskat & Neubauer 1982 and the Helios mission).

Tu et al. (1984) formulated the evolution of an outward-propagating spectrum of Alfvénic turbulence as

$$\nabla \cdot \left[\left(\frac{3}{2}\mathbf{u}_{\text{sw}} + \mathbf{v}_{\text{A}} \right) \frac{P(r,f)}{4\pi} \right] - \mathbf{u}_{\text{sw}} \cdot \nabla \left(\frac{P(r,f)}{8\pi} \right) = -\frac{\partial}{\partial f}\left(\frac{F(r,f)}{4\pi} \right).$$
$$(3.42)$$

The energy contained in inward-propagating waves was considered negligible despite them contributing to the spectral flux function $F(r,f)$. Applying (3.42) to a radial magnetic flux tube of cross-section $\mathcal{A} \propto B^{-1}$ results in the equation

$$\frac{1}{\mathcal{A}}\frac{\partial}{\partial r}\left[\mathcal{A}\left(\frac{3}{2}u_{\text{sw}} + v_{\text{A}} \right) \frac{P(r,f)}{4\pi} \right] - u_{\text{sw}}\frac{\partial}{\partial r}\frac{P(r,f)}{8\pi} = -\frac{\partial}{\partial f}\left(\frac{F(r,f)}{4\pi} \right).$$
$$(3.43)$$

In Tu et al. (1984), wave power was represented with a WKB-form, which, in the absence of cascading, would remain radially constant. In a

similar manner, we define

$$\tilde{P}(f,r) = \frac{V^2(r)}{B(r)v_{\mathrm{A}}(r)}P(f,r), \qquad (3.44)$$

which remains constant through WKB transport. Rewriting our wave evolution equation (3.43) with $\mathcal{A} \propto B^{-1}$, and including the wave growth rate term $\Gamma_{\mathrm{w}}(f,r)$, we find

$$\frac{\partial P(f,r)}{\partial t} + \frac{B(r)v_{\mathrm{A}}(r)}{V(r)}\frac{\partial}{\partial r}\left(\frac{V^2(r)}{B(r)v_{\mathrm{A}}(r)}P(f,r)\right) = \Gamma_{\mathrm{w}}(f,r)P(f,r) - \frac{\partial F}{\partial f}, \tag{3.45}$$

where F is the flux function. Rewriting this for $\tilde{P}$ and using a diffusive approximation for the flux function results in the wave evolution equation

$$\frac{\partial \tilde{P}(f,r)}{\partial t} + V(r)\frac{\partial \tilde{P}(f,r)}{\partial r} = \Gamma_{\mathrm{w}}(f,r)\tilde{P}(f,r) + \frac{\partial}{\partial f}D_{ff}\frac{\partial \tilde{P}(f,r)}{\partial f}. \tag{3.46}$$

3.6.1 Transmission of Alfvén waves across the shock

The presented methods for wave spectral evolution and wave propagation assume a quasi-steady background. Thus, these methods cannot be applied in solving the wave composition in the downstream of a shock. Detailed research into wave transmission at a shock front can be found in, for example, Campeanu & Schlickeiser (1992), Schlickeiser et al. (1993), and Vainio & Schlickeiser (1999). Ng (2007) simulated wave transmission along with particle interactions at a parallel shock, but only within a limited spatial range. For the research presented in this work, we consider the fact that downstream of the shock, turbulence is excited to a significant degree (Vainio & Schlickeiser 1998), and assume scattering to be strong (Giacalone & Jokipii 2007; Burlaga et al. 2006). Thus, for each acceleration cycle, the time spent in the downstream is much smaller than the time spent in the upstream, and can be approximated to be of small consequence.

Chapter 4

Diffusive Shock Acceleration

Diffusive shock acceleration (DSA) describes the process of acceleration as particles bounce repeatedly between the upstream and downstream of a shock. In the solar context, it is often described as accelerating seed particles from the solar wind to very high energies through repeated interactions with a propagating coronal shock or the bow shock of the Earth (see, e.g., Lee 1982). This is a first-order Fermi acceleration process (Fermi 1949), and has been investigated first by Axford et al. (1977), Krymskii (1977), Blandford & Ostriker (1978), and Bell (1978). In order for particles to encounter the shock multiple times, some phenomenon must force them to return from the upstream (and downstream) back to the shock. In this work, we study the possibility that turbulence generated by the accelerated particles themselves traps them to the upstream near-shock region.

4.1   Momentum increase

First-order Fermi acceleration, where a particle bounces off a propagating shock or the fast-moving plasma behind it (Bell 1977), could be crudely approximated as a ball bouncing off a table tennis racket. However, what in fact happens is best described through the scatterings the particle experiences in the various frames in question. In this discussion, we ignore the effects of solar rotation and assume solar wind plasma motion to be radial, omitting the effects caused by centrifugal and Coriolis forces.

The velocity of a particle can be defined, for example, in the following:

- The frame of a space-borne observational platform or satellite

- The frame of the propagating coronal shock

- The solar wind flow frame

- The frame of outward propagating waves

- The frame of downstream scatterings centres

As particles travel through interplanetary space, they scatter off Alfvénic turbulence at resonant wavenumbers. Particle pitch-angles change, but energy is conserved in the frame of scattering centres. As presented in chapter 3, assuming the simplified case of only outward propagating waves, the frame of scattering centres travels at the wave phase speed $V = u_{\mathrm{sw}} + v_{\mathrm{A}}$. Waves propagating across the shock are amplified and interactions alter cross helicities (Vainio & Schlickeiser 1999). Exact solutions to wave transmission processes are difficult to find, especially at oblique shocks, and thus, for simplicity, we assume the downstream scattering frame to be equal to the downstream plasma frame ($H_{c,2} = 0$).

The statistical average change of momentum $\langle \Delta p \rangle$, measured for particles in the solar wind frame after returning from a shock crossing, is positive due to the relative velocities of the upstream and downstream scattering centres (Bell 1978). Sample particle velocity schematics are shown in figure 4.1.

4.2   Population trapping

A requirement for extended Fermi acceleration is for particles to be trapped to the vicinity of the shock in both the upstream and the downstream. This can be achieved by, for example, scattering. The extent of the trapping region affects particle escape out of the acceleration process (see, e.g., Ostrowski & Schlickeiser 1996 and Vainio et al. 2000). In the upstream, particle trapping can be explained through scattering off Alfvén waves amplified by streaming particles (see section 3.4). Thus, for particles to be efficiently trapped to the near-shock region, there must be enough particle streaming to cause significant wave amplification.
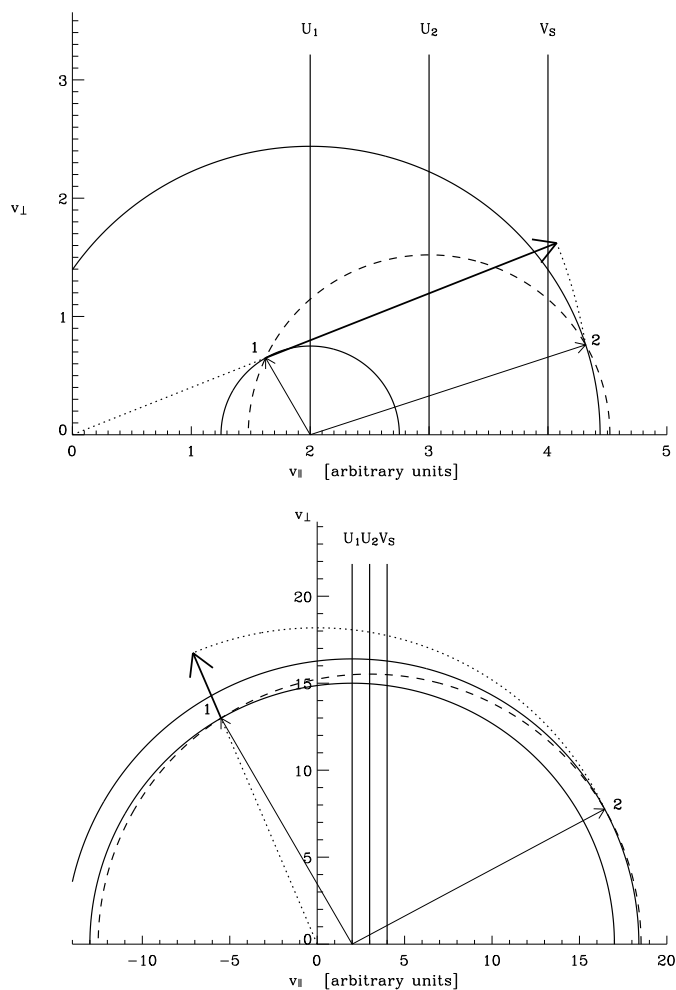
Figure 4.1: Fermi acceleration experienced by sample particles at a shock. Velocities are given in arbitrary units, in the inertial frame, and the flow velocity ratio $u_1/u_2 = 2$. The upper [lower] image depicts a slow [fast] upstream particle (arrow 1) experiencing scattering in the downstream (dashed lines) and being ejected to the upstream of the shock (arrow 2). The increase in inertial frame speeds is shown as the thick arrows, and the increase in upstream plasma frame speeds is seen from the difference in the radius of the solid semicircles.

4.2.1   Return from the downstream

Particles transmitted to the downstream of the shock are, as a population, convected away from the shock front. Further major energy gains are experienced only by particles which re-enter the upstream, remaining within the acceleration process. Statistical re-entry probabilities for particle populations can be assessed through the assumption of population isotropy (the approximation of strong scattering) and calculated particle fluxes. A useful simplification is to assume particles are trapped to a single flux tube and to calculate velocities in the HT frame.

For isotropic downstream populations, the probability of return to the shock front can be approximated by the ratio of shock-bound and downstream-bound fluxes. This was presented in Jones & Ellison (1991), and we formulate it as

$$P_{\mathrm{ret}} = \begin{cases} \left(\frac{v' - u_2}{v' + u_2} \right)^2, & v' > u_2 \\ 0, & v' \leq u_2. \end{cases} \tag{4.1}$$

As our description of guiding centre motion is restricted to a single dimension, with values calculated in the HT frame, equation 4.1 contains u_2, not $u_{2,\mathrm{n}}$. The particle plasma frame speed v' is considered in a frame moving along the downstream field line, not perpendicular to the shock front.

As particles transmitted to the downstream are anisotropic, the return condition (4.1) should be applied at a downstream return boundary (see, e.g., Ellison et al. 1995), where particles have achieved isotropy. Particles are allowed to propagate in the downstream and isotropise through small-angle scatterings. The downstream return boundary could be approximated as being, for instance, at a distance of 2λ in the downstream. We note that in the diffusion-convection equation,

$$u_x \frac{\partial n}{\partial x} = \frac{\partial}{\partial x} \left(\kappa_x \frac{\partial n}{\partial x} \right), \tag{4.2}$$

the characteristic distance of the system is the diffusion length κ_x / u_x, where x is the spatial distance in the shock-normal direction and κ_x is the associated diffusion coefficient. We then assume that particles have achieved sufficient isotropy at three times the diffusion length, placing the downstream return boundary at $\mathcal{B} = 3\kappa_x / u_x$.

The shock-normal diffusion coefficient $\kappa_x = \langle (\Delta x)^2 \rangle / (2\Delta t)$ can be split into field-parallel and field-perpendicular components as

$$\begin{aligned}
\langle (\Delta x)^2 \rangle &= \langle (\Delta x_\parallel)^2 \cos^2 \theta_{Bn,2} + (\Delta x_\perp)^2 \rangle \sin^2 \theta_{Bn,2} \\
&\quad + 2\Delta x_\parallel \Delta x_\perp \cos \theta_{Bn,2} \sin \theta_{Bn,2} \rangle \\
&= \langle (\Delta x_\parallel)^2 \cos^2 \theta_{Bn,2} + (\Delta x_\perp)^2 \rangle \sin^2 \theta_{Bn,2} \rangle,
\end{aligned} \tag{4.3}$$

where the mixed term vanishes due to ensemble averaging. Thus, we find $\kappa_x = \kappa_\parallel \cos^2 \theta_{Bn,2} + \kappa_\perp \sin^2 \theta_{Bn,2}$. If we assume only motion and diffusion parallel to the mean magnetic field, we have $\kappa_\perp = 0$. Using $\kappa_\parallel = v'\lambda_\parallel / 3$, this allows defining the return boundary as being parallel to the shock and at the distance $\mathcal{B} = \lambda_\parallel \cos \theta_{Bn,2} v'/u_2$ in the downstream.

4.2.2 Cross-field diffusion

Downstream of the shock, magnetic disturbances are strong, leading to efficient scattering. As $\delta B \ll B_0$ does not necessarily hold true, magnetic field lines can wander and twist. This can be described through field-line random walk, but this method introduces the possibility of a single field line intersecting with the shock front multiple times. Cross-field diffusion plays a minor role at quasi-parallel shocks when $\theta_{Bn,2}$ is small, and proper assessment of it would require full-orbit simulations, which are outside the scope of this thesis.

Even if particle motion is constrained to unidirectional field lines, particles experiencing strong scattering can be deflected to a new gyropath. In this way, they are no longer locked to a single magnetic field line (see, e.g., Jones et al. 1993 and Baring et al. 1995). This can lead to their guiding centre jumping up to a theoretical maximum distance of $2r_L$, perpendicular to the magnetic field line. This can be modelled as cross-field diffusion, with perpendicular diffusive motion of the guiding centre.

In **Paper III**, we assess effects of downstream cross-field diffusion on injection according to this approximation of jumps across unidirectional field lines. We consider two downstream cross-field diffusion coefficients. The first goes to zero in the vicinity of the shock, prohibiting particles from reaching the shock front via a cross-field diffusion jump. The second remains constant up to the shock, allowing particles to jump right up to the shock front, from where particles with a suitable shock-bound parallel velocity can be injected. The first method results in injection decrease,

the second in injection increase of similar magnitude. Thus, we consider ignoring cross-field diffusion a fair first-order approximation for the scope of this thesis.

4.2.3 The injection problem

A longstanding question regarding DSA is that of sufficient seed particle injection. Solar wind seed particles interacting with a propagating shock must be injected into the acceleration process in quantities significant enough to maintain acceleration and to match observations. The diffusion approximation, often used for describing evolution of particle populations, assumes that they are quasi-isotropic, which holds true especially when $v \gg u$. Especially at low energies, the diffusion approximation is incapable of describing particle population evolution accurately, as particles are not isotropic in the shock frame. Seed particles with high energies, which can be accurately modelled through diffusive equations, may not be not abundant enough to result in adequate particle injection for an efficient DSA process.

As shock-normal propagation velocity V_s or shock-normal angle θ_{Bn} increases, the HT-frame flow speeds increase, and the threshold speeds at which diffusive methods are no longer applicable increase. Thus, the injection problem is especially meaningful for oblique shocks, which are often viewed as essential for SEP acceleration (see, e.g., Ellison et al. 1995 and Giacalone & Jokipii 2006). The injection problem is assessed in detail in **Paper III**.

The injection problem can be addressed in a variety of ways. Some choose to bypass it by assuming mono-energetic injection (e.g. Li et al. 2012) or power-law seed populations (e.g., Sandroos & Vainio 2007; Ng & Reames 2008). Other methods include a κ-distribution with an ad-hoc minimum injection energy (e.g. Neergaard Parker & Zank 2012). Alternatively, particle injection energies can be modelled on the downstream gas temperature (Zank et al. 2007) or using a thermostat model (Malkov & Völk 1995a,b, 1998).

In Monte Carlo simulations, the anisotropic downstream-transmitted seed population can be assumed to isotropise through small-angle scatterings. However, downstream propagation without boundaries is not numerically feasible, requiring a combination of particle simulations and careful application of the diffusion approximation. One such method, used in this work, is described in section 5.

4.2.4   Upstream trapping

In the less-turbulent upstream, particle population escape can be assessed through transport equations and the quantified amplified turbulence. Strong turbulence leads to a small value of the diffusion coefficient $D_{\parallel}$, and this strong turbulence is highly dependent on a large amount of energetic particle streaming in the upstream (see section 3.4). As presented in section 3.2.2, equation (3.16) for an isotropic population of particles using linear particle density is

$$\frac{\partial n}{\partial t} + \frac{\partial}{\partial r}\left[\left(V + \frac{D_{\parallel}}{L}\right)n\right] - \frac{\partial}{\partial p}\left[\frac{p}{3}\left(\frac{\partial V}{\partial r} + \frac{V}{L}\right)\,n\right] = \frac{\partial}{\partial r}\left(D_{\parallel}\frac{\partial n}{\partial r}\right).$$

The second term, which is the convection term, shows that the particle population is convected away from the Sun at speed $V + D_{\parallel}/L$, where the portion $D_{\parallel}/L$ is due to diffusion and magnetic focusing. Thus, in regions where $V + D_{\parallel}/L < V_{\rm s}$, the particle population experiences sufficient scattering to cause particles to re-encounter the shock and be accelerated to higher energies. Conversely, in regions where $V + D_{\parallel}/L > V_{\rm s}$, the scattering effects of turbulence are insufficient to convect the population of accelerated particles back to the shock front, allowing them to escape.

The $V + D_{\parallel}/L < V_{\rm s}$ formulation of particle trapping is supported by the concept of streaming limits. This effect, based on observations, was introduced in Reames (1990a) and further assessed in, for example, Ng & Reames (1994) and Reames & Ng (1998). In Reames & Ng (2010), it is linked to GLE observations.

In figure 4.2 we show a sample particle population in front of a coronal shock, where the streaming particles have amplified turbulence to an adequate extent to generate a region of turbulent trapping in front of the shock. Particles outside the trapping region (at high energies or far from the shock) are slow to isotropise whilst experiencing strong focusing towards $\mu = 1$, and thus, their mean motion is away from the shock.

4.3   Accelerated population spectra

Assuming that particle populations are isotropic allows finding analytical solutions to accelerated population spectra. The diffusion-convection equation (see, e.g, Parker 1965b, Gleeson & Axford 1967, and Jones 1990) can be
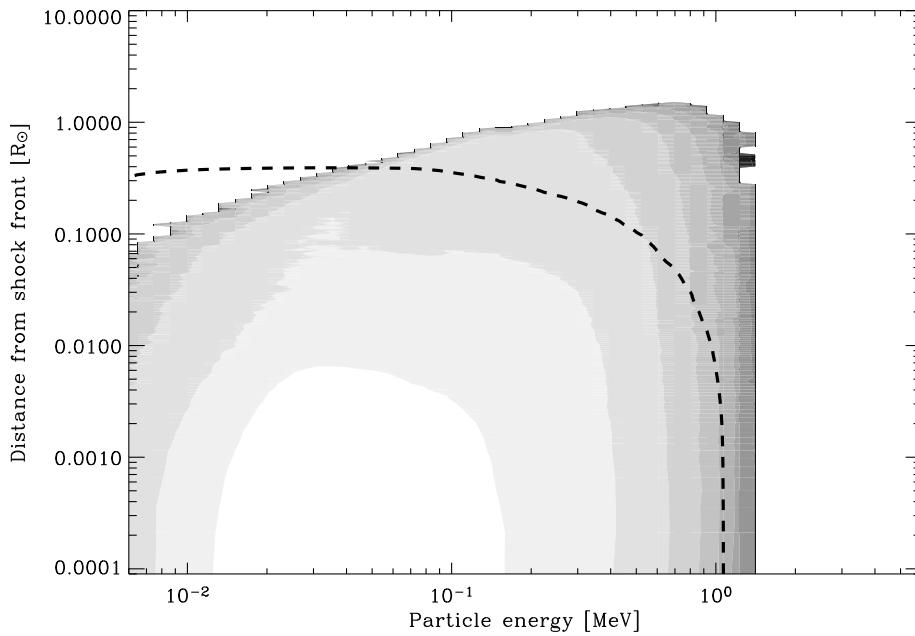
Figure 4.2: Sample energetic particle population accelerated by a coronal shock (filled contours), and the associated turbulent trapping region formed due to wave amplification through streaming of particles (dashed curve). The edge of the turbulent trapping region is defined as $V + D_{\parallel}/L = V_{\mathrm{s}}$.

used to find theoretical steady-state solutions for particle spectra at a propagating shock (see, e.g., Axford et al. 1977, Krymskii 1977, and Blandford & Ostriker 1978).

We present various well-known solutions, where the particle distribution function must be continuous at the shock. The upstream distribution may, as $x \to -\infty$ (in the far upstream), approach alternatively 0 or a small background spectrum. The downstream spectrum is taken to be spatially constant. For detailed analysis on previous work related to spectral analysis of accelerated particles, we refer the reader to, for example, Jones (1990), Schlickeiser et al. (1993), and Vainio (1999).

One solution for cosmic rays of momentum $p \gg mu_{1x}$, where there is no additional source function at the shock, is given by utilising separate asymptotic values for $x \to \pm\infty$ (Blandford & Ostriker 1978) as

$$f_0(x,p) = \begin{cases} f_-(p) + \{f_+(p) - f_-(p)\}\, e^{-u_{1x}\int_x^0 dx' D_{xx}^{-1}}, & x < 0 \\ f_+(p), & x \geq 0 \end{cases} \qquad (4.4)$$

$$f_+(p) = \sigma p^{-\sigma} \int_{p_0}^p dp'\, p'^{\sigma-1} f_-(p'), \qquad (4.5)$$

where $\sigma = 3r_{\mathrm{g}}/(r_{\mathrm{g}}-1)$ (Drury 1983). Further, solving the energy spectrum of the differential particle flux in the downstream of the shock (see, e.g., Vainio 1999) finds

$$\frac{dJ}{dE} = p^2 f_0 \propto p^{-\Gamma}, \qquad (4.6)$$

where $\Gamma = \sigma - 2 = (r_{\mathrm{g}} + 2)/(r_{\mathrm{g}} - 1)$.

Choosing to include a low-energy mono-energetic particle source function Q_0 at the shock front, Forman & Webb (1985) find the solution as

$$f_+(p) = \sigma \left\{ \frac{Q_0}{4\pi u_{1x} p_0^3} + \int_{p_0}^p \frac{dp'}{p'} \left(\frac{p'}{p_0}\right)^\sigma f_-(p') \right\} \left(\frac{p_0}{p}\right)^\sigma, \qquad (4.7)$$

where $p_0 = mu_{1x}$. This leads to the conclusion that for all upstream seed particle distributions where $f_-(p) \propto p^{-\sigma'}$ and $\sigma' > \sigma$, the resultant spectrum at the shock still reduces to $f_+(p) \propto p^{-\sigma}$.

The above derivations assume that particle populations isotropise in the frame of gas flows. If particles are assumed to isotropise in the frame of scattering centres (propagating at the wave phase speed in the frame of gas

flows), we find $\sigma = 3r_{sc}/(r_{sc} - 1)$, where

$$r_{sc} = \frac{V_{1x}(p)}{V_{2x}(p)} = r_g \frac{M_A + H_{c1}}{M_A + \sqrt{r_g}H_{c2}} \tag{4.8}$$

is the scattering centre compression ratio for particles of momentum p (Vainio & Schlickeiser 1998).

When comparing simulation results or analytical theories to particle observations (see, e.g., Tylka et al. 2000), it is necessary to account for high-energy particles escaping from the acceleration process due to the energy dependence of the diffusion coefficient D_{xx}. Ellison & Ramaty (1985) introduced the e-folding spectrum as a way to parametrise the maximum energy attained through shock acceleration as

$$\frac{dJ}{dE} \propto p^{-\Gamma} \exp\left(-\frac{E}{E_c}\right), \tag{4.9}$$

where E_c is the spectral cut-off energy. E_c will change with shock properties, acceleration efficiency, and ion population.

4.4 Acceleration timescales

In section 4.3, a solution was provided for particle spectra resulting from a steady-state DSA scenario. This is a useful analytic tool, applicable to, for example, the termination shock at the outer edge of the heliosphere. However, a shock propagating through the solar corona is a transient event, and thus, it becomes necessary to investigate acceleration timescales (Krymsky et al. 1979). The canonical solution for acceleration time in DSA is presented as (Axford 1981)

$$\tau_{acc} = \left(\frac{1}{p}\frac{dp}{dt}\right)^{-1} = \frac{3}{u_1 - u_2}\left(\frac{D_{\parallel,1}}{u_1} + \frac{D_{\parallel,2}}{u_2}\right). \tag{4.10}$$

Assuming downstream turbulence to be strong, and thus, downstream scattering times to be negligible, equates to setting $D_{\parallel,2} \approx 0$. Analytical solutions to acceleration timescales, with momentum-dependent diffusion coefficients, are presented in, for example, Drury (1983) and Forman & Drury (1983).

4.5 Shock drift acceleration

Shock drift acceleration (SDA) is an acceleration mechanism of energetic particles which only occurs when $\theta_{Bn} > 0$. It is an effect occurring on (relatively) small spatial scales due to the motional electric fields arising from the component of plasma flow perpendicular to the magnetic field. SDA can cause rapid SEP acceleration and has been linked to energetic storm particle spikes (Sarris & van Allen 1974; Armstrong et al. 1977). If calculations are done in the HT frame, the motional electric field vanishes, and SDA effects can be considered accurately modelled to first order (see, e.g., Webb et al. 1983 and Terasawa 1979).

4.5.1 Shock surfing

A similar process to shock drift acceleration, increasing pick-up ion energies, is shock surfing (see, e.g., Lever et al. 2001). In shock surfing, the cross-shock potential causes the particle to be reflected at the shock in mid-gyropath. Thus, the particle bounces along the shock front in a series of arcs, being accelerated by the motional electric field, until it has achieved enough energy to escape the surfing process. Shock surfing can be examined through full-orbit simulations, but is outside the scope of this thesis.

Part II

CSA: Monte Carlo simulations of Coronal Shock Acceleration

Chapter 5

Developing a self-consistent DSA simulation

Numerical simulations of SEP acceleration are used to infer accelerated particle spectra and time profiles from, including but not limited to, seed particle populations and shock properties. Due to the limitations of performing in-situ observations within the solar corona, simulations play a major role in aiding our understanding of SEP acceleration. As such, they have been the focus of many research groups for decades.

A review on this field of study can be found in, for example, Lee (2005). Ng et al. (2012) present a review on one modelling effort, which has given interesting results on, for example, streaming limits and elemental abundances. It includes the bootstrapped feedback of self-generated waves (Ng & Reames 2008), finding solutions to analytical schemes via numerical methods (see also Ng et al. 1999 and Ng et al. 2003). Another model using distribution functions is the α-particle acceleration model of Galinsky & Shevchenko (2010), utilising scale separations. Its strengths include injection from the ambient medium and support for large spatial scales.

Giacalone (2005) presented test particle simulations, assessing the effect of shock-normal angle on acceleration efficiency (see also Giacalone & Jokipii 2006). They, however, included no wave amplification due to particles, instead assessing a multitude of astrophysical scenarios not limited to coronal effects. The SHOPAR code (see, e.g., Sandroos & Vainio 2006 and Sandroos & Vainio 2009a) is likewise a test particle code, but developed specifically for the coronal environment and associated complex magnetic geometries. The PATH code (see, e.g., Zank et al. 2000) consists of a 2D MHD module for shock modelling and an onion shell model for accelerated

particle populations downstream of the shock with Monte Carlo simulation of ions escaping upstream.

The Coronal Shock Acceleration (CSA) simulation software was developed in order to meet the requirements of extended self-consistent DSA at a propagating coronal shock, with wave amplification generated by the streaming particles themselves. The analytical basis of the model, along with wave amplification equations, was presented in Vainio (2003). Previous results based on the CSA code base have been published in Vainio & Laitinen (2007) and Vainio & Laitinen (2008). The software supports the OpenMPI library for sharing processing load over multiple cores. The software is written in Fortran 90/95, with data files using the FITS file format.

5.1 Simulation framework

CSA is a Monte Carlo simulation code which simulates coupled transport of energetic particles and Alfvén waves. Due to numerical limitations, the coronal/interplanetary flux tube, along which the coronal shock and particles propagate, is modelled with only a single radial coordinate. Simulation parameters define solar wind parameters, normalisation values at 1 AU, injected particle population properties, and the motion of the shock front along the flux tube.

As DSA with self-generated waves cannot be described through test particle simulations, the software is constructed with a feedback loop. Seed population parameters and the shock description are predetermined through initialisation parameters and the applied solar wind model. We consider downstream turbulence to be strong regardless of upstream wave spectra. This way, particle injection can be assessed during simulation initialisation. Then, as the shock propagates through the corona, injected particles are activated as the shock passes their injection position.

Particle propagation is implemented through a 1-D guiding centre approach. Particle streaming is tracked and used to infer wave amplification. Alfvénic turbulence is tracked on a grid attached to the propagating shock, with frequency diffusion (see equation 3.41) and convection (see section 3.6) used to account for non-linear interactions and WKB transport. Alfvén wave power is then used to calculate particle scattering coefficients. At predetermined times, particle spectra and wave power are written to disk,
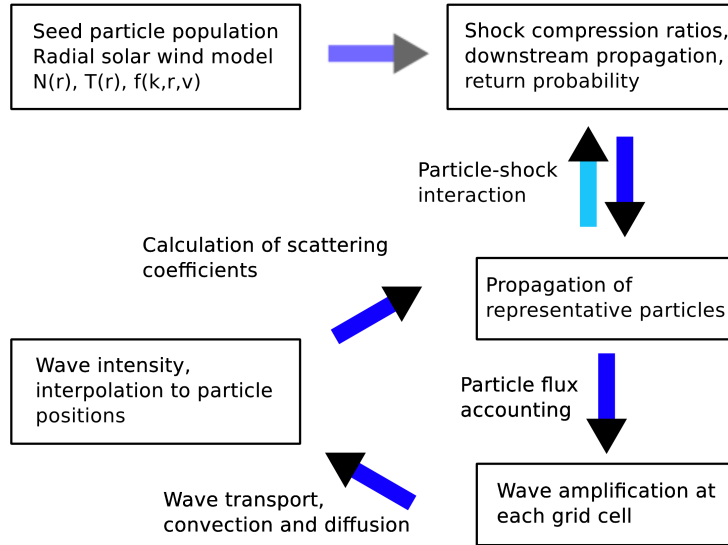
Figure 5.1: Flow chart of CSA simulation software. Particle properties affect their return probability and downstream propagation, but do not modify shock properties.

with the simulation continuing until the target simulation time is attained. A flowchart describing the simulation framework is presented in figure 5.1.

CSA supports the OpenMPI standard for parallelisation with the amount of simulated particles split across all processes. At time step intervals Δt, processes distribute accumulated turbulence amplification coefficients $\Gamma_\mathrm{w}(r, f)$ amongst themselves. Δt can be adjusted during the simulation in order to minimise data transfer between processes. Minimum and maximum values for allowed amplification coefficients can be set manually, limiting Δt.

CSA can save its full simulation state at wall time or simulation time intervals, allowing computationally intensive simulations to be run in multiple consecutive sessions. This resume functionality supports parallelisation, with the primary root process handling all file access.

The logarithmic grids CSA uses internally are also used for data output to disk. Simulation parameters include the number of bins in each direction

(radial, frequency, velocity) and the minimum and maximum values for each direction. The values assigned to the grid in the χ-direction (where $\chi = v, f,$ or r and $i = 0 \ldots n_\chi - 1$) are

$$\chi_i = \exp\left(\frac{i}{n_\chi - 1} \log\left(\frac{\chi_1}{\chi_0}\right) + \log\left(\chi_0\right)\right). \tag{5.1}$$

5.2   Particle Transport

We solve the stochastic differential equations governing particle transport by considering a large number of representative particles which are propagated inside the flux tube and scattered off Alfvén waves. Instead of solving the equation for focused transport (3.12), we split the equivalent stochastic particle motion into separate operations. It should be noted that adiabatic deceleration is implicitly included when particle focusing and scattering are accounted for in appropriate frames of reference.

Particle motion is restricted to the adiabatic guiding centre approximation (in the HT frame), where guiding centre motion and plasma flow are aligned with the background magnetic field $\mathbf{B}_0$. Particles are propagated with a staggered leapfrog algorithm (see, e.g., Morton & Mayers 2005), with particle time step $\Delta t_i \leq \Delta t$.

The particle time step is set for each particle as $\Delta t_i = 2^{-n_i} \Delta t$, where $n_i \geq 0$ is an integer. This is used to constrain the scattering amplitude $\nu_i \Delta t_i$ to values between 0.02 and 0.05. Additionally, n_i may be incremented to prevent a particle crossing more than one spatial grid cell boundary during one step.

At each particle half-step, particle pitch-angles are corrected for focusing effects due to decreasing magnetic flux density, and particles are scattered through isotropic small-angle scattering in the frame of outward propagating Alfvén waves. At the half-step interval, the particle position is compared with the shock position, and shock interaction routines are called when necessary.

The equations describing implicit Euler solutions for focusing are (Vainio & Laitinen 2008)

$$h = -\frac{v_i \Delta t_i}{2} \left.\frac{\partial \ln B}{\partial r}\right|_{r=r_i} \tag{5.2}$$

and

$$\mu_i' = \frac{-1 + \sqrt{1 + 4h(\mu_i + h)}}{2h},$$ (5.3)

where r_i is the particle position at the half-time step, and v_i and μ_i are the particle speed and pitch-angle cosine at the beginning of the time step. Isotropic particle scattering, at frequency ν, is then performed after Lorentz-transforming v_i and μ_i to the Alfvén wave frame (designated v_i', μ_i'). Scattering angles $\theta_{\rm s}$ and $\phi_{\rm s}$ are randomized according to Kocharov et al. (1998), where $\theta_{\rm s} = \sqrt{-2\nu\Delta t_i \log(1 - \mathcal{S})}$ and $\phi_{\rm s} = 2\pi\mathcal{S}'$, and $\mathcal{S}$ and $\mathcal{S}'$ are uniformly distributed random numbers in the range $[0, 1)$. The pitch-angle cosine, after focusing and scattering, is

$$\mu'' = \mu' \cos\theta_{\rm s} + \sqrt{1 - \mu'^2} \sin\theta_{\rm s} \cos\phi_{\rm s}.$$ (5.4)

5.3   Wave evolution

The wave power of Alfvénic fluctuations is stored on a grid, attached to the propagating shock and convected along with it. The grid is logarithmic both in the radial and frequency directions. Only outward-propagating waves are considered (see, e.g., Schwenn & Marsch 1991, pp. 159), moving at speed $V = u_{\rm sw} + v_{\rm A}$. Our wave model considers WKB propagation with added terms for diffusion and amplification, and additionally wave power is convected on the grid towards the shock at speed $V_{\rm s} - V$. We store wave power as WKB-normalised values according to (3.44).

This evolution of the wave spectrum, formulated as equation (3.46), is handled through operator splitting. After each simulation time step, we first apply frequency diffusion and then convect wave power on the grid according to the difference between shock propagation speed and wave phase speed. Finally, wave amplification due to particle streaming is applied with the methods described in section 3.4.

Our diffusion calculations are conducted with a standard implicit Crank-Nicholson scheme (Crank et al. 1947), using the form of D_{ff} presented in (3.41). The Crank-Nicolson scheme is unconditionally stable and always second-order accurate. However, we constrain the diffusion time step as $\Delta t_j \leq (\Delta f_{\rm min})^2 / D_{ff,\rm max}$ to preserve accuracy. The wave intensity at the low frequency boundary is kept constant, representing a heating source,

and the wave intensity at the high frequency boundary is set to follow a $\tilde{P} \sim f^{-3}$ power law.

Due to spatially changing wave phase speeds $V(r)$, wave advection is handled by a combination of a regular 1st order upwind scheme and an explicit Lax-Wendroff scheme (Lax & Wendroff 1960), with a Van Leer flux limiter (van Leer 1974) defining the combination ratio. Additionally, the scheme takes into account the logarithmic nature of the grid. The advection module can use smaller time steps $\Delta t_k = 2^{-n_k}\Delta t$ to retain stability according to the Courant condition. At the far boundary, $\tilde{P}$ is kept constant, and at the shock boundary, a regular upwind scheme is used.

The initialisation spectrum of waves is set to $\tilde{P}(f, r_{\text{w0}}) \propto f^{-1}$ where r_{w0} is an initialisation distance parameter, which we set as $r_{\text{w0}} = 1.5 \, R_{\odot}$. We then calculate diffusive advection of this spectrum, first to the initial position of the shock, and then across the whole wave grid. Finally, we normalise the wave power in order to achieve a given 100 keV proton mean free path at 1 AU. We set this to $\lambda(1\text{AU}) = 55 \, R_{\odot}$, which agrees with observations (see, e.g., Palmer 1982).

The process of transforming particle streaming into wave amplification is described in section 3.4. We present equation (3.38) as

$$\Gamma(r, f_{\text{r}}) = \frac{\pi}{2} \Omega_{\text{c}} \frac{m}{m_{\text{p}}} \frac{p S_{\alpha}(r, p, t)}{n_{\text{p}} v_{\text{A}}}, \tag{5.5}$$

where the particle streaming is given as

$$S_{\alpha}(r, p, t) = 2\pi \int_{-1}^{+1} v p^2 f_{\alpha}(r, p, t) d\mu. \tag{5.6}$$

After each half-step of particle movement, the position of the particle on our wave grid is compared to saved values, to accumulate particle streaming. However, as our grid is attached to the shock, this results in the shock-frame streaming value $S_{\alpha,\text{grid}}(\mathbf{r}, p, t)$. This is transformed into the frame of propagating waves as $S_{\alpha}(\mathbf{r}, p, t) = m_{\text{s}} S_{\alpha,\text{shock}}(\mathbf{r}, p, t)$, where

$$m_{\text{s}} = \frac{v_{\text{w}} \mu_{\text{w}}}{v_{\text{g}} \mu_{\text{g}}} \tag{5.7}$$

is a transformation parameter, a subscript of w denotes particle values in the frame of waves and one of g denotes values in the frame of the grid.

Particle streaming is gathered over time step Δt intervals, then processed into wave amplification as described in section 3.4.

5.4   Simulation and shock parameters

Our solar wind model considers a single radial flux tube of coronal or solar wind plasma. The properties of plasma are fixed with semi-empirical expressions as a function of radial distance from the Sun. The flux tube is assumed to be surrounding a radial magnetic field line, and expands according to $\mathcal{A} \propto B^{-1}$, with

$$B(r) = B_0 \left(\frac{r}{r_\oplus} \right)^{-2} \left[1 + b_f \left(\frac{r}{R_\odot} \right)^{-6} \right], \tag{5.8}$$

where $r_\oplus = 1\,\mathrm{AU}$ and $R_\odot$ is the solar radius. We typically set $b_f = 1.9$ and B_0 scales the values to 2.90 nT at 1 AU (see Vainio et al. 2003). We consider the solar wind density to be (Cranmer & van Ballegooijen 2005)

$$n_{\mathrm{sw}}(r) = n_0 \left[\left(\frac{r}{R_\odot} \right)^{-2} + 25 \left(\frac{r}{R_\odot} \right)^{-4} + 300 \left(\frac{r}{R_\odot} \right)^{-8} \right.$$
$$\left. + 1500 \left(\frac{r}{R_\odot} \right)^{-16} + 5796 \left(\frac{r}{R_\odot} \right)^{-33.9} \right], \tag{5.9}$$

where n_0 is used to fix the Alfvén speed, from equation (2.4), to match the simulation parameter $v_A(1\,\mathrm{AU})$. We usually set $v_A(1\,\mathrm{AU}) = 20\,\mathrm{km\,s^{-1}}$. The ion temperature T is taken to be (Cranmer & van Ballegooijen 2005)

$$T(r) = 5 \cdot 10^5 \left[0.2 + 0.02 \left(\frac{r}{R_\odot} \right)^{0.8} + 0.21 \left(\frac{r}{R_\odot} \right)^{-33} \right]^{-1}. \tag{5.10}$$

Ions and electrons are considered to have the same temperature, and they both contribute to plasma pressure in calculating the sound speed in equation (2.2). Solar wind flow velocity is inferred from mass conservation. The temperatures and flow speeds used in our model are shown in figure 5.2.

The shock profile evolution parameters chosen for our model are the initial shock-normal velocity $V_{\mathrm{s},0}$, the initial shock angle cosine $\mu_{\mathrm{s},0} = \cos(\theta_{Bn,0})$, the asymptotic shock angle cosine $\mu_{\mathrm{s},1} = \cos(\theta_{Bn,\infty})$, the shock-normal de-
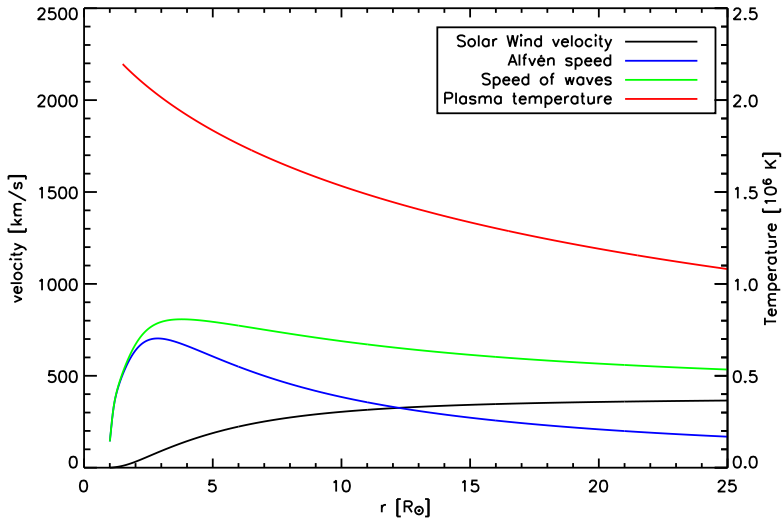
Figure 5.2: CSA model values for solar wind speed u_{sw}, Alfvén speed v_{A}, wave phase speed V, and ion temperature T. Model normalisation parameters are $B(1\,\mathrm{AU}) = 2.90\,\mathrm{nT}$, $b_f = 1.9$, $v_{\mathrm{A}}(1\,\mathrm{AU}) = 20\,\mathrm{km\,s^{-1}}$, and $u_{\mathrm{sw}}(1\,\mathrm{AU}) = 380\,\mathrm{km\,s^{-1}}$.

celeration $\dot{V}_{\mathrm{s}}$, and the inverse shock cosine transition time q_{n}. The shock-normal velocity at time t is

$$V_{\mathrm{s}}(t) = V_{\mathrm{s},0} + \dot{V}_{\mathrm{s}}t \qquad (5.11)$$

and the shock-normal angle cosine at time t is

$$\mu_{\mathrm{s}}(t) = \frac{\mu_{\mathrm{s},0} + tq_{\mathrm{n}}\mu_{\mathrm{s},1}}{1 + tq_{\mathrm{n}}}. \qquad (5.12)$$

This allows for modelling of an expanding shock front with a decreasing shock-normal velocity, and with the intersection angle decreasing over time, which is a fair approximation of many coronal mass ejection driven shocks. The point of intersection between the shock front and the magnetic field line within the simulation flux tube propagates at speed $V_{S,\parallel}(t) = V_{\mathrm{s}}(t)/\mu_{\mathrm{s}}(t)$ in the solar frame and is stationary in the HT frame.

The gas compression ratio r_{g} at the shock front is solved according to section 2.5, using a simple Newton iterator. The magnetic compression ratio r_B can be solved analytically with equation (2.24). Gas and magnetic compression ratios for sample shocks are presented in figure 5.3. CSA considers the shock profile to be a step with no prescribed foot, ramp or foreshock. We do not convect actual simulation values of Alfvénic turbulence to the downstream, and they are not used in calculating shock parameters or downstream scattering amplitudes.

5.5 Particle-shock interactions

Simulated particles which encounter the propagating coronal shock can be either reflected at the shock or transmitted to the downstream. For each particle-shock interaction, we calculate the appropriate return probability P_{ret}, and if it is high enough, we return the particle back to the upstream with the appropriate modifications to speed and pitch-angle. The representative weight of the particle is adjusted by multiplying it with the return probability P_{ret}.

Reflection at a shock front can be caused by magnetic compression (section 2.6) and the cross-shock potential (section 2.7). As presented in appendix B of **Paper III**, a particle is reflected, and thus, returned to the
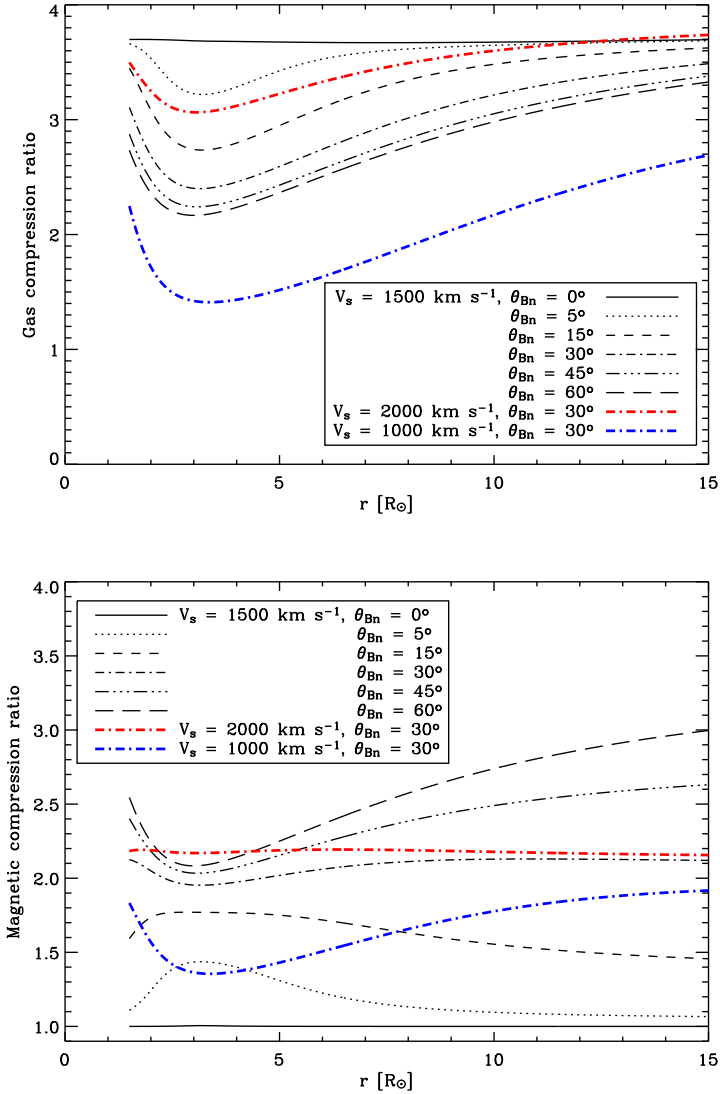
Figure 5.3: CSA model solutions for gas compression ratio r_g (above) and magnetic compression ratio r_B (below), for a selection of shock-normal velocities and angles.

upstream, if

$$2\mu v u_1 - v^2 + v^2(1 - \mu^2)r_B > u_1^2 - 2(q/m)\Delta\Phi. \tag{5.13}$$

In our notation, the return probability from a shock encounter for a reflected particle is $P_{\mathrm{ret}} = 1$.

Transmitted particles are slowed down by the cross-shock potential and have their pitch-angle altered due to magnetic compression. The downstream speed v' and pitch-angle μ' of particles can be solved, as presented in **Paper III**, with the following equations:

$$
\begin{aligned}
v'^2 &= \left[u_2 - \sqrt{u_1^2 - 2\mu v u_1 + v^2 - v^2(1 - \mu^2)r_B - 2(q/m)\Delta\Phi}\right]^2 \\
&\quad + (1 - \mu^2)v^2 r_B
\end{aligned} \tag{5.14}
$$

$$\mu' = \frac{1}{v'}\left[u_2 - \sqrt{(\mu v - u_1)^2 - \frac{2}{m}\mathcal{M}\Delta B - \frac{2}{m}q\Delta\Phi}\right] \tag{5.15}$$

$$\mathcal{M} \equiv \frac{m(1 - \mu_2^2)v_2^2}{2B_2} = \frac{m(1 - \mu_1^2)v_1^2}{2B_1} \tag{5.16}$$

CSA considers the downstream of a propagating coronal shock to be strongly turbulent ($D_{\parallel,2} \approx 0$, see eq. 4.10), resulting in negligible downstream residence time. In the downstream, we apply the ratio of shock-bound and downstream-bound fluxes (see equation 4.1) to find the mean probability of return to the upstream.

Freshly transmitted particles are not isotropic, and as presented in **Paper III**, making such an assumption could significantly skew injection probabilities. Thus, we propagate particles in the downstream up to a return boundary at $x_{\mathrm{n}} = -\mathcal{B}$ (see, e.g., Ellison et al. 1996 and section 4.2.1). Particles have an initial return probability of $P_{\mathrm{ret},0} = 1$. At the distance $x_{\mathrm{n}} = -\mathcal{B}$, particles have encountered enough scatterings to warrant the assumption of isotropy. At this point, the return probability $P_{\mathrm{ret},i}$ from equation (4.1) can be assigned. After this, particles receive a new randomised flux-weighted shock-bound pitch-angle

$$\mu' = \frac{1}{v'}\left(u_2 + (v' - u_2)\sqrt{\mathcal{S}}\right), \tag{5.17}$$

where $\mathcal{S}$ is a uniformly distributed random number in the range [0,1). Particles then propagate and scatter until they return to $x_\mathrm{n} = -\mathcal{B}$ or until they reach the shock front. Multiple encounters with the return boundary can result in a cumulative return probability $P_\mathrm{c} = \prod P_{\mathrm{ret},i}$. If at any time $P_\mathrm{c} < 10^{-6}$, the particle is considered lost to the downstream. If the particle returns to the shock front, it is returned to the upstream with $P_\mathrm{ret} = P_\mathrm{c}$.

In the downstream, the angle between the shock normal and the mean magnetic field is θ_{Bn2}, which is found from $\cos\theta_{Bn2} = r_B^{-1}\cos\theta_{Bn}$. The field-parallel diffusion coefficient is $\kappa_\parallel = v'\lambda_\parallel/3$, and if used, the field-perpendicular diffusion coefficient is $\kappa_\perp(\mu') = a_\perp\kappa_\parallel(1-\mu'^2)$, where $a_\perp$ is a parameter of cross-field diffusion strength. The term $(1-\mu'^2)$ scales motion according to the Larmor radius r_L. The shock-normal diffusion coefficient is then formulated as $\kappa_x = \kappa_\parallel\cos^2\theta_{Bn,2} + \kappa_\perp(\mu')\sin^2\theta_{Bn,2}$.

In **Paper II**, the downstream return boundary is set to $\mathcal{B} = 2\lambda_\parallel\cos\theta_{Bn2}$ in order to ensure sufficient isotropisation time. Elsewhere, we use $\mathcal{B} = 3\kappa_x/u_x$, which becomes

$$\mathcal{B} = \lambda_\parallel\left(\cos^2\theta_{Bn,2} + a_\perp\sin^2\theta_{Bn,2}\right)\frac{v'}{u_2\cos\theta_{Bn,2}}. \tag{5.18}$$

In this, we have cautiously used the maximum value $\kappa_\perp(\mu')|_\mathrm{max} = a_\perp\kappa_\parallel$. If cross-field diffusion is not simulated, we set $a_\perp = 0$.

Particle motion normal to the shock front is found as

$$\Delta x_\mathrm{n} = \Delta x_\parallel\cos\theta_{Bn,2} + \Delta x_\perp\sin\theta_{Bn,2}. \tag{5.19}$$

In the downstream, field-parallel particle motion is $\Delta x_\parallel = (v'\mu' - u_2)\Delta t'$, where $\Delta t' = 0.1/\nu$ is the propagation time step and $\nu = v'/\lambda_\parallel$ is the particle scattering frequency. The perpendicular motion of particles is solved using the stochastic differential equation method (Gardiner 1985) as

$$\Delta x_\perp = \mathcal{R}_\mathrm{n}\sqrt{2\kappa_\perp(\mu')\Delta t'} = \mathcal{R}_\mathrm{n}\sqrt{1-\mu'^2}\sqrt{(2/3)a_\perp\lambda_\parallel v'\,\Delta t'}, \tag{5.20}$$

where $\mathcal{R}_\mathrm{n}$ is a normal distributed random number from a Box-Muller transform (Box & Muller 1958). Perpendicular motion is additionally constrained to $\Delta x_\perp \leq v'_\perp\Delta t'$.

5.6   Particle injection

A major factor contributing to the efficiency of DSA is the total amount of particles participating in the acceleration process. CSA simulates particle injection by propagating a coronal shock along the prescribed radial flux tube and simulating interactions of ambient solar wind test particles with the shock front. Any particles which return to the upstream of the shock are considered injected, and can participate in the acceleration process. The injection process is discussed in extensive detail in **Paper III**.

CSA allows for two κ-distributed seed particle populations (hereafter populations 1 and 2), which follow the descriptions given in section 1.5. Additionally, each population can contain a portion of minor ions (^{3}He^{2+}, ^{4}He^{2+}, ^{16}O^{6+}, and ^{56}Fe^{14+}). The spatial distribution of seed particles for each population is given as

$$n_{\alpha j}(r) = \epsilon_{\alpha j} n_{\text{sw}}(r), \tag{5.21}$$

where values $\epsilon_{\alpha j}$ are parameters, α designates the ion in question, and j represents population 1 or 2. For protons, CSA allows values of $\epsilon_{\text{H1}} + \epsilon_{\text{H2}} \in (0, 1]$. Abundances $\epsilon_{\alpha j}$ for minor ions are given in units $\epsilon_{\text{H}j}$. Suggested sample values for ion abundances are $\epsilon_{\text{He3},j} = 1.6 \cdot 10^{-5}$, $\epsilon_{\text{He4},j} = 4 \cdot 10^{-2}$, $\epsilon_{\text{Fe},j} = 1 \cdot 10^{-4}$ and $\epsilon_{\text{O},j} = 8 \cdot 10^{-4}$ (based on Lodders 2003).

CSA supports distribution shapes of $\kappa = 15$, $\kappa = 12$, and values from the range $\kappa \in [2, 6]$. The value of 15 is considered close to a Maxwellian distribution. Alternatively, the parameter κ can be set to follow a linear trend between $r = 1.5 R_{\odot}$ and $3 R_{\odot}$ from 6 to 2 (and constant outside this range). This simulates how, at small radial distances and with higher gas densities, particles have a higher chance of thermalising. The particle speed v is measured in the upstream plasma frame. We use mass-proportional temperatures for different ion species and the proton kinetic temperature is taken to agree with the radial solar wind model.

5.6.1   Monte Carlo tests for injection

The protons of each population are represented by $N_{\text{H}j}$ Monte Carlo particles, and for each minor ion species there are $N_{\alpha j} = \frac{1}{4} N_{\text{H}j}$ Monte Carlo particles. The particles are distributed uniformly along the path of the shock, with positions randomised from $r_i \in [r_{\text{s}}(t = 0), r_{\text{s}}(t = t_{\text{max}}))$. As the average spatial separation of particles is $\delta r_{\alpha j} = (r_{\text{s}}(t_{\text{max}}) - r_{\text{s}}(0))/N_{\alpha j}$, each

simulated particle is assigned a representative weight of

$$w_{ij} = \int_{r_i}^{r_i + \delta r_{\alpha j}} \mathcal{A}(r) n_{\alpha j}(r) \, \mathrm{d}r, \tag{5.22}$$

where $n_{\alpha j}$ is the particle density and $\mathcal{A}(r)$ is the flux tube cross-sectional area.

We solve analytical speed thresholds for particle injection due to both reflection at the shock and scatterings in the downstream. As presented in **Paper III**, the minimum plasma frame speed for particles resulting in injection can be solved from our solar wind and shock parameters. For each particle, at position r_i, we find two threshold speeds for reflection, and 1-3 threshold speeds for injection after downstream isotropisation. Downstream isotropisation threshold speeds resulting from extrema at $\mu \neq \pm 1$ (see **Paper III**, appendix B) are solved through numerical iteration. Finding the smallest of these threshold speeds can, for some simulation parameters and particle positions, result in a minimum speed of 0. In these circumstances, completely cold seed particles have a nonzero probability of injection, and injection test speeds have no lower limit.

The particle speed is randomised from the κ-distribution, allowing only speeds which exceed the injection threshold speed. The randomisation is done via a numerical look-up table, which is created for values of $\kappa = 2, 2.5, 3, \ldots, 6, 12,$ and 15. Linear interpolation is used to find the speed associated with the randomisation parameter, a uniformly distributed random number. If the value of κ_i assigned to the particle is not included in the table, but $\kappa_i \in [2, 6]$, a second linear interpolation is performed between the two values found by using the nearest tabulated values of κ. The κ-distribution representative velocity parameter w_0 is solved from the radial temperature profile $T(r)$ or, if given, a constant solar wind plasma temperature.

Seed particles are considered isotropic in the upstream plasma frame. Taking into account flux conservation, as presented in **Paper III**, the pitch-angle cosine μ of particles with speeds $v < u_1$ is randomised as

$$\mu|_{v<u_1} = \frac{u_1}{v} - \sqrt{(\frac{u_1}{v} - 1)^2 + 4\frac{u_1}{v}\mathcal{S}}, \tag{5.23}$$

where μ receives values from the range $-1 < \mu \leq +1$ and $\mathcal{S}$ is a uniformly distributed random number in the range $[0,1)$.

For particles with speeds $v > u_1$, information of the propagating shock can extend into the upstream, affecting the incident particle pitch-angle distribution. Thus, we place particles in the upstream at a distance of $x_1 = 2\lambda$, with

$$\mu|_{v>u_1} = -\left(-\frac{u_1}{v} + (1 + \frac{u_1}{v})\sqrt{\mathcal{S}}\right), \qquad (5.24)$$

which limits μ to values from the range $-1 < \mu \leq \frac{u_1}{v}$, i.e. travelling towards the shock. The particles are then scattered and convected in the upstream until they reach the shock front.

When particles reach the shock front, they are tested for particle-shock interaction to find their probability of returning to the upstream P_{ret}. Successfully returning particles are considered injected.

5.6.2 The negative binomial distribution and the minimum variance unbiased estimator

Despite calculating minimum injection speeds, randomised particles might not be injected into the acceleration process. To retain statistical accuracy, we employ statistical methods and note that the amount of successful injections follows a negative binomial distribution. We randomise particles in groups of varying sizes, where for each attempt within the group, the particle receives newly randomised values of v and μ. Each group will result in injection of a single representative particle, and the group size is dependent on injection probability. First, the newest particle in a group is tested for reflection. Reflected particles are returned to the upstream and considered injected, with $P_{\text{ret}} = 1$. Non-reflected particles are transmitted to the downstream, with v' and μ' calculated according to equations (5.15) and (5.14), after which downstream propagation and scattering follows.

We attempt new particles until each group has $\mathcal{R} = 5$ successfully injected particles (hereafter referred to as successes). The amount of uninjected or unsuccessful particles in the group is designated $\mathcal{K}$. From $\mathcal{R}$ and $\mathcal{K}$, we estimate the statistical probability, $\mathcal{P}$, of the group resulting in a particle designated as successful. With $\mathcal{P}$ calculated, the last successful particle of the group is considered injected, and is used to represent the whole group.

As a precaution against excessively low success probabilities, the group size is limited to $(\mathcal{R} + \mathcal{K}) = 10^6$. If this limit is reached, and at least 2

successes are encountered, the values of $\mathcal{R}_i$ and $\mathcal{K}_i$ associated with the last encountered success are used to calculate $\mathcal{P}$. If the tests resulted in only 0 or 1 successes, the group is considered as resulting in no injection.

In estimating $\mathcal{P}$, the minimum variance unbiased estimator (see, e.g., Lehmann & Casella 1998) is used, which gives

$$\mathcal{P} = \frac{\mathcal{R} - 1}{\mathcal{R} + \mathcal{K} - 1}. \tag{5.25}$$

It should be noted, however, that the actual probability of injection for a particle is $P_{\mathrm{inj}} = \mathcal{P} P_{\mathrm{ret}}$, where P_{ret} is the probability of return associated with the last encountered success. Thus, the injected weight of the Monte Carlo particle is found as $W_{ij} = w_{ij} P_{\mathrm{inj}}$, where w_{ij} is the representative weight of upstream seed particles assigned to this group, as shown in equation (5.22).

5.7 Data output

CSA results are saved using the Flexible Image Transport System (FITS, see, e.g., Wells et al. 1981). Each file consists of multiple Header + Data Units (HDUs). Each HDU contains header information with all simulation parameters and definitions on how to interpret the contained data.

Turbulence power files contain 3 HDUs.

- The primary data unit contains a 3-dimensional data cube with dimensions equal to the number of output time steps, the number of radial bins, and the number of frequency bins. Each data value represents the wave power $P(f)$ at the given output time step, radial position, and frequency.

- The first extension data unit contains a 2-dimensional array of the radial positions associated with each cell, in units of solar radius, at each output time step.

- The second extension data unit contains a 2-dimensional array of the frequencies associated with each cell, given in hertz, at each output time step.

- The third extension data unit contains a table with a single data column of simulation times at each output time step, given in seconds.

Particle distribution files contain 3 HDUs. A separate file is created for each active ion species. Particle counts can be chosen to represent the number of particles within the bin or the omnidirectional intensity I in units $\mathrm{cm^{-2}\,sr^{-1}\,s^{-1}\,MeV^{-1}}$. This omnidirectional intensity is defined as

$$\frac{\mathrm{d}I}{\mathrm{d}E} = \frac{p^2}{2} \int f(p,\mu)\,\mathrm{d}\mu = \frac{1}{4\pi}\frac{\mathrm{d}N}{\mathrm{d}^3x\,\mathrm{d}p}. \tag{5.26}$$

- The primary data unit contains a 3-dimensional data cube with dimensions equal to the number of output time steps, the number of radial bins, and the number of speed bins. Each data value represents the chosen particle count within the bin, starting at the given radial position and speed, at the given time.

- The first extension data unit contains a 2-dimensional array of the radial positions associated with each cell, in units of solar radius, at each output time step.

- The second extension data unit contains a 2-dimensional array of the particle speeds associated with each cell, given in units c, at each output time step.

- The third extension data unit contains a table with the following data columns:

    1. Simulation times at each output time step, given in seconds.
    2. Amount of active particles within the simulation at each output time step.
    3. Amount of particles injected into the simulation during each time step.
    4. Amount of particles leaving the simulation during each time step.
    5. Weighted average age of active particles within the simulation at each output time step, given in seconds.
    6. Weighted average age of particles injected into the simulation during each time step, given in seconds.
    7. Weighted average age of particles leaving the simulation during each time step, given in seconds.

Each FITS file contains only counts and weighted ages of particles belonging to the appropriate ion population.

For enhanced statistical stability, particle counts can be integrated over the length of the output time step (at Δt_i intervals) instead of representing a snapshot situation at the moment of output.

Part III

Results

Chapter 6

Results of DSA at coronal shocks

In this chapter, we present simulation results of DSA at coronal shocks. These results span a larger parameter space than presented in the articles included in this thesis. We compare proton and minor ion spectra, wave amplification results, and wave power spectra at shocks of varying shock-normal velocities and shock-normal angles. Our results show how DSA efficiency at coronal shocks varies greatly based on shock and seed population properties.

6.1   Simulation parameters

In the presented simulations, we have used different constant values for the shock-normal velocity V_s and the shock-normal angle $\theta_{B\mathrm{n}}$. We assume the solar wind to consist of both thermal and non-thermal populations. **Paper III** contains detailed assessment of the injection process, allowing us to adjust simulation input parameters for suitable numerical efficiency. The non-thermal seed particle population is modelled as a $\kappa = 2$ distribution, and is set to 1% of the solar wind density. The thermal population should be the remaining 99% of solar wind density. Our injection method treats seed particles as pure test particles, instead of allowing them to affect the properties and spatial profile of the shock front or plasma flows. Thus, it is possible that our method overestimates the particle injection from the thermal population. For this reason, we artificially inhibit the injection of thermal particles, seeding them as only 10% of solar wind density. This decreases the possible injection of thermal particles, but does not affect the

suprathermal population. For minor ion abundances, we used estimates presented in **Paper II** (see, e.g., Lodders 2003), both for thermal and suprathermal populations.

We simulate particle scatterings in the downstream up to the return boundary $\mathcal{B}$, but based on the results of **Paper III**, we do not simulate cross-field diffusion. Our simulation parameters are listed in tables 6.1 through 6.4.

number of radial grid points	$n_r = 401$
minimum value for radial grid points	$r_0 = 5 \cdot 10^{-3} \, R_\odot$
maximum value for radial grid points	$r_1 = 308.167 \, R_\odot$
number of velocity grid points	$n_v = 81$
minimum value for velocity grid points	$v_0 = 10^8 \, \mathrm{cm\,s^{-1}}$
maximum value for velocity grid points	$v_1 = 2.9 \cdot 10^{10} \, \mathrm{cm\,s^{-1}}$
number of frequency grid points	$n_f = 81$
minimum value for frequency grid points	$f_0 = 10^{-5} \, \mathrm{s^{-1}}$
maximum value for frequency grid points	$f_1 = 10^3 \, \mathrm{s^{-1}}$

Table 6.1: Simulation parameters 1: Data grids

6.1.1 Injection efficiency

As presented in **Paper III**, oblique shocks are inefficient at injecting thermal particles into the acceleration process. We attempted injection of both $\kappa = 2$ and $\kappa = 15$ populations for shocks with $\theta_{Bn} = 0°$ and $\theta_{Bn} = 15°$, but omitted tests at higher shock-normal angles. In table 6.5, we list the injection efficiencies of protons for all presented simulations, and show that injection of thermal particles was negligible in all cases except for the parallel $V_s = 1500 \, \mathrm{km\,s^{-1}}$ case.

Shock-normal velocity V_s (constant)	1000, 1500, or 2000 km s^{-1}
Shock-normal angle θ_{Bn} (constant)	0°, 15°, 30°, or 60°
Shock starting position r_{s0}	$2\,R_\odot$
$P \propto f^{-1}$ initialisation distance r_{w0}	$1.5\,R_\odot$
Simulation time t_{max}	640 s
Output time step t_{out}	10 s
Internal time step Δt (adjusted dynamically)	$6.4 \cdot 10^{-3}$ s
Minimum value for Γ_w per time step	$\Gamma_{min} = 4 \cdot 10^{-3}$
Maximum value for Γ_w per time step	$\Gamma_{max} = 0.2$
Cross-shock potential strength	$\phi = 0.12$

Table 6.2: Simulation parameters 2: Shock and simulation parameters

Magnetic flux tube supra-expansion coefficient	$b_f = 1.9$
Magnetic field strength at 1 AU	$B(1\,\text{AU}) = 2.90\,\text{nT}$
Solar wind speed at 1 AU	$u_{sw}(1\,\text{AU}) = 380\,\text{km s}^{-1}$
Alfvén speed at 1 AU	$v_A(1\,\text{AU}) = 20\,\text{km s}^{-1}$
Mean free path for 100 keV proton at 1 AU	$\lambda(1\,\text{AU}) = 55\,R_\odot$

Table 6.3: Simulation parameters 3: Solar wind parameters

6.1.2   The turbulent trapping region

Throughout our interpretation of the simulation results, we will be referring to the *turbulent trapping region*, as defined in section 4.2.4. Within the turbulent trapping region, particles are confined to the vicinity of the shock, experiencing efficient DSA. In figure 6.1, we show contour plots of omnidirectional proton intensities along with the boundary of the turbulent

Proton density for population 1 ($\kappa = 2$)	$\epsilon_{\text{H1}} = 0.01$
Proton density for population 2 ($\kappa = 15$)	$\epsilon_{\text{H2}} = 0.1$
Proportional $^{3}\text{He}^{2+}$ density	$\epsilon_{\text{He3,1}} = \epsilon_{\text{He3,2}} = 1.6 \cdot 10^{-5}$
Proportional $^{4}\text{He}^{2+}$ density	$\epsilon_{\text{He4,1}} = \epsilon_{\text{He4,2}} = 4 \cdot 10^{-2}$
Proportional $^{16}\text{O}^{6+}$ density	$\epsilon_{\text{O,1}} = \epsilon_{\text{O,2}} = 1 \cdot 10^{-4}$
Proportional $^{56}\text{Fe}^{14+}$ density	$\epsilon_{\text{Fe,1}} = \epsilon_{\text{Fe,2}} = 8 \cdot 10^{-4}$

Table 6.4: Simulation parameters 4: Particle populations

V_{s} [km s^{-1}]	$\theta_{B\text{n}}$ [deg]	Eff($\kappa = 2$)	Eff($\kappa = 15$)
1000	15	$1.5 \cdot 10^{-3}$	$3 \cdot 10^{-6}$
1000	30	$9.7 \cdot 10^{-4}$	n/a
1500	0	$6.2 \cdot 10^{-2}$	$6.2 \cdot 10^{-2}$
1500	15	$1.0 \cdot 10^{-3}$	$8 \cdot 10^{-9}$
1500	30	$7.5 \cdot 10^{-4}$	n/a
1500	60	$1.3 \cdot 10^{-4}$	n/a
2000	15	$5.9 \cdot 10^{-4}$	$9 \cdot 10^{-7}$
2000	30	$4.2 \cdot 10^{-4}$	n/a

Table 6.5: Injection efficiencies: Particles entering the simulation as a fraction of tested solar wind particles. Shocks with $\theta_{B\text{n}} = 30°$ or $\theta_{B\text{n}} = 60°$ were only tested for injection from the $\kappa = 2$ seed population.

trapping region. As can be seen in the left image, with $V_{\text{s}} = 1500\,\text{km}\,\text{s}^{-1}$ and $\theta_{B\text{n}} = 0°$, the turbulent trapping region extends to high energies and encompasses the whole proton population, save for high-energy protons escaping in the radial direction. Conversely, in the right-hand image, with

$V_{\rm s} = 1500\,{\rm km\,s}^{-1}$ and $\theta_{B{\rm n}} = 15°$, we see significant injection of particles which are not contained within the turbulent trapping region, and thus, will not experience significant DSA.

The particle energies associated with boundaries of the turbulent trapping regions are shown in figure 6.2. Within the turbulent trapping region, particle populations should approach a shape described by a power-law index Γ_E in agreement with acceleration theory (see section 4.3). Outside the turbulent trapping region, particles are mostly limited to energy gains from SDA during injection.
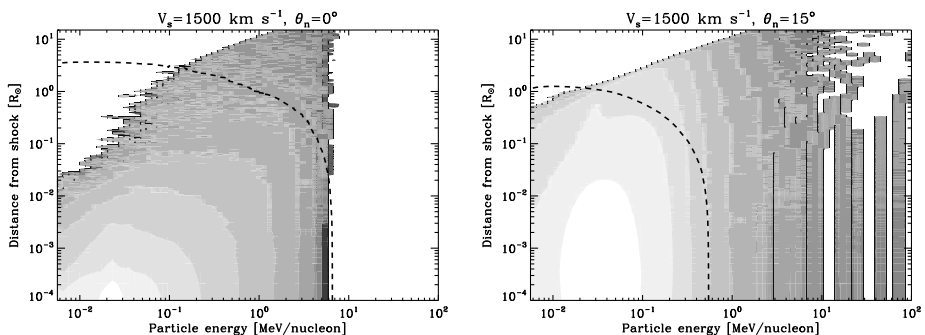
Figure 6.1: Contours of omnidirectional proton intensities after 640 seconds of simulation along with the boundary of the turbulent trapping region (dashed curve). The left figure, with shock-normal velocity $V_{\rm s} = 1500\,{\rm km\,s}^{-1}$ and shock-normal angle $\theta_{B{\rm n}} = 0°$, displays efficient trapping, with only a few far-out particles escaping. The right figure, with shock-normal velocity $V_{\rm s} = 1500\,{\rm km\,s}^{-1}$ and shock-normal angle $\theta_{B{\rm n}} = 15°$, displays weak trapping, with high-energy particles experiencing negligible DSA.

6.2 Wave amplification

In figure 6.3, we show a selection of wave amplification results. For all graphs, the wave amplification coefficient $\Gamma_{\rm w}$ (equation 3.38) was integrated over the whole simulation time. Results are shown both for the first row of wave power grid cells in front of the shock (left column), and integrated
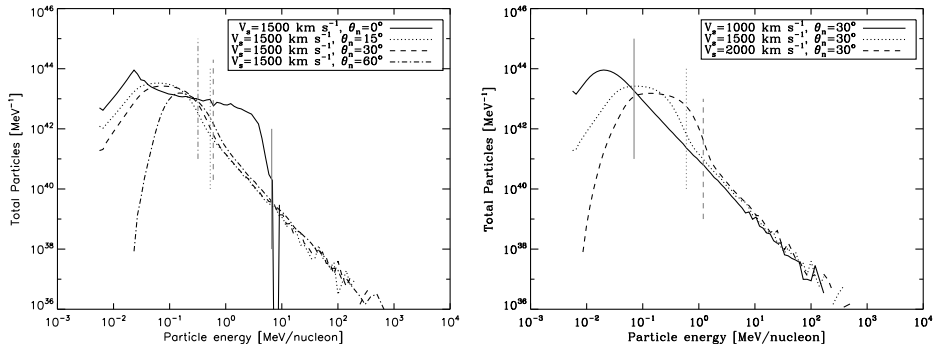
Figure 6.2: Spatially integrated accelerated proton spectra
($\mathrm{d}N/\mathrm{d}E$) after 640 seconds of simulation. Also plotted,
with grey vertical lines, are the near-shock maximum ener-
gies associated with the edge of the turbulent trapping region.
Shown are comparisons for different shock-normal angles using
$V_\mathrm{s} = 1500\,\mathrm{km\,s^{-1}}$ (left image), and different shock-normal ve-
locities using $\theta_{B\mathrm{n}} = 30°$ (right image). Particle spectra exhibit
build-ups within the turbulent trapping region.

over the whole spatial grid (right column). The results of integrating over
the whole spatial grid should be interpreted carefully, as they do not have
a direct physical counterpart.

As the shock-normal velocity V_s or shock-normal angle $\theta_{B\mathrm{n}}$ increases,
the speed of the shock along the field line increases, and with it, the energy
gained by a particle per particle-shock interaction. This leads to particles
having larger energies, and drives wave amplification to lower (resonant)
frequencies.

The top row in figure 6.3 shows how shock-normal angle $\theta_{B\mathrm{n}}$ can have a
significant effect on Alfvén wave amplification, especially in the near-shock
region. The variation on wave amplification magnitude is directly related
to the injection efficiency of the shock, which has a strong dependence on
the shock-normal angle $\theta_{B\mathrm{n}}$. The peak amplification values for $\theta_{B\mathrm{n}} = 15°$
and $\theta_{B\mathrm{n}} = 30°$ are remarkably similar. This can be explained by referring
to **Paper III**, where the injected flux for these two cases are very similar,
though for $\theta_{B\mathrm{n}} = 15°$ it is injection through downstream scatterings that
dominates, and for $\theta_{B\mathrm{n}} = 30°$, injection through reflection.

From the middle and bottom rows, where the shock-normal velocity is varied for a constant shock-normal angle, we can see that the maximal amplification amplitude does not have a strong dependence on shock-normal velocity, but its peak frequency does. Comparing amplification spectra near the shock and for the whole spatial range, we see that at low frequencies (i.e. resonant with high energy particles), amplification is weak in the near-shock region. Over the whole spatial range, however, amplification is stronger. This is due to fast particles exiting the vicinity of the shock, as they are not within the turbulent trapping region.

In figure 6.4, we show samples of integrated wave amplification coefficient Γ_{w} for different minor ion species. The top left image (amplification in front of the shock, $V_{\mathrm{s}} = 1500\,\mathrm{km\,s^{-1}}$, $\theta_{B\mathrm{n}} = 0°$) is in good agreement with the results presented in **Paper II**. With increasing shock-normal angle (the second and third row, left images), wave amplification in front of the shock extends well to lower frequencies, where ${}^{2}\mathrm{He}^{4+}$ causes turbulence amplification of amounts comparable with protons. However, this amplification is not enough to extend the turbulent trapping region to these frequencies, so the bootstrapped DSA process does not become effective for high energy particles.

When assessing turbulence amplification over the whole spatial grid (fig. 6.4, right column), we find that as for protons, minor ions generate negligible wave amplification at low frequencies through escaping particles. In the parallel shock case (top right), we can distinguish a strong bump of amplification due to freshly injected particles (from approximately 50 to 200 Hz, resembling the near-shock amplification) in addition to an amplification bump extending all the way to ~ 0.1 Hz. This secondary amplification region is due to efficient DSA and high-energy particle streaming in the near-shock region, with the low-frequency edge corresponding with the boundary of the turbulent trapping region. The differences in minor ion resonant frequencies are easily distinguished in this picture.
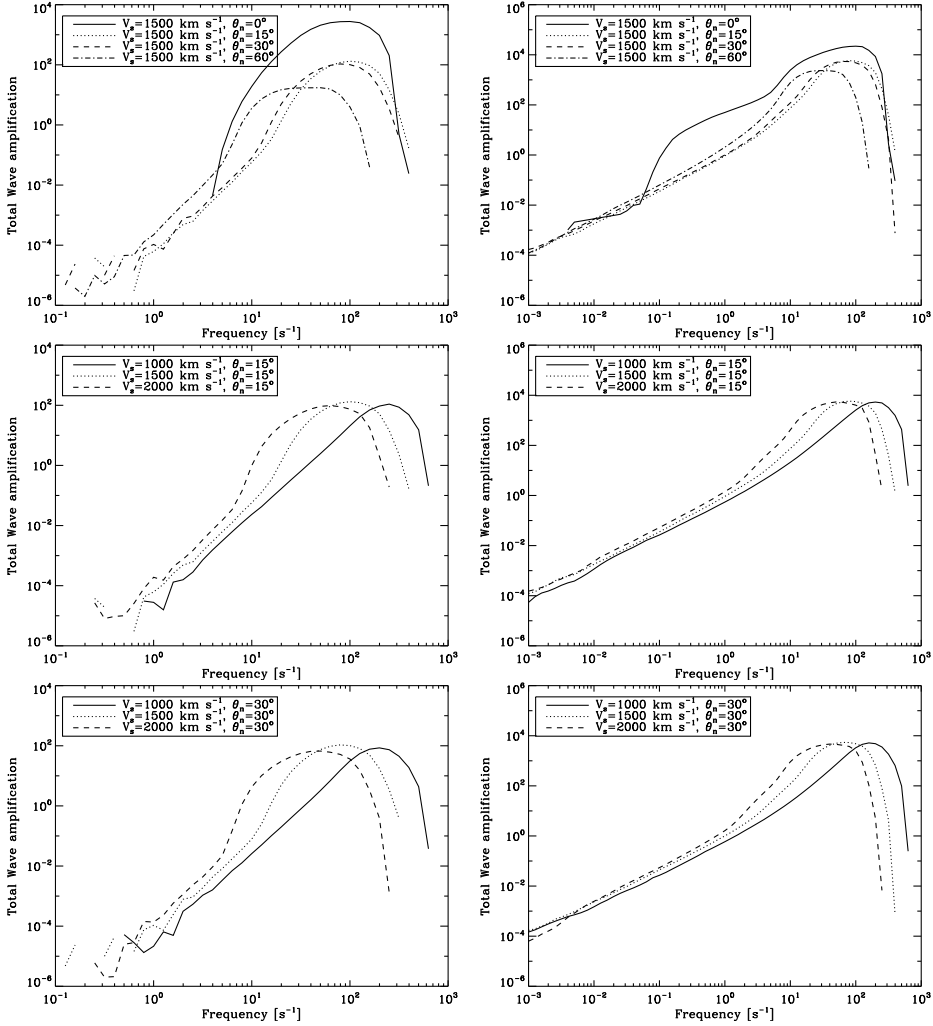
Figure 6.3: Wave amplification due to streaming protons integrated over 640 seconds of simulation. The left column shows amplification in front of the shock (at a distance of $3 \cdot 10^{-4} \, R_\odot$), and the right column shows amplification integrated over the whole spatial grid. Shown are comparisons for different shock-normal angles using $V_s = 1500 \, \text{km s}^{-1}$ (top row), different shock-normal velocities using $\theta_{Bn} = 15°$ (middle row), and different shock-normal velocities using $\theta_{Bn} = 30°$ (bottom row).
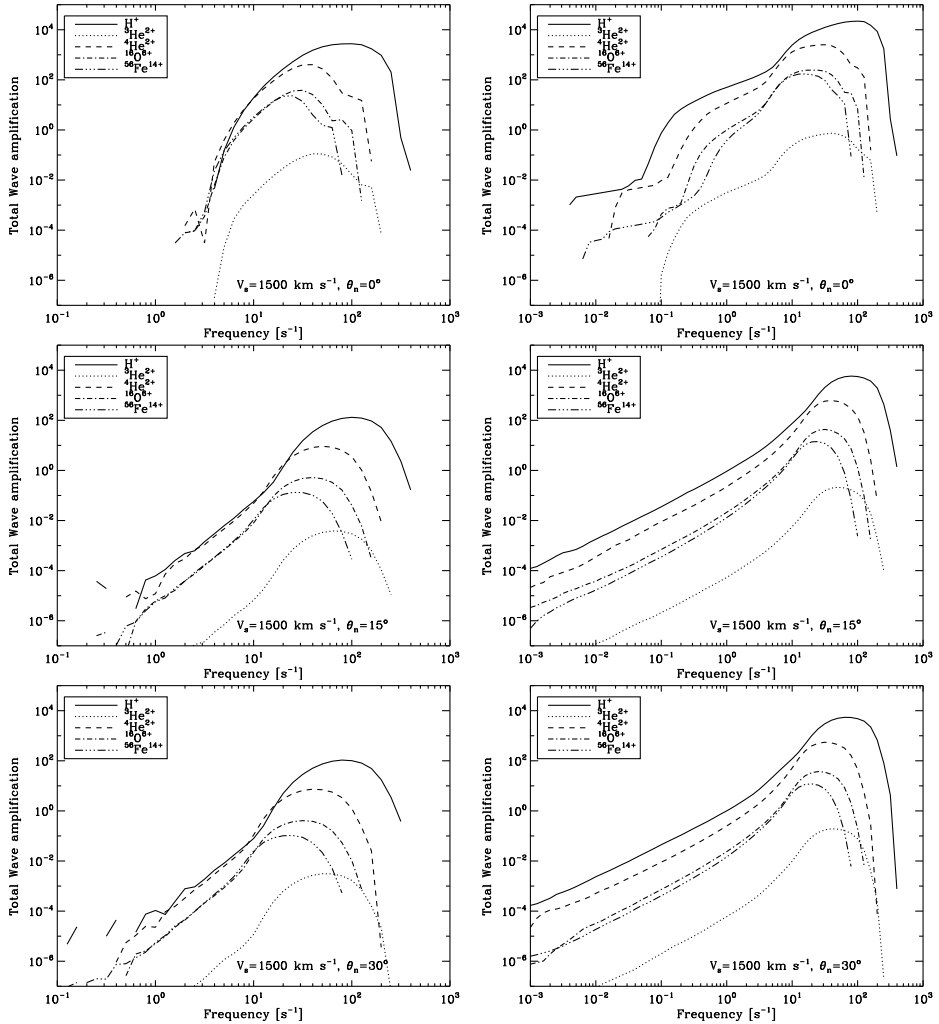
Figure 6.4: Wave amplification due to streaming ions (protons, $^3\text{He}^{2+}$, $^4\text{He}^{2+}$, $^{16}\text{O}^{6+}$, and $^{56}\text{Fe}^{14+}$) integrated over 640 seconds of simulation. The left column shows amplification in front of the shock (at a distance of $3 \cdot 10^{-4} \, R_\odot$), and the right column shows amplification integrated over the whole spatial grid. Presented cases are for shock-normal velocity $V_s = 1500 \, \text{km s}^{-1}$ and three different shock-normal angles: $\theta_{Bn} = 0°$ (top), $\theta_{Bn} = 15°$ (middle), and $\theta_{Bn} = 30°$ (bottom).

6.3   Alfvén wave power spectra

In figure 6.5, we compare the spectra of Alfvénic turbulence in front of various shocks. In the left figure, we compare three cases with shock-normal angle $\theta_{Bn} = 15°$ and shock-normal velocities $V_s = 1000\,\mathrm{km\,s^{-1}}$, $V_s = 1500\,\mathrm{km\,s^{-1}}$, and $V_s = 2000\,\mathrm{km\,s^{-1}}$. As the shock-normal velocity increases, the peak of the amplified spectrum moves to smaller frequencies and becomes narrower. This is a well-understood result, as the momentum increase a particle receives during each shock interaction, and thus, the energy of particles after injection into the acceleration process, increases with the flow speed u_1 at the shock.

The results of keeping the shock-normal velocity constant and varying the shock obliquity angle θ_{Bn} are shown in the right half of figure 6.5. The parallel shock ($\theta_{Bn} = 0°$) has by far the most wave power, with amplified wave power extending to frequencies as low as $1\,\mathrm{Hz}$. This extension of wave power to small frequencies is due to inverse cascading of wave power, modelled through diffusion (see section 3.5). This is confirmed by calculating the resonant frequency (equation 3.28) of the largest particle energy attained (approximately $5\,\mathrm{MeV}$), which, with our solar wind model, gives $f_{\mathrm{res}} \approx 5\,\mathrm{Hz}$.

It is also noteworthy, that the cases $\theta_{Bn} = 15°$ and $\theta_{Bn} = 30°$ do not differ much. This is in agreement with wave amplification comparison of these two cases. With increasing obliquity, the HT-frame speed of inflowing gas increases, which causes the $\theta_{Bn} = 60°$ to peak at a lower frequency. The parallel case of $\theta_{Bn} = 0°$, however, does not peak at a larger frequency than the other cases. This is due to erosion of the peak due to diffusion. The resonant frequency of the most abundant freshly injected particles (with $E \approx 30\,\mathrm{keV}$) is $f_{\mathrm{res}} \approx 130\,\mathrm{Hz}$, well past the peak of the wave power spectrum.

The difference in spectral amplitude at low (unenhanced) frequencies is due to WKB-transport effects and the difference in distance traversed by the shock after 640 seconds of simulation.
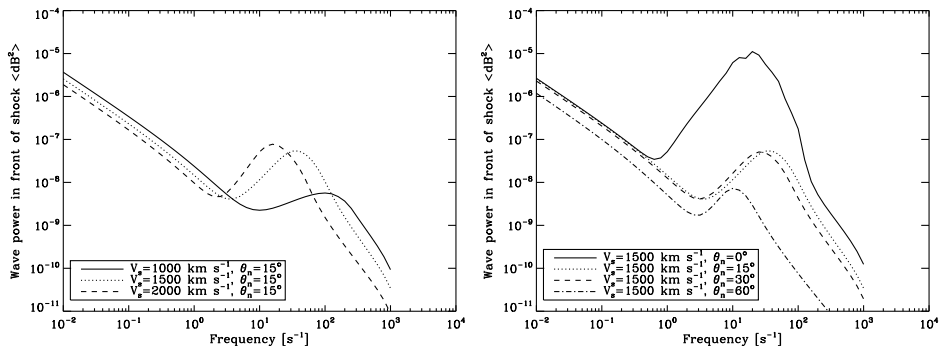
Figure 6.5: Wave power spectra in front of the shock (at a distance of $3 \cdot 10^{-4} R_\odot$) after 640 seconds of simulation. The left figure shows shock-normal angle $\theta_{Bn} = 15°$ and results for three different shock-normal velocities: $V_s = 1000\,\mathrm{km\,s^{-1}}$, $V_s = 1500\,\mathrm{km\,s^{-1}}$, and $V_s = 2000\,\mathrm{km\,s^{-1}}$. The right figure shows shock-normal velocity $V_s = 1500\,\mathrm{km\,s^{-1}}$ and results for four different shock-normal angles: $\theta_{Bn} = 0°, 15°, 30°$, and $60°$.

6.4   Accelerated proton spectra

The spectra of accelerated protons, after 640 seconds of acceleration, are shown in figure 6.6. The left-hand column consists of omnidirectional proton intensity spectra $(\mathrm{d}I/\mathrm{d}E)$ in front of the shock, with the right column displaying spectra of protons upstream of the shock, spatially integrated over the whole flux tube $(\mathrm{d}N/\mathrm{d}E)$.

We find apparent power-law spectra for three of the presented omnidirectional intensity spectra: with $V_s = 1500\,\mathrm{km\,s^{-1}}$, the parallel case has a power-law of approximately -2.5, and with $V_s = 1000\,\mathrm{km\,s^{-1}}$. Cases with $\theta_{Bn} = 15°$ and $\theta_{Bn} = 30°$ appear to have power-laws of approximately -3.

Many omnidirectional intensity spectra, however, do not seem to follow power-laws. At low energies, a soft bump, resulting from particle trapping, can be seen in the 10 keV to 1 MeV region. At high energies, a power-law of -2.5 or -3 could fit the data, but weak statistics are a problem.

By investigating infinitesimally short acceleration simulations, we were able to deduce that the injected omnidirectional intensity spectra of parti-

cles right in front of oblique shocks do also follow a -2 power-law, but only for a very short period of time. Within seconds the spectrum begins to change, as the turbulent trapping region begins to form, increasing particle intensities at low energies. At high energies, particles are not confined to the shock vicinity, rapidly escaping further out.

Next, we compare the accelerated population spectra with the power-laws and analysis methods presented in section 4.3. The equation for the scattering centre compression ratio (4.8), using upstream and downstream cross-helicities $H_{c1} = -1$ and $H_{c2} = 0$, becomes $r_{sc} = r_g(M_A - 1)/M_A$. This form, despite not reducing to 1 when $M_A \to 1$, can be used to estimate the accelerated population (steady-state) power-law, as an approximation accounting for injection through both reflection and isotropisation in the downstream.

The momentum-dependent spectral power-law is found using the relation $\Gamma_p = (r_{sc} + 2)/(r_{sc} - 1)$, and the energy-dependent power-law, with $dI/dE \propto E^{-\Gamma_E}$, can be found with $\Gamma_E = \frac{1}{2}\Gamma_p$. If the power-law of the source population is harder than the one found from compression ratio calculations, the accelerated proton population should exhibit the source population power-law, with amplified intensity. Our source population is a combination of $\kappa = 2$ and $\kappa = 15$ populations, with the $\kappa = 2$ population dominating for oblique shocks. In these cases, and at high energies, the $\kappa = 2$ distribution is injected as is, resulting in particle spectra with power-laws of $\Gamma_E = 2$.

For the $V_s = 1500\,\mathrm{km\,s^{-1}}$ parallel shock case, we find values of roughly $M_A \approx 2$ and $r_{sc} \approx 1.85$, which result in a power-law of $\Gamma_E \approx 2.3$, which is a moderately good match with the omnidirectional intensity spectra found near the shock. This spectrum is a result of efficient injection from the thermal $\kappa = 15$ population, along with efficient DSA within the turbulent trapping region, extending along the whole accelerated particle spectrum. A power-law related to the $\kappa = 2$ population cannot be seen due to the efficiency of thermal particle injection and associated DSA.

For $V_s = 1500\,\mathrm{km\,s^{-1}}$ oblique shocks, injection of the thermal $\kappa = 15$ population is negligible. Analytical solutions based on scattering centre compression ratios find $\Gamma_E \approx 3.1$ for $\theta_{Bn} = 15°$ and $\Gamma_E \approx 3.4$ for $\theta_{Bn} = 30°$. These low scattering centre compression ratio should result in a particle spectrum with the source population power-law of -2. As mentioned, this was found briefly at the start of the simulation, before turbulent trapping of low-energy particles alters the shape of the spectrum.

The right-hand column of figure 6.6, displaying spatially integrated accelerated proton spectra $(\mathrm{d}N/\mathrm{d}E)$, is capable of displaying population power-laws with better statistics, and thus, to higher energies. All cases with oblique shocks display a clear $\Gamma_E \approx 2$ power-law, consistent with injection of a $\kappa = 2$ seed population. This population has experienced only reflection and shock drift acceleration at the shock. The build-up within the turbulent trapping region is also visible.

The parallel shock $V_s = 1500 \, \mathrm{km\,s^{-1}}$ case instead appears to display a much harder power-law of $\Gamma_E \approx 0.43$, which ends abruptly. This power-law, however, is an artefact of including a far-escaping accelerated population which consists of only high-energy protons.

One reason for an abrupt cut-off in the parallel shock case is our method of particle injection - as the shock injects a significant amount of thermal seed particles, statistics do not allow for many very strongly suprathermal particles to be injected. The parallel case did not seed protons above $\sim 1 \, \mathrm{MeV}$ (still well below the maximum attained energy), whereas for oblique cases injection continued to $\sim 10 \, \mathrm{MeV}$. Thus, further refinement of the implementation of our high-energy particle injection is required in order to obtain comprehensive energy spectra in cases where low-energy particles are readily injected.

We also note that in calculating both omnidirectional intensities in front of the shock, and full-population spectra, we display only particles which have already been injected into the acceleration process by at least one shock encounter. For comparison, proton spectra for $V_s = 1500 \, \mathrm{km\,s^{-1}}$ along with the ambient seed population are shown in figure 6.7.

6.4.1 Accelerated minor ion spectra

Figure 6.8 shows omnidirectional intensity spectra near the shock and spatially integrated particle spectra for five different ion populations, for three different acceleration scenarios. Minor ions are seen to have similar resultant accelerated particle spectra as protons. The spectral shapes associated with injection (for instance, the low energy peak visible for the parallel case) result from injecting minor ions with velocity profiles equal to those of protons. The spectral cut-off energies of the parallel shock case (top row) are in agreement with results presented in **Paper II**.

The presented oblique shock cases (middle and bottom row) result, as for protons, in power-laws associated with the seed population. Thus, our
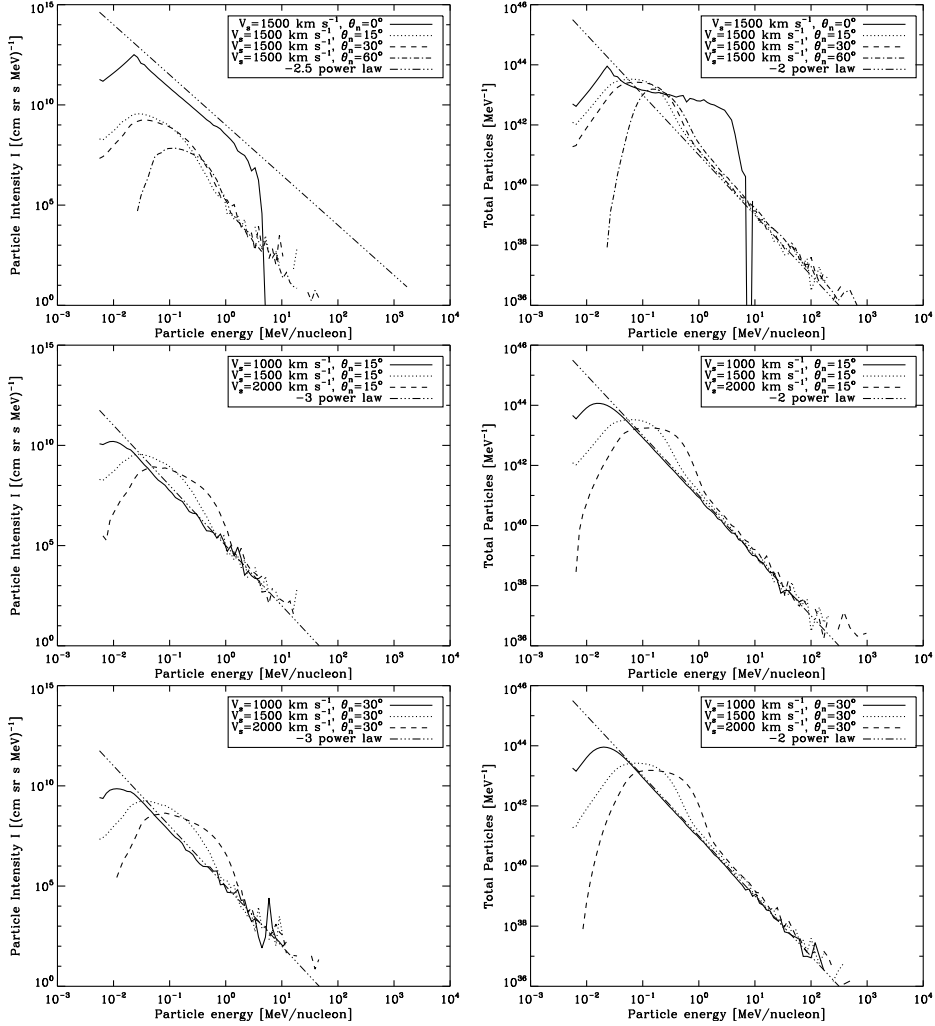
Figure 6.6: Accelerated proton spectra after 640 seconds of simulation. The left column shows omnidirectional intensities in front of the shock, and the right column shows spatially integrated proton spectra ($\mathrm{d}N/\mathrm{d}E$). Shown are comparisons for different shock-normal angles using $V_{\mathrm{s}} = 1500\,\mathrm{km\,s^{-1}}$ (top row), different shock-normal velocities using $\theta_{B\mathrm{n}} = 15°$ (middle row), and different shock-normal velocities using $\theta_{B\mathrm{n}} = 30°$ (bottom row). Included are sample power-laws for comparison.
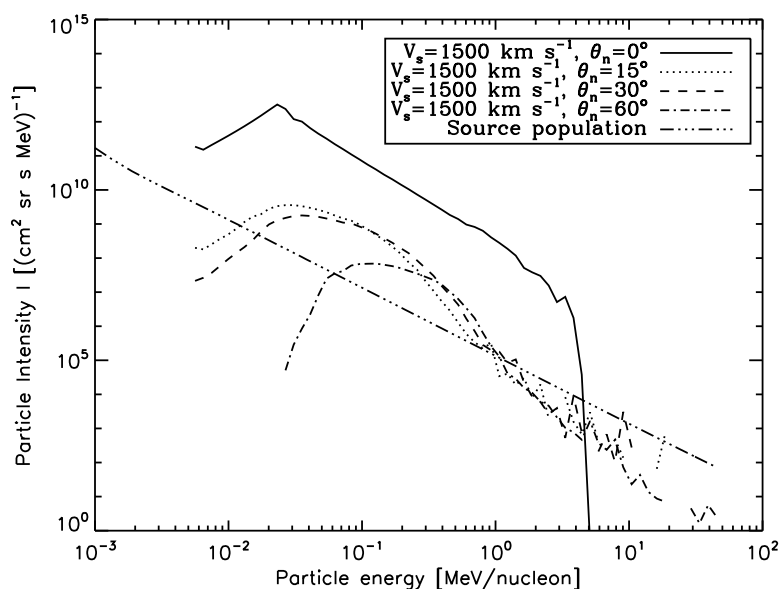
Figure 6.7: Accelerated proton omnidirectional intensities in front of the shock after 640 seconds of simulation. Shown are comparisons for different shock-normal angles using $V_{\mathrm{s}} = 1500\,\mathrm{km\,s^{-1}}$ along with the solar wind source population.

remarks regarding proton spectra are valid for minor ions as well. In the left-hand column, with near-shock omnidirectional intensity spectra, the high-energy portions of the spectra are softer than the seed population suggests, with $\Gamma_E \approx 3$. As for protons, this is a result of the turbulent trapping region increasing low-energy particle fluxes in the near-shock region. In the right-hand column, with spectra integrated over the whole spatial length, spectra approach the value $\Gamma_E \approx 2$, associated with the seed population, experiencing shock drift acceleration with only negligible DSA.

As presented in **Paper II**, minor ion trapping is caused by the same amplified Alfvén wave spectrum which traps protons, and the high-energy boundaries of minor ion trapping regions are related to the shape of the power spectrum. The right-hand column images of figure 6.8 include maximum energies for which the minor ion in question is still within the turbulent trapping region, as denoted by grey vertical lines. As can be seen, these maximum energies coincide with the low-energy intensity increase, just as was seen for protons.

6.5   Time-dependence of acceleration

SEP acceleration, wave amplification, and trapping of energetic particles are dynamic processes, the properties of which can change rapidly over time. In figure 6.9 we show time evolution of omnidirectional proton intensities and wave power spectra for shock-normal velocity $V_s = 1500\,\mathrm{km\,s^{-1}}$ and three different shock-normal angles: $\theta_{Bn} = 0°$, $\theta_{Bn} = 15°$, and $\theta_{Bn} = 30°$.

The parallel case can be seen to generate significant turbulence amplification within the first 10 seconds of simulation, which results in the enhanced particle intensity spectrum forming, albeit only up to ca. 1 MeV. This corresponds with the very steep rise in the power spectrum at approximately 20 Hz. Accordingly, the resonant frequency (equation 3.28) for a 1 MeV particle at the beginning of the simulation is $f_{\mathrm{res}} \approx 23\,\mathrm{Hz}$

As the simulation proceeds, inverse cascading (see section 3.5), modelled through diffusion in wavenumber space, causes enhanced wave power to spread to smaller frequencies, which pushes the turbulent trapping boundary to higher energies. Extension of the turbulent trapping boundary and maximum particle energies are strongly correlated, and an abundance of high energy particles helps amplified wave power extend to smaller frequencies, and vice versa. As stated previously, the resonant frequency for a
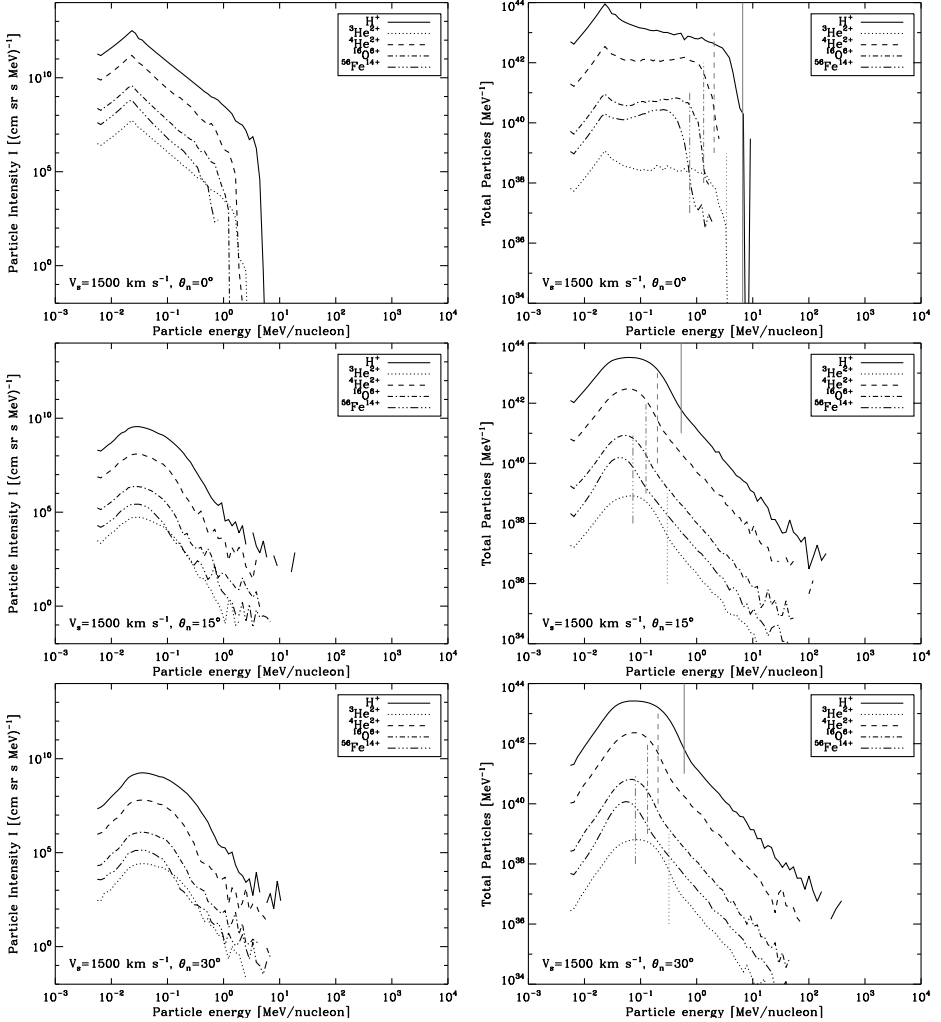
Figure 6.8: Accelerated proton and minor ion spectra after 640 seconds of simulation. The left column shows omnidirectional intensities in front of the shock, and the right column shows spatially integrated particle spectra (dN/dE). Presented cases are for shock-normal velocity $V_s = 1500\,\mathrm{km\,s^{-1}}$ and three different shock-normal angles: $\theta_{Bn} = 0°$ (top), $\theta_{Bn} = 15°$ (middle), and $\theta_{Bn} = 30°$ (bottom). The right-hand column shows also, with grey vertical lines, the near-shock maximum energies for each ion population still within the turbulent trapping region.

5 MeV particle at the end of the simulation is $f_{\rm res} \approx 5\,{\rm Hz}$, and thus, inverse cascading must be responsible for the amplification of wave power below this frequency.

In the oblique cases ($\theta_{B\rm n} = 15°$ and $\theta_{B\rm n} = 30°$), build-up of wave power amplification is much slower, with maximal amplification found at 160 s of elapsed simulation. The enhanced region of wave power spreads to smaller frequencies with elapsed simulation time. In the beginning of the simulation, with little turbulence amplification present, the observed spectra of accelerated protons follow relatively clear injection power-laws. Only as wave power is amplified and the turbulent trapping region forms do we see enhancement of low-energy particle intensities.
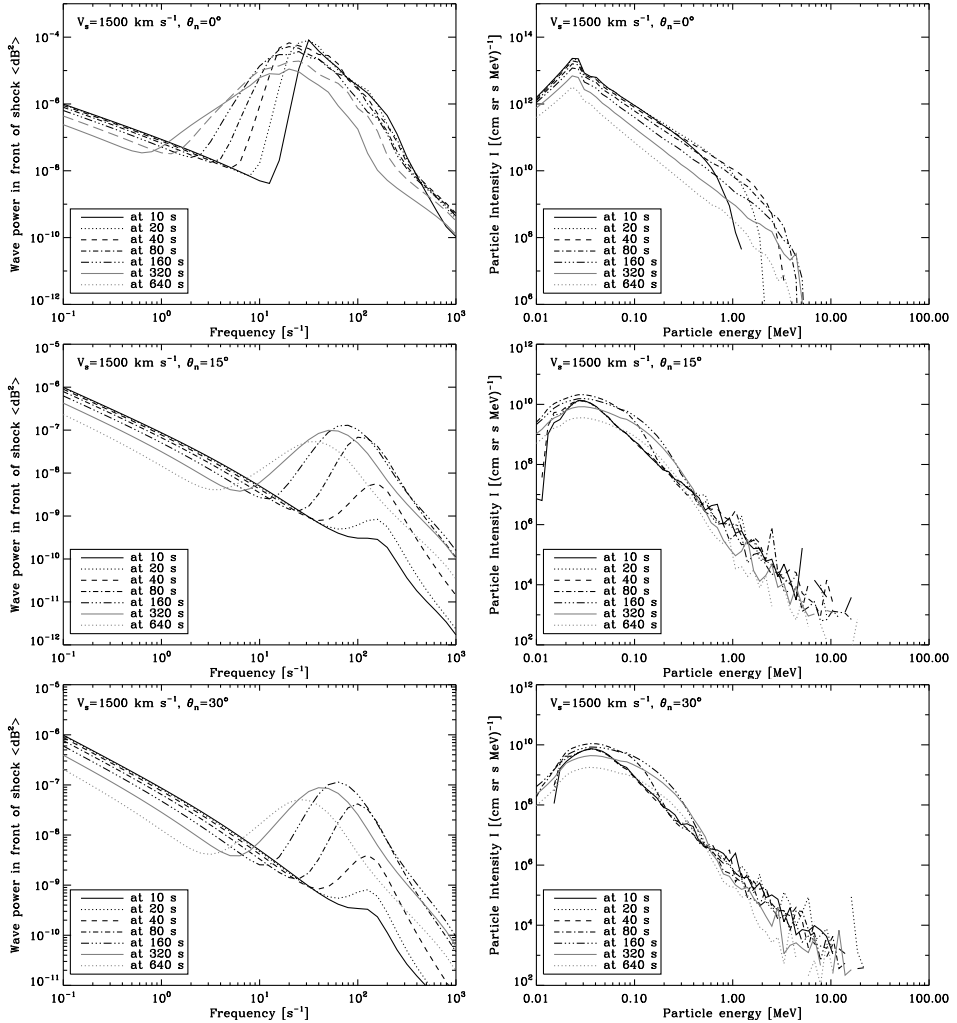
Figure 6.9: Time evolution for particle acceleration and trapping scenarios: The left column shows wave power in front of the shock, and the right column shows omnidirectional proton intensities in front of the shock. Presented cases are for shock-normal velocity $V_{\mathrm{s}} = 1500\,\mathrm{km\,s^{-1}}$ and three different shock-normal angles: $\theta_{B\mathrm{n}} = 0°$ (top), $\theta_{B\mathrm{n}} = 15°$ (middle), and $\theta_{B\mathrm{n}} = 30°$ (bottom).

Chapter 7

Summary & Conclusions

The topics presented in this thesis include theoretical descriptions of particle transport theory, wave transport and evolution, and energetic particle acceleration in the solar corona. In addition, the geometry and parameters of coronal shocks have been discussed. The software suite introduced in chapter 5 has been used to simulate SEP acceleration through DSA at coronal shocks.

7.1   Paper I

The starting point for this study was an extension of analytical simplified solar wind transport combined with Monte Carlo simulated particles and wave amplification. In **Paper I**, we transformed the model to take full advantage of semi-empirical formulations of the solar wind. We attached all tracking grids to the propagating shock, which helped curb numerical instabilities in the near-shock region. Additionally, this allowed us to better optimise the shape of the grid, resulting in increased spatial grid extent and decreased memory and data transfer bandwidth. The method of wave advection on this grid allows for radially varying wave phase speeds, and could be used to implement multiple wave modes, travelling in both directions in the solar wind plasma frame.

The topic of research presented in **Paper I** was decreasing shock propagation speed. We limited our analysis to parallel shocks and applied an approximation of constant gas compression ratio $r_g = 4$. We used a prescribed injection instead of testing the incident solar wind distribution for shock interactions. We found that, for a decelerating shock, acceleration efficiency was slightly decreased, but only when the total amount of par-

ticles taking part in the acceleration process was small. Efficient injection leads to strong trapping of particles to the near-shock region, which leads to repeated shock encounters and acceleration in both cases.

We also note that although a rapidly propagating shock can easily overtake isotropised particles (see section 4.2), it also overtakes generated turbulence rapidly, requiring ongoing amplification of waves. The difference in near-shock spectra is clearly visible in **Paper I**, figure 3. These results do not, however, take into account the differing injection efficiencies of the two shock-velocity profiles.

7.2   Paper II

In **Paper II**, we reported on the acceleration of heavier ions through DSA at coronal shocks. We expanded our model to calculate particle injection through Monte Carlo tests. Seed particle populations supported κ-distributions and were connected to the ambient solar wind density. We limited our study to parallel shocks, and calculated the shock compression ratio according to the hydrodynamic form of equation (2.14) instead of simulating wave pressure with a small shock-normal angle.

We simulated the amplification of waves by minor ions as well as protons, with protons expectedly dominating. Protons are especially important for the launch of the acceleration process, as their charge-to-mass ratio is smallest, and thus, their resonant frequencies are higher than for other particle species. Since slow, thermal particles are resonant with high frequencies, the amplification caused by streaming protons can decrease acceleration time of heavier ions. Through analytical assessment, we found the acceleration time of ions (up to intermediate rigidities) to be proportional to Q/A. Acceleration times up to maximum energies (limited by the turbulent trapping region) were found to be proportional to $(Q/A)^{3/2}$.

As shown in figure 1 of **Paper II**, at low frequencies, the turbulence amplification by minor ions approaches or even overtakes that of protons. Theoretically, this should facilitate better proton acceleration at high energies, as lower energy ions participate in generating suitable trapping in front of the propagating shock.

We assessed parallel shocks with shock-normal velocities $V_s = 1250\,\mathrm{km\,s^{-1}}$, $V_s = 1500\,\mathrm{km\,s^{-1}}$, and $V_s = 1750\,\mathrm{km\,s^{-1}}$. We found that faster shocks resulted in a stronger rise of spectrum at low frequencies. Ion spectral cut-off

energy increased with the mass-to-charge ratio, with all three shock-normal velocities showing a similar relation. We showed how minor ion acceleration times lead to very hard ion spectra, especially during early stages of the acceleration process.

7.3 Paper III

Paper III considered injection efficiency without any bootstrapped wave amplification or actual acceleration. We assessed the importance of correctly accounting for anisotropy of transmitted seed populations. We compared Monte Carlo simulations where we either assumed instant particle isotropy in the downstream or isotropisation through small-angle scatterings. We found that parallel and quasi-parallel shocks can efficiently inject slow, thermal seed particles. It is these slow, thermal particles for which anisotropy is greatest, and in their case the diffusive approximation is most likely to be incorrect. We found that properly accounting for downstream isotropisation through scatterings results in decreased injection efficiency of thermal particles, and that it caused the elimination of the thermal injection component to take place at smaller shock-normal angles. These differences decreased injection of thermal particles but did not completely prevent it.

We also considered the effects of cross-field diffusion and a cross-shock electrostatic potential on particle injection. However, we did this within the constraints of guiding centre motion, choosing to exclude field-line random walk and full-orbit calculations from **Paper III**. Cross-field diffusion was found to be of minor effect at small shock-normal angles. At large values of θ_{Bn}, we found that cross-field diffusion could, with a minor adjustment of boundary conditions, be seen to approximately double or halve the injection of fast particles. However, at large shock-normal angles, the primary method of injection was reflection, and cross-field diffusion had a significant effect on total injection efficiency only at a very small range of values for θ_{Bn}.

We found that the presence of an electrostatic cross-shock potential increased the probability of reflection and decreased the probability of injection of transmitted particles. Properly accounting for downstream isotropisation through scatterings increased the prohibiting effect of the cross-shock potential on thermal particles, and caused thermal particles to

be eliminated from injection at smaller shock-normal angles. Suprathermal particles, with a higher chance of being reflected, displayed a weaker correlation between cross-shock potential strength and injection probability of transmitted particles.

In conclusion, in **Paper III**, we presented how injection of thermal and quasi-thermal particles is a complex process, and how downstream isotropisation of particles requires delicate consideration. We found that the presence of a cross-shock potential had a non-negligible effect on injection efficiency, but that cross-field diffusion did not drastically alter injection probabilities.

7.4 Paper IV

Paper IV considered the limitations of QLT in comparison with full-orbit simulations. We presented full-orbit simulations of particle scattering in a turbulent plasma and compared them with simplified analytical calculations of Fokker-Planck coefficients. Three-dimensional incompressible MHD simulations were used to describe coronal plasmas with non-linear wave interactions and energy cascading to high wavenumbers. This was accomplished by using a pseudo-spectral method and the GISMO simulation software package (see, e.g., Lange & Spanier 2012).

We simulated the effect of proton streaming on Alfvén waves by injecting an amplified peak of energy, representing a peaked spectrum generated by a mono-energetic particle beam, into the three-dimensional plasma simulation. This energised plasma was then used for simulated test particle propagation and scattering. The change in particle pitch-angles over the simulation time was used to infer an estimate for the pitch-angle diffusion coefficient $D_{\mu\mu}$.

As an alternative approach, we decomposed plasma turbulence data into three-dimensional wave spectra, which were used in calculating the Fokker-Planck scattering coefficients $D_{\mu\mu}$ according to SQLT. These SQLT coefficients were then compared with the full-orbit coefficients. We found that for peaked turbulence, full-orbit simulations and SQLT showed similarities at resonant pitch-angles, but at non-resonant frequencies SQLT greatly underestimated scattering frequency. We note that, especially when the strength of turbulence $\delta B/B_0$ is strong, full-orbit simulations indicated pitch-angle scattering to be only weakly dependent on μ, which suggests

that the simplifications described in section 3.3 are reasonable.

7.5   Additional results of DSA at coronal shocks

In chapter 6, we presented additional simulation results of DSA at coronal shocks. We found that most of our simulations were in fact incapable of generating meaningful trapping, except at energies below 1 MeV. The presented cases resulted in small scattering centre compression ratios, with the resultant high-energy particle spectra power-laws being equal to those of the injected seed populations.

Our solar wind model predicts very high Alfvén speeds and low gas compression ratios in the spatial region of our simulations, which is a source of low Alfvénic Mach numbers, and thus, softer predicted spectra (or the spectra of the seed population). Simulating acceleration at shocks with larger shock-normal velocities and smaller Alfvén speeds might result in more efficient acceleration.

We show how wave amplification dynamics can vary greatly based on shock obliquity, and thus, injection efficiency. We find that efficient injection of thermal particles can result in significant wave amplification in front of the shock, generating a very large turbulent trapping region in front of the shock. The parallel case resulted in rapid deposition of particle energy into wave power, after which cascading, and especially inverse cascading, modified the shape of the power spectrum, extending the turbulent trapping region to high energies, i.e., low frequencies. The full dynamics of this region cannot be explained with the results presented in chapter 6, but they are exhibited as build-up at low energies for oblique shocks and efficient acceleration to high energies at parallel shocks. Particle spectra extending beyond the turbulent trapping region exhibit power-laws compatible with the source population, where particles have experienced only negligible DSA.

We show that minor ion acceleration at oblique shocks is as expected, with turbulent trapping region dynamics comparable with those of protons, as can be extrapolated from the results published in **Paper II**.

Chapter 8

Future prospects

The work presented in this thesis is a comprehensive report on SEP acceleration through DSA at coronal shocks, especially from the viewpoint of numerical simulations and the CSA software suite. In this chapter, we present some ideas on how to address limitations of the approaches taken in this research, as well as plans for further parameter studies and improvements.

CSA uses a number of simplifications and approximations when considering wave-particle interactions, resonance conditions and wave cascading. Although the results presented in **Paper IV** suggest an isotropic scattering condition can be applied to acceleration at coronal plasmas, a proper anisotropic consideration would be preferable. Afanasiev & Vainio (2013) have prepared an anisotropic scattering formulation, which could be implemented into CSA. This would, however, require wave amplification tracking through particle streaming not in spatial wave frame coordinates, but in pitch-angle space. Additionally, the question of the resonance gap (see, e.g., Ng & Reames 1995) must be considered carefully.

As was shown in chapter 6, wave cascading has a major impact on the spectral shape of Alfvénic turbulence. Our linear diffusive approximation is stable and results in near-Earth spectra which are compatible with observations, but it could be replaced with a more accurate method using a non-linear power-dependent flux function or diffusion coefficient. In order to properly model interactions between waves, the CSA framework could be extended to encompass multiple parallel wave modes and a cascading function which considers interactions of waves propagating in opposite directions. Inclusion of oblique wave modes remains likely outside the scope of this type of simulation.

As was shown in **Paper III**, particle-shock interactions and the injection process must be modelled with great care. The near-shock region of CSA simulation could possibly be replaced with a full-orbit model, with possible future expansions being downstream field-line random walk, spatial shock profile modelling, shock front velocity profile modification, and perhaps even wave transmission into the downstream including particle and wave transport therein.

An additional future prospect is connecting the shock and injection parameters of CSA to coronal MHD simulations. This would allow fitting MHD simulations to EUV observations of CME expansion, feeding these parameters into CSA and comparing acceleration and transport results with particle detector observations.

Reworking of shock parametrisation to better model shock fronts associated with observed CME expansion, along with associated parameter studies, are likely topics of near-future studies. In addition, a parameter study aimed at modelling shocks with high Alfvénic mach numbers and high scattering centre compression ratios, resulting in efficient trapping, is of high interest. If these simulations are to include quasi-parallel shocks, with strong injection of thermal particles, the seed particle selection routines should be amended to encompass injection of highly suprathermal particles in addition to the abundant thermal population.

In conclusion, although CSA can still be improved in a number of ways, it presents a numerically efficient way to simulate long-term DSA within the solar corona and the inner heliosphere, using only reasonable and justified approximations. As such, it is a useful tool, the results of which should be of interest to the whole solar physics community.

Bibliography

Afanasiev, A. & Vainio, R. 2013, ApJS, 207, 29

Alfvén, H. 1942, Nature, 150, 405

Alfvén, H. 1950, Cosmical electrodynamics

Alfvén, H. 1977, Reviews of Geophysics and Space Physics, 15, 271

Armstrong, T. P., Chen, G., Sarris, E. T., & Krimigis, S. M. 1977, in Astrophysics and Space Science Library, Vol. 71, Study of Travelling Interplanetary Phenomena, ed. M. A. Shea, D. F. Smart, & S. T. Wu, 367–388

Axford, W. I. 1981, in International Cosmic Ray Conference, Vol. 12, International Cosmic Ray Conference, 155–203

Axford, W. I., Leer, E., & Skadron, G. 1977, in International Cosmic Ray Conference, Vol. 11, International Cosmic Ray Conference, 132–+

Baring, M. G., Ellison, D. C., & Jones, F. C. 1995, Advances in Space Research, 15, 397

Barnes, A. & Hollweg, J. V. 1974, J. Geophys. Res., 79, 2302

Bell, A. R. 1977, MNRAS, 179, 573

Bell, A. R. 1978, MNRAS, 182, 147

Blandford, R. D. & Ostriker, J. P. 1978, ApJ, 221, L29

Box, G. E. P. & Muller, M. E. 1958, Ann. Math. Statist., 29, 610

Boyd, T. & Sanderson, J. 2003, The Physics of Plasmas (Cambridge University Press)

Burlaga, L. F., Ness, N. F., & Acuña, M. H. 2006, ApJ, 642, 584

Campeanu, A. & Schlickeiser, R. 1992, A&A, 263, 413

Cane, H. V., von Rosenvinge, T. T., Cohen, C. M. S., & Mewaldt, R. A. 2003, Geophys. Res. Lett., 30, 8017

Chandrasekhar, S. 1943, Reviews of Modern Physics, 15, 1

Chin, Y.-C. & Wentzel, D. G. 1972, Ap&SS, 16, 465

Cliver, E. W., Kahler, S. W., Cane, H. V., et al. 1983, Sol. Phys., 89, 181

Crank, J., Nicolson, P., & Hartree, D. R. 1947, Proceedings of the Cambridge Philosophical Society, 43, 50

Cranmer, S. R. & van Ballegooijen, A. A. 2005, ApJS, 156, 265

Cranmer, S. R., van Ballegooijen, A. A., & Edgar, R. J. 2007, ApJS, 171, 520

de Hoffmann, F. & Teller, E. 1950, Physical Review, 80, 692

Denskat, K. U. & Neubauer, F. M. 1982, J. Geophys. Res., 87, 2215

Dobrowolny, M., Mangeney, A., & Veltri, P. 1980, Physical Review Letters, 45, 144

Dorman, L. I. & Pustil'nik, L. 2008, Sun and Geosphere, 3, 7

Drury, L. O. 1983, Reports on Progress in Physics, 46, 973

Earl, J. A. 1974, ApJ, 193, 231

Earl, J. A. 1976, ApJ, 205, 900

Ellison, D. C., Baring, M. G., & Jones, F. C. 1995, ApJ, 453, 873

Ellison, D. C., Baring, M. G., & Jones, F. C. 1996, ApJ, 473, 1029

Ellison, D. C. & Ramaty, R. 1985, ApJ, 298, 400

Fairfield, D. H. 1968, J. Geophys. Res., 73, 7329

Fermi, E. 1949, Physical Review, 75, 1169

Fisk, L. A. 1971, J. Geophys. Res., 76, 1662

Forman, M. A. & Drury, L. O. 1983, in International Cosmic Ray Conference, Vol. 2, International Cosmic Ray Conference, 267

Forman, M. A. & Webb, G. M. 1985, in Washington DC American Geophysical Union Geophysical Monograph Series, Vol. 35, Washington DC American Geophysical Union Geophysical Monograph Series, ed. B. T. Tsurutani & R. G. Stone, 91–114

Galinsky, V. L. & Shevchenko, V. I. 2010, Nonlinear Processes in Geophysics, 17, 663

Gardiner, C. 1985, Handbook of stochastic methods for physics, chemistry, and the natural sciences, Springer series in synergetics (Springer-Verlag)

Gedalin, M. 1996, J. Geophys. Res., 101, 4871

Giacalone, J. 2005, ApJ, 624, 765

Giacalone, J. & Jokipii, J. R. 2006, Journal of Physics Conference Series, 47, 160

Giacalone, J. & Jokipii, J. R. 2007, ApJ, 663, L41

Giacalone, J. & Neugebauer, M. 2008, ApJ, 673, 629

Gibbs, J. 1902, Elementary principles in statistical mechanics: developed with especial reference to the rational foundations of thermodynamics, Yale bicentennial publications (C. Scribner's sons)

Gleeson, L. J. & Axford, W. I. 1967, ApJ, 149, L115

Gleeson, L. J. & Webb, G. M. 1980, Fund. Cosmic Phys., 6, 187

Goldreich, P. & Sridhar, S. 1995, ApJ, 438, 763

Gopalswamy, N., Xie, H., Yashiro, S., et al. 2012, Space Sci. Rev., 171, 23

Grechnev, V. V., Afanasyev, A. N., Uralov, A. M., et al. 2011, Sol. Phys., 273, 461

Grevesse, N., Noels, A., & Sauval, A. J. 1996, in Astronomical Society of the Pacific Conference Series, Vol. 99, Cosmic Abundances, ed. S. S. Holt & G. Sonneborn, 117

Gringauz, K. I., Bezrokikh, V. V., Ozerov, V. D., & Rybchinskii, R. E. 1960, Soviet Physics Doklady, 5, 361

Hasselmann, K. & Wibberenz, G. 1968, Z. Geophys., 34, 353

Hollweg, J. V. 1986, J. Geophys. Res., 91, 4111

Horbury, T. S., Balogh, A., Forsyth, R. J., & Smith, E. J. 1996, A&A, 316, 333

Hull, A. J., Scudder, J. D., Fitzenreiter, R. J., et al. 2000, J. Geophys. Res., 105, 20957

Iroshnikov, P. S. 1963, AZh, 40, 742

Iroshnikov, P. S. 1964, Soviet Ast., 7, 566

Jokipii, J. R. 1966, ApJ, 146, 480

Jokipii, J. R. 1971, Reviews of Geophysics and Space Physics, 9, 27

Jokipii, J. R. & Parker, E. N. 1970, ApJ, 160, 735

Jones, F. C. 1990, ApJ, 361, 162

Jones, F. C., Baring, M. G., & Ellison, D. C. 1993, in International Cosmic Ray Conference, Vol. 2, International Cosmic Ray Conference, 243

Jones, F. C. & Ellison, D. C. 1991, Space Sci. Rev., 58, 259

Kallenrode, M. 2004, Space Physics: An Introduction to Plasmas and Particles in the Heliosphere and Magnetospheres, Advanced Texts in Physics (Springer)

Kocharov, L., Pizzo, V. J., Odstrcil, D., & Zwickl, R. D. 2009, Journal of Geophysical Research (Space Physics), 114, 5102

Kocharov, L., Vainio, R., Kovaltsov, G. A., & Torsti, J. 1998, Sol. Phys., 182, 195

Kocharov, L. G., Torsti, J., Vainio, R., & Kovaltsov, G. A. 1996, Sol. Phys., 165, 205

Kolmogorov, A. 1941, Akademiia Nauk SSSR Doklady, 30, 301

Kolmogorov, A. N. 1991, Royal Society of London Proceedings Series A, 434, 9

Kraichnan, R. H. 1965, Physics of Fluids, 8, 1385

Krymskii, G. F. 1977, Akademiia Nauk SSSR Doklady, 234, 1306

Krymsky, G. F., Kuzmin, A. I., Petukhov, S. I., & Turpanov, A. A. 1979, in International Cosmic Ray Conference, Vol. 2, International Cosmic Ray Conference, 39

Kulsrud, R. 2005, Plasma Physics for Astrophysics, Princeton Series in Astrophysics (Princeton University Press)

Kulsrud, R. & Pearce, W. P. 1969, ApJ, 156, 445

Kuncic, Z., Cairns, I. H., & Knock, S. 2002, Journal of Geophysical Research (Space Physics), 107, 1218

Kunstmann, J. E. 1979, ApJ, 229, 812

Laitinen, T. 2003, Energetic Particle Acceleration and Transport in Wave-heated Solar Wind, Turun Yliopiston Julkaisuja: Astronomica, Chemica, Physica, Mathematica (Turun Yliopisto)

Lange, S. & Spanier, F. 2012, A&A, 546, A51

Lario, D., Hu, Q., Ho, G. C., et al. 2005, in ESA Special Publication, Vol. 592, Solar Wind 11/SOHO 16, Connecting Sun and Heliosphere, ed. B. Fleck, T. H. Zurbuchen, & H. Lacoste, 81

Lax, P. & Wendroff, B. 1960, Commun. Pure Appl. Math., 13, 217

Lee, M. A. 1971, Plasma Physics, 13, 1079

Lee, M. A. 1982, J. Geophys. Res., 87, 5063

Lee, M. A. 1983, J. Geophys. Res., 88, 6109

Lee, M. A. 2000, in American Institute of Physics Conference Series, Vol. 528, Acceleration and Transport of Energetic Particles Observed in the Heliosphere, ed. R. A. Mewaldt, J. R. Jokipii, M. A. Lee, E. Möbius, & T. H. Zurbuchen , 3–18

Lee, M. A. 2005, ApJS, 158, 38

Lehmann, E. & Casella, G. 1998, Theory of Point Estimation, Springer Texts in Statistics (Springer)

Leith, C. E. 1967, Physics of Fluids, 10, 1409

Lever, E. L., Quest, K. B., & Shapiro, V. D. 2001, Geophys. Res. Lett., 28, 1367

Li, G., Shalchi, A., Ao, X., Zank, G., & Verkhoglyadova, O. P. 2012, Advances in Space Research, 49, 1067

Li, G. & Zank, G. P. 2005, Geophys. Res. Lett., 32, 2101

Lodders, K. 2003, ApJ, 591, 1220

Luhmann, J. G. 1976, J. Geophys. Res., 81, 2089

Lund, N. 1989, in American Institute of Physics Conference Series, Vol. 183, Cosmic Abundances of Matter, ed. C. J. Waddington, 111–123

Ma, S., Raymond, J. C., Golub, L., et al. 2011, ApJ, 738, 160

Malandraki, O. E., Agueda, N., Papaioannou, A., et al. 2012, Sol. Phys., 281, 333

Malkov, M. A. & Völk, H. J. 1995a, in International Cosmic Ray Conference, Vol. 3, International Cosmic Ray Conference, 277

Malkov, M. A. & Völk, H. J. 1995b, A&A, 300, 605

Malkov, M. A. & Völk, H. J. 1998, Advances in Space Research, 21, 551

Mason, G. M., Mazur, J. E., & Dwyer, J. R. 1999, ApJ, 525, L133

Matthaeus, W. H., Zhou, Y., Zank, G. P., & Oughton, S. 1994, J. Geophys. Res., 99, 23421

Miller, J. A. & Roberts, D. A. 1995, ApJ, 452, 912

Morton, K. & Mayers, D. 2005, Numerical Solution of Partial Differential Equations: An Introduction, Numerical Solution of Partial Differential Equations: An Introduction (Cambridge University Press)

Neergaard Parker, L. & Zank, G. P. 2012, ApJ, 757, 97

Ng, C. K. 2007, in American Institute of Physics Conference Series, Vol. 932, Turbulence and Nonlinear Processes in Astrophysical Plasmas, ed. D. Shaikh & G. P. Zank, 271–276

Ng, C. K. & Reames, D. V. 1994, ApJ, 424, 1032

Ng, C. K. & Reames, D. V. 1995, ApJ, 453, 890

Ng, C. K. & Reames, D. V. 2008, ApJ, 686, L123

Ng, C. K., Reames, D. V., & Tylka, A. J. 1999, Geophys. Res. Lett., 26, 2145

Ng, C. K., Reames, D. V., & Tylka, A. J. 2003, ApJ, 591, 461

Ng, C. K., Reames, D. V., & Tylka, A. J. 2012, in American Institute of Physics Conference Series, Vol. 1436, American Institute of Physics Conference Series, ed. J. Heerikhuisen, G. Li, N. Pogorelov, & G. Zank, 212–218

Ng, C. K. & Wong, K.-Y. 1979, in International Cosmic Ray Conference, Vol. 5, International Cosmic Ray Conference, 252

Ostrowski, M. & Schlickeiser, R. 1996, Sol. Phys., 167, 381

Palmer, I. D. 1982, Reviews of Geophysics and Space Physics, 20, 335

Parker, E. N. 1965a, Space Sci. Rev., 4, 666

Parker, E. N. 1965b, Planet. Space Sci., 13, 9

Pomoell, J., Vainio, R., & Kissmann, R. 2011, Astrophysics and Space Sciences Transactions, 7, 387

Prested, C., Schwadron, N., Passuite, J., et al. 2008, Journal of Geophysical Research (Space Physics), 113, 6102

Priest, E. R. 1982, Solar magneto-hydrodynamics (D.Reidel), 74P

Reames, D. V. 1990a, ApJ, 358, L63

Reames, D. V. 1990b, ApJS, 73, 235

Reames, D. V. 1995, Advances in Space Research, 15, 41

Reames, D. V. 1998, Space Sci. Rev., 85, 327

Reames, D. V. 1999a, Space Sci. Rev., 90, 413

Reames, D. V. 1999b, ApJ, 518, 473

Reames, D. V. 2002, ApJ, 571, L63

Reames, D. V. 2009, ApJ, 706, 844

Reames, D. V. & Ng, C. K. 1998, ApJ, 504, 1002

Reames, D. V. & Ng, C. K. 2010, ApJ, 723, 1286

Reames, D. V., Ng, C. K., & Tylka, A. J. 2012, Sol. Phys., 126

Reames, D. V., Richardson, I. G., & Wenzel, K.-P. 1992, ApJ, 387, 715

Roelof, E. C. 1969, in Lectures in High-Energy Astrophysics, ed. H. Ögelman & J. R. Wayland, 111

Ross, J. E. & Aller, L. H. 1976, Science, 191, 1223

Ruffolo, D. 1995, ApJ, 442, 861

Salas, M. D. 2007, Shock Waves, 16, 477

Sandroos, A. & Vainio, R. 2006, A&A, 455, 685

Sandroos, A. & Vainio, R. 2007, ApJ, 662, L127

Sandroos, A. & Vainio, R. 2009a, A&A, 507, L21

Sandroos, A. & Vainio, R. 2009b, ApJS, 181, 183

Sarris, E. T. & van Allen, J. A. 1974, J. Geophys. Res., 79, 4157

Schlickeiser, R. 1989, ApJ, 336, 243

Schlickeiser, R. 2002, Cosmic Ray Astrophysics (Springer)

Schlickeiser, R., Campeanu, A., & Lerche, L. 1993, A&A, 276, 614

Schwenn, R. & Marsch, E. 1991, Physics of the Inner Heliosphere II. Particles, Waves and Turbulence.

Shebalin, J. V., Matthaeus, W. H., & Montgomery, D. 1983, Journal of Plasma Physics, 29, 525

Skilling, J. 1971, ApJ, 170, 265

Skilling, J. 1975, MNRAS, 172, 557

Spanier, F. & Vainio, R. 2008, ArXiv e-prints

Srivastava, N. & Schwenn, R. 2000, in The Outer Heliosphere: Beyond the Planets, ed. K. Scherer, H. Fichtner, & E. Marsch, 13

Terasawa, T. 1979, Planet. Space Sci., 27, 193

Torsti, J., Aurela, A., Kelha, V., et al. 1988, ERNE: Energetic and Relativistic Nuclei and Electron experiment, Tech. rep.

Torsti, J., Laitinen, T., Vainio, R., et al. 1997, Sol. Phys., 175, 771

Tu, C.-Y., Pu, Z.-Y., & Wei, F.-S. 1984, J. Geophys. Res., 89, 9695

Tylka, A. J., Boberg, P. R., McGuire, R. E., Ng, C. K., & Reames, D. V. 2000, in American Institute of Physics Conference Series, Vol. 528, Acceleration and Transport of Energetic Particles Observed in the Heliosphere, ed. R. A. Mewaldt, J. R. Jokipii, M. A. Lee, E. Möbius, & T. H. Zurbuchen , 147–152

Tylka, A. J., Cohen, C. M. S., Dietrich, W. F., et al. 2005, ApJ, 625, 474

Tylka, A. J., Cohen, C. M. S., Dietrich, W. F., et al. 2001, ApJ, 558, L59

Tylka, A. J., Reames, D. V., & Ng, C. K. 1999, Geophys. Res. Lett., 26, 2141

Vainio, R. 1999, in Plasma Turbulence and Energetic Particles in Astrophysics, ed. M. Ostrowski & R. Schlickeiser, 232–245

Vainio, R. 2003, A&A, 406, 735

Vainio, R., Kocharov, L., & Laitinen, T. 2000, ApJ, 528, 1015

Vainio, R. & Laitinen, T. 2001, A&A, 371, 738

Vainio, R. & Laitinen, T. 2007, ApJ, 658, 622

Vainio, R. & Laitinen, T. 2008, Journal of Atmospheric and Solar-Terrestrial Physics, 70, 467

Vainio, R., Laitinen, T., & Fichtner, H. 2003, A&A, 407, 713

Vainio, R. & Schlickeiser, R. 1998, A&A, 331, 793

Vainio, R. & Schlickeiser, R. 1999, A&A, 343, 303

Vainio, R. & Spanier, F. 2005, A&A, 437, 1

van Leer, B. 1974, Journal of Computational Physics, 14, 361

van Nes, P., Reinhard, R., Sanderson, T. R., Wenzel, K.-P., & Zwickl, R. D. 1984, J. Geophys. Res., 89, 2122

Vasyliunas, V. M. 1968, J. Geophys. Res., 73, 2839

Watermann, J., Vainio, R., Lilensten, J., Belehaki, A., & Messerotti, M. 2009, Space Sci. Rev., 147, 111

Webb, G. M., Axford, W. I., & Terasawa, T. 1983, ApJ, 270, 537

Wells, D. C., Greisen, E. W., & Harten, R. H. 1981, A&AS, 44, 363

Wright, J. M., Lennon, T. J., Corell, R. W., et al. 1995, The National Space Weather Program Strategic Plan

Zank, G. P., Li, G., & Verkhoglyadova, O. 2007, Space Sci. Rev., 130, 255

Zank, G. P., Rice, W. K. M., Le Roux, J. A., Cairns, I. H., & Webb, G. M. 2001, Physics of Plasmas, 8, 4560

Zank, G. P., Rice, W. K. M., & Wu, C. C. 2000, J. Geophys. Res., 105, 25079

Zhou, Y. & Matthaeus, W. H. 1990, J. Geophys. Res., 95, 14881